



Tullius, Ryan Michael (2017) *High-throughput biosensing using chiral plasmonic nanostructures*. PhD thesis.

<http://theses.gla.ac.uk/8657/>

Copyright and moral rights for this work are retained by the author

A copy can be downloaded for personal non-commercial research or study, without prior permission or charge

This work cannot be reproduced or quoted extensively from without first obtaining permission in writing from the author

The content must not be changed in any way or sold commercially in any format or medium without the formal permission of the author

When referring to this work, full bibliographic details including the author, title, awarding institution and date of the thesis must be given

Enlighten:Theses
<http://theses.gla.ac.uk/>
theses@gla.ac.uk

High-Throughput Biosensing using Chiral Plasmonic Nanostructures

Ryan Michael Tullius



University
of Glasgow

Submitted in fulfilment of the requirements for the
Degree of Doctor of Philosophy

School of Chemistry
College of Science and Engineering
University of Glasgow

August 2017

Abstract

The object of this thesis, is to demonstrate the potential capabilities of injection moulded chiral plasmonic nanostructures for enhanced sensing in biological systems. The key phenomenon employed throughout this thesis is the generation of electromagnetic fields, that produce a greater chiral asymmetry than that of circularly polarised light, termed 'superchiral' fields. These superchiral fields will be demonstrated as being an incisive probe into the structure, conformation, and orientation of proteins immobilised on the nanostructure surface of these injection moulded substrates. Initially, it will be shown how this phenomenon is sensitive to higher order changes in protein structure induced upon ligand binding, using an asymmetry parameter extracted from the optical rotatory dispersion (ORD) spectra. Where these changes would not be routinely detected by conventional chiroptical spectroscopy techniques, such as circular dichroism (CD). Further to this, as these nanostructures display the plasmonic analogue of the interference effect, electromagnetically induced transparency (EIT), a narrow transparency window is created within a broad reflectance spectrum. Where the spectra can be modelled using a simple coupled oscillator model, and the retardation phase effects extracted. This allows two new asymmetry parameters to be introduced for characterising any changes induced by the biological samples, the experimental separation parameter $\Delta\Delta S$, and the modelled retardation phase asymmetries. These will be used to characterise the orientation of three structurally similar protein fragments, called Affimers, with the modelled phase asymmetries being shown as a particularly incisive probe into the surface immobilised orientation. Furthermore, conformational changes in the cancer relevant protein, HSP90, will be characterised upon the addition of increasing concentrations of the inhibitor molecule 17-AAG. With the orientation of the immobilised HSP90 protein being shown to influence the sensitivity observed for any protein-ligand interactions that occur. Finally, this phenomenon will be used to quantitatively detect elevated protein levels in a complex solution. Elevated levels of IgG will be measured in human blood serum solutions, utilising the isoelectric point of the proteins in solution to enhance the level of IgG adsorbed in the protein corona. This will demonstrate for the first time, the use of superchiral fields generated around injection moulded chiral nanostructures, to detect protein changes in complex real life solutions, such as human blood serum. Representing the first step in creating a high-throughput ultrasensitive system for a range of diagnostic applications.

Contents

Abstract	ii
Contents	iii
List of Figures	vii
List of Tables	xiv
Acronyms and Abbreviations	xv
Publications	xvii
Acknowledgements	xviii
Authors Declaration	xix
Chapter 1 – Introduction	
1.1 Thesis Overview	1
1.2 References	5
Chapter 2 – Theory	
2.1 Chirality	6
2.1.1 Molecular Chirality	6
2.2 Optical Activity	7
2.2.1 Optical Rotation	7
2.2.2 Circular Dichroism	9
2.2.3 Optical Rotatory Dispersion	10
2.3 Superchirality	11
2.3.1 Superchiral Fields	11
2.4 Plasmonics	13
2.4.1 Plasmonic Oscillations	13
2.4.2 Surface Plasmon Polaritons	14
2.4.3 Plasmon Excitation	16
2.4.4 Localised Surface Plasmon Resonances	17
2.4.5 Plasmonic Hybridisation	19
2.5 Interference Effects	21

2.5.1 Fano Resonance	22
2.5.2 Electromagnetically Induced Transparency	23
2.5.3 Plasmonic Electromagnetically Induced Transparency	24
2.5.4 Plasmonic EIT Modelling	25
2.6 References	26

Chapter 3 – Experimental

3.1 Introduction	29
3.2 Nanostructure Fabrication	29
3.2.1 Template Fabrication	29
3.2.2 Injection Moulding	30
3.2.3 TPS Preparation	31
3.2.4 Nanostructure Geometry	32
3.2.5 Nanostructure Hybridisation	33
3.3 Structure Characterisation Microscopy	35
3.3.1 Scanning Electron Microscopy (SEM)	35
3.3.2 Atomic Force Microscopy (AFM)	36
3.4 Spectroscopy	38
3.4.1 Polarisation Microscope	38
3.4.2 Optical Rotatory Dispersion Spectroscopy	40
3.4.3 Reflectance Spectroscopy	42
3.4.4 Electromagnetic Modelling	44
3.4.5 Refractive Index Measurements	45
3.5 Surface Functionalisation and Preparation	47
3.5.1 Nitrilotriacetic Acid (NTA) Functionalisation	47
3.5.2 Protein Preparation	49
3.5.3 Microfluidic Chamber	49
3.6 Modelling	50
3.6.1 Mathematical Model for EIT	50
3.6.2 Salt Solution Modelling	52
3.7 References	54

Chapter 4 – Detection of Ligand Induced Changes in Protein Higher Order Structure

4.1	Introduction	55
4.2	Proteins	56
	4.2.1 The Shikimate Pathway	56
	4.2.2 5-enolpyruvylshikimate-3-phosphate (EPSP) Synthase	56
	4.2.3 Shikimate Kinase (SK)	57
4.3	Results and Discussion	58
	4.3.1 Immobilisation Coverage	58
	4.3.2 Measurement of Protein Structural Changes	59
	4.3.3 Circular Dichroism Spectroscopy	61
	4.3.4 Discussion	63
4.4	Conclusion	64
4.5	References	66

Chapter 5 – Orientation Determination of Adsorbed Structurally Similar Affimers

5.1	Introduction	68
5.2	Affimers	69
5.3	Results and Discussion	70
	5.3.1 Measurement of Affimers	70
	5.3.2 Non-Target Binding	73
	5.3.3 Affimer Modelling	74
	5.3.4 Discussion	78
5.4	Conclusion	82
5.5	References	83

Chapter 6 – Characterisation of Surface Orientation and Ligand Induced Conformational Changes for Heat Shock Protein 90

6.1	Introduction	85
6.2	Heat Shock Protein 90 (HSP90)	86
6.3	Results and Discussion	88

6.3.1 Measurement of HSP90 and Ligand Addition	88
6.3.2 Control Measurements	90
6.3.3 HSP90 Modelling	91
6.3.4 Discussion	93
6.4 Conclusion	96
6.5 References	98

Chapter 7 – Detection of Elevated Immunoglobulin G Levels in Human Serum

7.1 Introduction	99
7.2 Human Blood Serum	100
7.2.1 Immunoglobulin G (IgG)	101
7.2.2 Protein Corona	102
7.3 Results and Discussion	103
7.3.1 IgG Spiked Serum Measurements	104
7.3.2 Saline Buffered Spiked Serum Measurements	108
7.3.3 Non-IgG Spiked Serum Solutions	112
7.3.4 Discussion	114
7.4 Conclusion	117
7.5 References	119

Summary and Future Outlook

Appendix A	124
Appendix B	126
Appendix C	127
Appendix D	129
Appendix E	132
Appendix F	134

List of Figures

- Figure 2.01** Electric field vectors of circularly polarised light propagating along z . Vectors rotate clockwise when viewed in the $-z$ direction showing right-handed polarisation.
- Figure 2.02** (a) Electric field vector of linearly polarised light split into the two components of left- and right-circularly polarised light propagating out of the page, (b) electric field vector rotated at a further point of propagation through an optically active medium.
- Figure 2.03** (a) Electric field vector of linearly polarised light split into the two components of left- and right-circularly polarised light propagating out of the page, (b) differential absorption of left- and right-CPL causing elliptically polarised light, specified by angle φ .
- Figure 2.04** Ellipticity and related optical rotatory dispersion curves centred around the electronic absorption wavelength λ_j .
- Figure 2.05** Graphical representation of plasmonic oscillations. (a) bulk metal with no electric charge applied, (b) shows after application of an electric field causing displacement of the electron cloud, (c) shows oscillation of electron cloud in opposite direction when electric field turned off.
- Figure 2.06** Graphical representation of (a) the surface charges and resultant electromagnetic wave at the metal-dielectric interface, and (b) the electric field strength in the z direction for both the dielectric and metal. δ_d and δ_m are the penetration depths of the SPP wave into the dielectric and metal respectively.
- Figure 2.07** Dispersion curves for surface plasmon polariton, and light in a vacuum. Wavevector for SPP is always higher than for light at the same frequency.
- Figure 2.08** Prism coupling methods of SPP excitation at a metal-dielectric interface. (a) Kretschmann configuration, and (b) Otto configuration.
- Figure 2.09** Graphical representation of localised surface plasmons on metallic nanospheres.

- Figure 2.10** Hybridisation (energy level) diagram of two nanorods aligned longitudinally to each other and separated by a small gap.
- Figure 2.11** Schematic of the coupled oscillator model between bright and dark modes.
- Figure 2.12** Asymmetric Fano resonance produced from the coupling of optically bright and dark plasmon modes.
- Figure 2.13** (a) Three level EIT system where ω_p and ω_c are the frequency of the probe and coupling beams, and (b) EIT absorption spectra showing a narrow transparency dip within a broad absorption band.
- Figure 3.01** Graphical description of nickel shim fabrication for injection moulding process.
- Figure 3.02** (a) Picture of Engel Victory 28 injection moulder, (b) graphical description of the injection moulder tool showing the nickel shim within the moulding cavity, and (c) graphical description of the high-throughput injection moulding process for creating each templated substrate.
- Figure 3.03** Photo of injection moulded substrates before, and after 100 nm gold is evaporated onto the nanopatterned surface.
- Figure 3.04** (a) Top and side view of shuriken indentation in injection moulded polymer substrate (80 nm depth), (b) shuriken indentations after evaporation with 100 nm gold, showing continuous gold film and indentations, and (c) SEM images of both right- (blue border) and left-handed (red border) shuriken structures with diameter of 500 nm and periodicity of 700 nm.
- Figure 3.05** Hybridisation scheme between electric and magnetic modes of the shuriken nanostructures. Δ is the energy separation between the bright and dark modes.
- Figure 3.06** SEM image of right handed shuriken structures recorded using the FEI Nova NanoSEM 630, after the evaporation of 100 nm gold onto the nanostructured surface.
- Figure 3.07** Graphical description of atomic force microscopy (AFM) system.

- Figure 3.08** AFM image, and height profiles, for shuriken structures covered with 100 nm gold. Red and blue lines overlaying the AFM image correspond to the regions where the similarly coloured height profiles were measured.
- Figure 3.09** Schematic representation of the custom built polarisation microscope.
- Figure 3.10** Photograph detailing the custom built polarisation microscope.
- Figure 3.11** Picture from Thorlabs DCC1645C camera showing field of view for custom built polarisation microscope.
- Figure 3.12** Example ORD spectra measured from left- (red) and right-handed (blue) nanostructures with water (solid) and a higher refractive index solution (dashed) on the substrate surface.
- Figure 3.13** Example reflectance spectra for both left- and right-handed shuriken structures with water (black), and a higher refractive index solution (coloured) on the substrate surface.
- Figure 3.14** EM simulation of chiral field plots for (a) top surface, and (b) bottom surface of the shuriken structure.
- Figure 3.15** (a) ORD spectra for left- and right-handed nanostructures in the presence of achiral salt solutions of increasing refractive index, (b) peak positions for left- (red) and right-handed (blue) shuriken structures with increasing refractive index solutions, and (c) asymmetry values relative to water for increasing refractive index, with comparison of asymmetry values for two exemplar proteins, EPSP Synthase and SK (Chapter 4).
- Figure 3.16** (a) Reflectance spectra for left- and right-handed nanostructures in the presence of achiral salt solutions of increasing refractive index, (b) average positions for left- (red) and right-handed (blue) shuriken structures with increasing refractive index solutions, and (c) asymmetry values relative to water for increasing refractive index.
- Figure 3.17** Scheme showing NTA monolayer functionalisation, binding of Ni^{2+} , and final binding of His-tagged protein to the NTA/ Ni^{2+} complex.
- Figure 3.18** Labelled photo, showing top and side view, of custom made 3D printed microfluidic chamber for TPSs.

- Figure 3.19** Effect of varying each parameter in the model by small increments from the initial values.
- Figure 3.20** (a) Experimental reflectance spectra (black) and fitting of data without the consideration of phase (blue dashed), and with the introduction of phase (red), and (b-d) fitting results for ω_r , ω_d , k , θ , and ϕ compared to the refractive index of solutions.
- Figure 4.01** Ribbon representations of the crystal structure of EPSP Synthase (a) open form of protein (PDB 2BJB), and (b) closed form of protein after binding (PDB 2O0E) of glyphosate and shikimate-3-phosphate ligand.
- Figure 4.02** Ribbon representations of the crystal structure of SK (a) open form of protein (PDB 2IYV), and (b) closed form of protein after binding (2IYQ) of ADP, shikimic acid and MgCl_2 .
- Figure 4.03** Asymmetry values against corresponding surface coverage for increasing coverage of EPSP synthase immobilised onto the shuriken nanostructures.
- Figure 4.04** ORD data for (a) EPSP Synthase, and (b) shikimate kinase. The top graph of each show the spectra in the presence of buffer only (solid line) to immobilised protein in the presence of buffer (dotted lines), and the bottom graph of each shows the spectra for immobilised protein (from top graph) and immobilised protein in the presence of ligand solutions (dash-dot line). (c) shows $\Delta\Delta\lambda$ values calculated from the ORD spectra for immobilised protein, protein in the presence of ligand solution, and ligand solution only.
- Figure 4.05** CD spectra for unliganded (blue) and ligand bound (red) protein, for EPSP Synthase and shikimate kinase in the top and bottom panels respectively. Spectra are shown for both the far UV and near UV spectra, in the left and right panels respectively.
- Figure 5.01** Ribbon representation of Affimer protein scaffold (PBD 4N6U), labelled with the positions of the inserted cysteines for the three different Affimers.

- Figure 5.02** Bar chart showing average shifts for 3 Affimers; K67C (blue), G65C (red), and H6C (green). Showing average shifts for immobilisation of Affimer, addition of PEG filler, and binding of target protein to Affimer (K67C and G65C bind GST, and H6C binds IgG), all relative to initial buffer measurement.
- Figure 5.03** Bar chart showing asymmetry values calculated for 3 Affimers; K67C (blue), G65C (red), and H6C (green). Showing asymmetry values for immobilisation of Affimer, addition of PEG filler, and binding of target protein to Affimer (K67C and G65C bind GST, and H6C binds IgG), all relative to initial buffer measurement.
- Figure 5.04** Bar charts showing (a) average shift, and (b) asymmetry for immobilised Affimer, addition of PEG filler, and addition of IgG target solution for GST binders, K67C (blue) and G65C (red), all relative to initial buffer measurements.
- Figure 5.05** Graphs showing (a) reflectance spectra for water (black), and salt solution (dashed coloured) for both left- and right-handed shuriken structures, and (b) reflectance spectra for buffer (black) and, the adsorbed G65C Affimer (dashed coloured) for both handedness of shuriken structures. To aid comparison, both salt solution and Affimer spectra have been shifted (solid coloured) to overlap the initial water/buffer spectra.
- Figure 5.06** Graphs showing measured reflectance spectra (black), and fitted spectra (coloured) for buffer and Affimer measurements for (a) G65C, (b) K67C, and (c) H6C.
- Figure 5.07** Bar graphs showing (a) $\Delta\Delta\lambda$ values from ORD spectra, (b) phase parameter (θ and ϕ) asymmetries, (c) coupling parameter (k) asymmetry, and (d) resonance frequency (ω_r and ω_d) asymmetries for all three Affimer variants.
- Figure 5.08** (a) Reflectance spectra from simulation with chiral dielectric covered left- (red) and right-handed (blue) shuriken nanostructures, as well as water covered shuriken structure (black), and (b) asymmetry in phase parameters for the simulated chiral dielectric layer compared with the three Affimer samples.

- Figure 6.01** Heat shock protein 90 dimers in (a) the open form (PDB: 2IOQ), (b) partly closed ATP-bound form (Intermediate 2, PDB: 2O1V), and (c) closed ATP-bound form (PDB: 2CG9). (d) and (e) show the relative immobilised orientation of the HSP90 protein when His-tagged at the C-terminus and N-terminus domain respectively.
- Figure 6.02** Bar chart showing the separation asymmetry parameter for HSP90 His-tagged at the C-terminal domain (blue) and at the N-terminal domain (red) for the initial immobilisation of the protein, and the addition of the 17-AAG ligand with increasing concentrations.
- Figure 6.03** Average shift and separation asymmetry parameter ($\Delta\Delta S$) values for the N-terminal attached HSP90 protein with the addition of control DMSO solutions (no 17-AAG inhibitor).
- Figure 6.04** Bar graphs showing the asymmetry values of θ (red bars) and ϕ (green bars) for the C-terminal (blue background, top) and N-terminal (red background, bottom) attached HSP90 protein.
- Figure 6.05** Bar graphs showing the asymmetries in the resonance frequencies (ω_r and ω_d), and coupling parameter (k) for the C-terminal (blue) and N-terminal (red) attached HSP90.
- Figure 7.01** (a) Crystal structure of immunoglobulin G antibody (PDB: 1IGT), and (b) showing the heavy chains (blue) and the light chains (green).
- Figure 7.02** Average shift (top), and separation asymmetry (bottom) values for solutions of (a) immunoglobulin G (left, blue background), and (b) human serum albumin (right, orange background) in 10 mM Tris buffer. (c) Graphical description of protein corona composition for two IgG concentrations depicted by the arrows from part (a).
- Figure 7.03** Graphs showing (a) average shifts, and (b) asymmetry values for increasing total protein concentration for stock serum solution, and all IgG spiked serum solutions diluted in Tris buffer.
- Figure 7.04** Graph showing the asymmetry value for the highest concentration solution of each spiked sample. Red background region shows the physiologically elevated levels of IgG in human serum.

- Figure 7.05** Graphs showing (a) average shifts, and (b) asymmetry values for increasing total protein concentration for stock serum solution, and all IgG spiked serum solutions diluted in Tris-saline buffer.
- Figure 7.06** Graph showing the asymmetry value for the highest concentration solution of each spiked sample for Tris buffer only dilutions (grey), and Tris-saline buffer dilutions (purple). Red background region shows the physiologically elevated levels of IgG in human serum.
- Figure 7.07** Graph showing the asymmetry parameters for increasing total protein concentration for stock serum (black), Albumin spiked serum (pink), Transferrin spiked serum (purple), and IgA spiked serum (maroon) diluted in Tris buffer. IgG spiked solution containing 17.0% IgG, and diluted in Tris buffer, shown for comparison purposes.
- Figure 7.08** Graph showing asymmetry parameters for increasing total protein concentration for stock serum (black), Albumin spiked serum (pink), Transferrin spiked serum (purple), and IgA spiked serum (maroon) diluted in Tris-saline buffer. IgG spiked solution containing 23.6% IgG, and diluted in Tris-saline buffer, shown for comparison purposes.
- Figure 7.09** (a) Asymmetry values for the highest concentration solutions diluted in Tris buffer (grey), and Tris-saline buffer (purple) for increasing spiked IgG contents. Graphical depiction of the protein corona for the 23.6% elevated IgG serum solution diluted in (b) Tris buffer, and (c) Tris-saline buffer.
- Figure C.01** (a) ORD spectra for EPSP Synthase (top), and shikimate kinase (bottom) ligand solutions relative to initial buffer measurements for left- (red) and right-handed (blue) shuriken structures. The solid and dashed lines represent the initial buffer measurement, and ligand solution measurements respectively. (b) The average shifts measured for EPSP Synthase and shikimate kinase when the protein was immobilised, when the ligand solutions were added to adsorbed proteins, and ligand solutions only in the absence of adsorbed protein.
- Figure D.01** ORD spectra for the three Affimer variants. (a) H6C, (b) G65C, and (c) K67C. Also (d) shows the $\Delta\Delta\lambda$ values for each Affimer for peak 1 of the ORD spectra.

List of Tables

- Table 3.01** Descriptions of the parameters that are used to implement the mathematical model for plasmonic induced transparency.
- Table 3.02** Parameter values used to fit the experimental salt solution spectra for left- and right-handed shuriken structures.
- Table 5.01** Model parameter values used to fit the left- and right-handed reflectance spectra for all three Affimer variant results.
- Table 5.02** Asymmetry values for the five parameters used to fit the Affimer spectra; ω_r , ω_d , k , θ , and ϕ .
- Table 7.01** Table showing the concentration and isoelectric points of constituents present in stock human serum solution.
- Table B.01** C_6 symmetry character table.
- Table D.01** Fitting parameters for the reflectivity of the simulated spectra with water (identical for left- and right-handed nanostructures, and a chiral dielectric for both left- and right-handed structures).
- Table E.01** Modelling values for the five variable parameters for the immobilisation of HSP90, and after the addition of each ligand solution for the C-terminal His-tagged protein.
- Table E.02** Modelling values for the five variable parameters for the immobilisation of HSP90, and after the addition of each ligand solution for the N-terminal His-tagged protein.

Acronyms and Abbreviations

17-AAG	17-allylamino-17-demethoxygeldanamycin
ADP	Adenosine diphosphate
AFM	Atomic force microscopy
ATP	Adenosine triphosphate
BSE	Back-scattered electrons
CD	Circular dichroism
CPL	Circularly polarised light
DMSO	Dimethyl sulfoxide
EBL	Electron beam lithography
EG-thiol	triethylene glycol mono-11-mercaptoundecyl
EIT	Electromagnetically induced transparency
EM	Electromagnetic
EPSP	5-enolpyruvylshikimate-3-phosphate
GST	Glutathione S-transferase
HBS	HEPES buffered saline
HEPES	4-(2-hydroxyethyl)-1-piperazineethanesulfonic acid
HSP90	Heat Shock Protein 90
IgA	Immunoglobulin A
IgD	Immunoglobulin D
IgE	Immunoglobulin E
IgG	Immunoglobulin G
IgM	Immunoglobulin M
IPA	Isopropyl alcohol
IPTG	isopropyl β -D-1-thiogalactopyranoside
IR	Infrared
KK	Kramers-Kronig
LSP	Localised surface plasmon
LSPR	Localised surface plasmon resonance
MIBK	Methyl isobutyl ketone
NMR	Nuclear magnetic resonance

NTA	Nitrilotriacetic acid
OR	Optical rotation
ORD	Optical rotatory dispersion
PEG	Polyethylene glycol
PEP	Phosphoenolpyruvate
PMMA	Poly(methyl methacrylate)
ROA	Raman optical activity
S3P	Shikimate-3-phosphate
SB	Shikimate binding
SE	Secondary electrons
SEM	Scanning electron microscopy
SK	Shikimate kinase
SPP	Surface plasmon polariton
SPR	Surface plasmon resonance
TPS	Templated plasmonic substrates

Publications

1. Ryan Tullius, Affar S, Karimullah, Marion Rodier, Brian Fitzpatrick, Nikolaj Gadegaard, Laurence D. Barron, Vincent M. Rotello, Graeme Cooke, Adrian Laphorn, and Malcolm Kadodwala, *“Superchiral” Spectroscopy: Detection of Protein Higher Order Hierarchical Structure with Chiral Plasmonic Nanostructures*. Journal of the American Chemical Society, 2015. **137**(26): p. 8380 – 8383.
2. Affar S. Karimullah, Calum Jack, Ryan Tullius, Vincent M. Rotello, Graeme Cooke, Nikolaj Gadegaard, Laurence D. Barron, and Malcolm Kadodwala. *Disposable Plasmonics: Plastic Templated Plasmonic Metamaterials with Tunable Chirality*. Advanced Materials, 2015. **27**(37): p. 5610 – 5616.
3. Calum Jack, Affar S. Karimullah, Ryan Tullius, Larousse Khosravi Khorashad, Marion Rodier, Brian Fitzpatrick, Laurence D. Barron, Nikolaj Gadegaard, Adrian J. Laphorn, Vincent M. Rotello, Graeme Cooke, Alexander O. Govorov, and Malcolm Kadodwala, *Spatial Control of Chemical Processes on Nanostructures through Nano-Localized Water Heating*. Nature Communications, 2016. **7**: p. 10946.
4. Calum Jack, Affar S. Karimullah, Ross Leyman, Ryan Tullius, Vincent M. Rotello, Graeme Cooke, Nikolaj Gadegaard, Laurence D. Barron, and Malcolm Kadodwala, *Biomacromolecular Stereostructure Mediates Mode Hybridization in Chiral Plasmonic Nanostructures*. Nano Letters, 2016. **16**(9): p. 5806 – 5814.
5. Ryan Tullius, Geoffrey W. Platt, Larousse K. Khorashad, Nikolaj Gadegaard, Adrian J. Govorov, Affar S. Karimullah, and Malcolm Kadodwala, *Superchiral plasmonic phase sensitivity for fingerprinting of protein interface structure*. ACS Nano, Accepted.

Acknowledgements

Firstly, I would like to start by expressing my gratitude to my supervisor, Professor Malcolm Kadodwala. Without his continuous support and encouragement throughout, this would not have been possible. I would also like to express my sincere thanks to our PostDoc, Dr Affar Karimullah, who has been at the forefront of helping to make this project a success, with his experience and expertise proving to be invaluable throughout, especially with the numerical simulations performed in this thesis. Additionally, thanks to my fellow PhD students; Dr Calum Jack, Marion Rodier, Chris Kelly, and Oriol Roig for all their help and encouragement through the years. With a special mention to Shun Hashiyada, who visited the lab for two extended periods of time, and provided much entertainment and discussion.

I would also like to express my thanks to the other academic staff within the School of Chemistry. Particularly, Dr Adrian Laphorn, who provided many of the protein samples used throughout this thesis, and for his advice and expertise on handling these proteins. As well as Professor Graeme Cooke, for allowing me to use his lab space, and giving his advice on all things organic. Thanks also to all the staff at the JWNC, and members of the Gadegaard group in the School of Engineering, who assisted with the sample fabrication. Many thanks must also go to our international collaborators; Professor Vince Rotello, who allowed me to visit his lab in Massachusetts, USA and provided many suggestions and discussions over the years, and Professor Alexander Govorov and Dr Larousse Khorashad in Ohio, USA for contributing to the numerical simulations. Additionally, sincere thanks to Avacta Life Sciences who provided all of the Affimer samples used in chapter 5 of this thesis.

Finally, many thanks must also go to my family for their infinite support and guidance throughout my time here. Especially my parents, and my wife Jenna, who without them, I may never have finished (or started) this PhD. However, this thesis is dedicated to two very important people, who have given me the purpose to finally complete this thesis for them; my son Josh, and my Dad. I hope this would have made you both proud.

Author's Declaration

I declare that, except where explicit reference is made to the contribution of others, this thesis is the result of my own work, and has not been submitted for any other degree at the University of Glasgow, or any other institution.

Ryan Tullius

August 2017

Chapter 1: Introduction

1.1 Thesis Overview

Metamaterials are artificially structured materials comprised of individual structures much smaller than the wavelength of light [1]. In contrast to bulk materials, where the properties are determined by the intrinsic chemical constituents of the system, metamaterials rely on the specific structures created within the material. With the optical properties of the material being controlled by the size, shape, and arrangement of the constituent structures [2, 3]. Allowing these materials to manipulate electromagnetic (EM) waves in interesting ways, and produce properties that would not be achievable from bulk materials [4].

Throughout this thesis, we will be utilising injection moulded substrates as a high-throughput method of characterising and detecting changes in biological systems, such as protein structural changes. Previously, chiroptical spectroscopies, such as circular dichroism (CD) and optical rotation (OR), have been used to probe chirality and orders of structure within biological samples. However, the low sensitivity of these methods has limited their use when measuring samples of increasingly small concentrations. More recently, chiroptical spectroscopy has attracted further interest when it was theorised that electromagnetic fields could exist that produce a greater chiral asymmetry than that of circularly polarised light (CPL), termed 'superchiral' [5]. It was then theorised that these superchiral fields could be significantly more sensitive to the structure of biological molecules compared with circularly polarised light, and could increase the sensitivity of chirally sensitive spectroscopy techniques. Experimentally, spectroscopic measurements that exploited these fields of enhanced chirality were first demonstrated by Hendry et al. in 2010, where they showed that chiral electromagnetic fields generated around chiral gold nanostructures were sensitive to different structural motifs in proteins [6]. Additionally, these experimental results also reported that the sensitivity of these generated chiral fields were enhanced by six orders of magnitude, relative to conventional chiroptical techniques, with the ability to detect picogram quantities of protein.

In the first results chapter, chapter 4, we use these injection moulded chiral substrates to further investigate the chiral field enhancement reported in previous studies [6]. Two proteins from the Shikimate pathway, a seven step metabolic pathway found in plants and bacteria, are investigated due to each protein having well characterised higher order structural changes upon specific ligand binding. Optical rotatory

dispersion (ORD) spectra are measured from the chiral nanostructures, with the same $\Delta\Delta\lambda$ parameter introduced in the original experimental study being used to characterise the changes observed. This parameter essentially measures the changes in the effective refractive index on the asymmetry of the generated chiral fields around the nanostructures. Hence, the basis of 'superchiral polarimetry' employed here, is the spectral position dependence of the plasmonic resonance on the dielectric environment around the nanostructure surface. Conventional chiroptical spectroscopy, such as circular dichroism (CD), can routinely only detect changes in the secondary and, to a limited extent, tertiary structure of proteins. The two proteins investigated in this chapter, both undergo changes in the higher order structure upon ligand binding, with CD measurements recorded for each protein showing no sensitivity to these changes. However, we demonstrate that superchiral polarimetry is sensitive to the higher order structural changes induced within both proteins, due to the anisotropy of the protein structure, in agreement with the early published results using this property to discriminate between proteins with high α -helical content, or high β -sheet content [6].

The detection of conformational changes in higher order protein structure, using ORD spectra from the chiral nanostructures, relies on an interpretation based on changes in the effective refractive index on the asymmetry of the generated chiral fields. This is a rather simplistic interpretation of the data used to characterise protein structural differences, and when examined theoretically, produces much smaller changes than are observed from the experimental results [7]. This shows that there may be other factors that lead to the significant sensitivity enhancement that is observed. In chapters 5, 6, and 7, we will move away from the more simplistic ORD interpretation seen in chapter 4, and develop a greater understanding of the chiral nanostructures by recording reflectance measurements for each experiment. When reflectance spectra are recorded from the chiral nanostructures used throughout this thesis, an electromagnetically induced transparency (EIT) like behaviour occurs. EIT is a quantum interference effect that appears in atomic systems consisting of three levels, resulting in a sharp transmission window within a broad reflection or absorption band. However, the plasmonic analogue of EIT derives from the strong coupling between bright and dark modes of the structure, to create a narrow transparency window within a broad reflectance spectrum [8-10]. With the strength of this coupling affecting the optical properties of the metamaterial.

In chapters 5, 6, and 7, a new parameter will be introduced to characterise the changes that occur in the optical spectra, as a result of biological samples being

introduced to the nanostructure surface. This parameter $\Delta\Delta S$, the change in the separation of the reflectance dips separated by the narrow transparency window, essentially measures the asymmetry in the coupling of the two plasmonic modes for the chiral nanostructures. In chapter 5, three biological molecules consisting of the same protein scaffold, called Affimers, were immobilised on the nanostructure surface with three different well-defined orientations. We show that one of the orientations can be easily distinguished using the experimental $\Delta\Delta S$ parameter, but the other two orientations produce similar responses to each other, and therefore cannot be easily differentiated. However, a simple coupled oscillator model can then be introduced to theoretically model the experimental reflectance spectra for each measurement. This coupled oscillator model considers the coupling between the two oscillators, as well as the phase of the bright and dark oscillator, θ and ϕ respectively. The coupling of the two oscillators is related to the $\Delta\Delta S$ parameter measured experimentally, but has a much higher inherent error. However, asymmetries in the two theoretical phase parameters, $\Delta\Delta\theta$ and $\Delta\Delta\phi$, do show differences relative to the orientation of the biomaterial at the surface. With all three orientations of the Affimer proteins becoming easily distinguishable, when measuring retardation phase changes in the model values. Showing that the retardation phase changes are an incisive probe into the orientation of biomolecules at the nanostructured surface.

In chapter 6, both the experimental $\Delta\Delta S$, and the two theoretical phase parameter asymmetries are used to detect ligand binding and conformational changes induced upon the cancer relevant protein, Heat shock protein 90 (HSP90). By attaching this protein to the nanostructure surface with two different immobilised orientations, and increasing the concentration of the inhibitor ligand introduced, a fingerprint of the protein-ligand interactions can be obtained. With the orientation of this immobilised protein being shown to affect the sensitivity of the phenomena to any ligand induced changes at low concentrations. Here, the experimental $\Delta\Delta S$ parameter, and the modelled phase asymmetry parameters are shown to be in good agreement with each other, validating the sensitivity of the measurement. With the modelled phase parameters being shown to be a slightly more incisive probe into the conformational changes that occur, for both orientations of the HSP90 protein, upon the addition of increasing concentrations of the inhibitor ligand, 17-AAG.

Finally, in chapter 7, we will examine how small concentration changes of specific proteins in human blood serum, can affect the structure and composition of the protein corona at the nanostructured surface. The $\Delta\Delta S$ parameter will be used to experimentally measure the effect of increasing the immunoglobulin G (IgG)

concentration within human blood serum solutions. It will be shown that when the stock serum solution is diluted in a standard buffer, both low and high elevated levels of IgG in the solution will exhibit the same response. Resulting in various levels of elevated IgG spiked serums being indistinguishable from each other, due to the composition of the protein corona at the nanostructured surface. To resolve this issue, the effect of increasing the ionic strength of the dilution buffer was investigated. This would increase the electrostatic screening in the solution, and will be shown to lower the coverage of the protein corona on the plasmonic surface. Overall, increasing the ionic strength of the dilution buffer for the spiked serum solutions will be shown to increase the detection limit for elevated IgG levels, due to the lower corona coverage, into the physiologically relevant range required in clinical applications. This represents the first step in creating a commercially viable, high-throughput biosensing system, utilising the effects of chiral molecules upon the superchiral fields generated in chiral metamaterials. Although this is an early stage investigation into these effects, results from a complex system (such as human blood serum solutions) shown here, already demonstrate the potential of this phenomenon at probing the biological structure and composition at metamaterial surfaces.

1.2 References

1. Liu, N., et al., *Stereometamaterials*. Nature Photonics, 2009. **3**(3): p. 157-162.
2. Kelly, K.L., et al., *The Optical Properties of Metal Nanoparticles: The Influence of Size, Shape, and Dielectric Environment*. Journal of Physical Chemistry B, 2003. **107**(3): p. 668-677.
3. Murray, W.A. and W.L. Barnes, *Plasmonic materials*. Advanced Materials, 2007. **19**(22): p. 3771-3782.
4. Liu, Y. and X. Zhang, *Metamaterials: a new frontier of science and technology*. Chemical Society Reviews, 2011. **40**(5): p. 2494-2507.
5. Tang, Y. and A.E. Cohen, *Optical chirality and its interaction with matter*. Physical Review Letters, 2010. **104**(16): p. 163901.
6. Hendry, E., et al., *Ultrasensitive detection and characterization of biomolecules using superchiral fields*. Nature Nanotechnology, 2010. **5**(11): p. 783-787.
7. Hendry, E., et al., *Chiral electromagnetic fields generated by arrays of nanoslits*. Nano Letters, 2012. **12**(7): p. 3640-3644.
8. Liu, N., et al., *Planar metamaterial analogue of electromagnetically induced transparency for plasmonic sensing*. Nano Letters, 2009. **10**(4): p. 1103-1107.
9. Luk'yanchuk, B., et al., *The Fano resonance in plasmonic nanostructures and metamaterials*. Nature Materials, 2010. **9**(9): p. 707-715.
10. Wu, D., et al., *Plasmonic metamaterial for electromagnetically induced transparency analogue and ultra-high figure of merit sensor*. Scientific Reports, 2017. **7**: p. 45210.

Chapter 2: Theory

2.1 Chirality

When Pasteur first postulated the concept of chirality in 1848, he used the term 'dissymmetry' to describe objects 'which differ only as an image in a mirror, differs from the object that produces it'. The word 'dissymmetry' has more recently been replaced by 'chirality' and was first used in this context by Lord Kelvin at the University of Glasgow in 1904. As such, the modern definition of chirality given by Barron, in terms of group theory, states that the criteria "for an object to be chiral is that it must not possess improper rotation symmetry elements such as a centre of inversion, reflection planes or rotation-reflection axes" and so must belong to one of the point groups C_n , D_n , O , T or I [1]. Chirality is not only limited to objects however, and can also be seen in electromagnetics such as circularly polarised light, where the electric field vector of the light rotates either clockwise (right handed) or anticlockwise (left handed) around the axis of propagation and constitutes a helical pattern.

2.1.1 Molecular Chirality

Ever since Pasteur's discovery of right- and left-handed crystals derived from tartaric acid, the interest in molecular chirality has continued to grow [1-3]. Molecules of opposite chirality, called enantiomers, are identical in most regards (e.g. density and molecular weight), however the handedness of a molecule can have an effect on some of its properties; such as odour, potency, and toxicity [4]. In nature most biological molecules which are chiral are found exclusively as one enantiomer, with natural sugars being exclusively right handed and all amino acids (except Glycine, which is not chiral) being exclusively left handed [5]. This homochirality in nature is of particular importance, due to the fact that the handedness of a molecule strongly affects how it interacts with other chiral molecules. This has played a significant role in drug discovery, as one enantiomer of the drug can have a drastically different effect to the other enantiomer, often with one having therapeutic activity and the other causing serious side effects [6, 7]. With most drugs being synthesised as a racemic mixture, it has become ever important to differentiate these molecules by their respective enantiomers. This can be achieved using another property possessed by molecules of different chirality, called optical activity.

2.2 Optical Activity

Natural optical activity can be defined as a system which has a differential response to left- and right- circularly polarised light (CPL), without influence from external forces such as an applied magnetic field [1]. Natural optical activity can then also be broken down into electronic optical activity and vibrational optical activity. Where electronic optical activity enables the measurement of circular dichroism (CD) and optical rotation (OR), and vibrational optical activity gives rise to infrared (IR) measurements and Raman optical activity (ROA). All of the spectroscopic measurements performed throughout this thesis rely on electronic natural optical activity, so vibrational optical activity will not be discussed further in this thesis.

For circularly polarised light, the tip of the electric field vector produces a circle with time, perpendicular to the axis of propagation. This circular polarisation is said to be right-handed if the electric field vector rotates clockwise when looking towards the source of light, and left-handed when the electric field vector rotates anticlockwise.

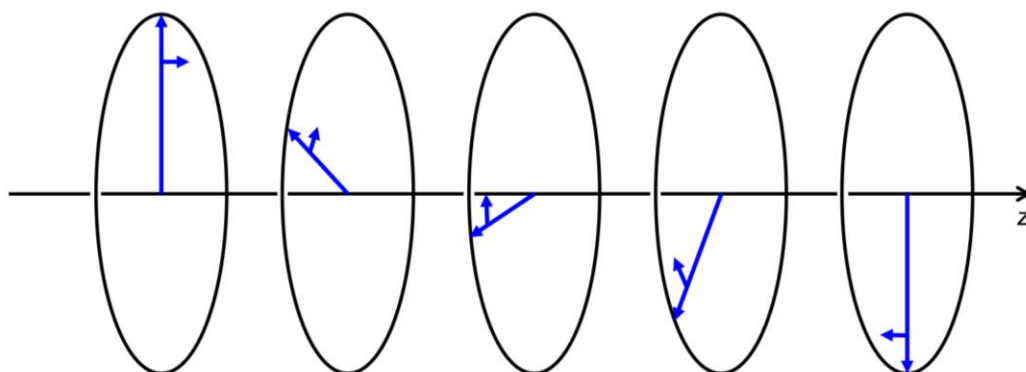


Figure 2.01 Electric field vectors of circularly polarised light propagating along z . Vectors rotate clockwise when viewed in the $-z$ direction showing right-handed polarisation.

2.2.1 Optical Rotation

From this definition of circularly polarised light, linearly polarised light can be regarded as a superposition of equal amplitude left- and right-circularly polarised light, where the orientation of the plane of polarisation is a function of the relative phases of both component beams. When linearly polarised light propagates through an optically active medium, the two circular components (left- and right-handed CPL) travel at different velocities. This difference in velocities of the two components would introduce a phase difference between them, and this would change the orientation of the plane of polarisation, α (Figure 2.02). If the medium was not optically active (e.g.

an achiral medium) the polarisation of the linear light beam would remain unchanged, as there would be no difference in the velocities of the left- and right-circularly polarised components, and therefore no phase difference between them.

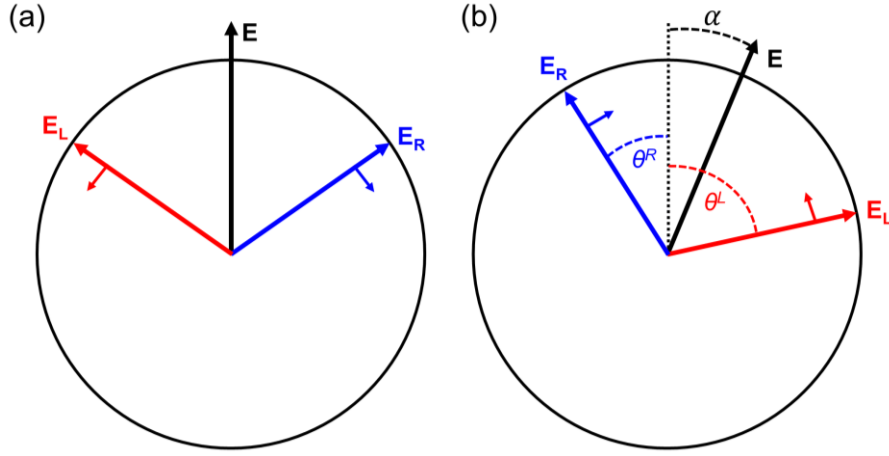


Figure 2.02 (a) Electric field vector of linearly polarised light split into the two components of left- and right-circularly polarised light propagating out of the page, (b) electric field vector rotated at a further point of propagation through an optically active medium.

The rotation of the polarisation of a linearly polarised light beam gives rise to the effect known as optical rotation. When a linearly polarised light beam of angular frequency $\omega = 2\pi c/\lambda$ enters a transparent optically active medium at point $z = 0$, then at any given instant \mathbf{E}_L and \mathbf{E}_R are the same angle from the plane of propagation at that point, $z = 0$ (Figure 2.02(a)). Then at the same instant, at some point $z = l$, in the optically active medium, the electric field vectors \mathbf{E}_L and \mathbf{E}_R are orientated at angles:

$$\theta^L = 2\pi cl/\lambda v^L \quad (2.2.1)$$

$$\theta^R = 2\pi cl/\lambda v^R \quad (2.2.2)$$

These changes are for \mathbf{E}_L and \mathbf{E}_R respectively from \mathbf{E} at $z = 0$, as shown in Figure 2.02(b), where v^L and v^R are the velocities of the left- and right-circularly polarised components within the medium. The angle of rotation of the linearly polarised light beam, in radians, becomes:

$$\alpha = \frac{1}{2}(\theta^L + \theta^R) = \frac{\pi cl}{\lambda} \left(\frac{1}{v^L} - \frac{1}{v^R} \right) \quad (2.2.3)$$

As the refractive index is $n = c/v$, the angle of rotation per unit length in equation 2.2.3 can be written as:

$$\alpha = \frac{\pi}{\lambda} (n^L - n^R) \quad (2.2.4)$$

This optical rotation, the difference between the refractive indices n^L and n^R for left- and right-circularly polarised light respectively in the medium, is a function of circular birefringence. When this occurs, if the medium rotates the plane of polarization clockwise when looking towards the source of the light (as occurs in Figure 2.02(b)) the medium is classed as *dextro rotatory*, and if it rotates the plane of polarisation anticlockwise then it is said to be *laevo rotatory*.

2.2.2 Circular Dichroism

In an optically active medium, since the refractive index is different for both \mathbf{E}_L and \mathbf{E}_R in transparent media, then the absorbance of left- and right-handed circularly polarised light will also be different. Thus, this differential absorption of left- and right-circularly polarised light is known as circular dichroism (CD).

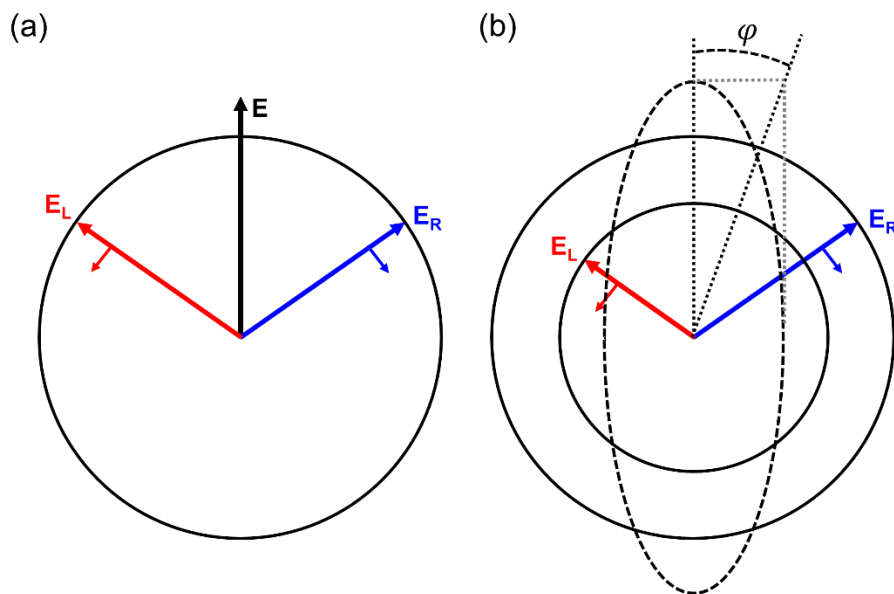


Figure 2.03 (a) Electric field vector of linearly polarised light split into the two components of left- and right-circularly polarised light propagating out of the page, (b) differential absorption of left- and right-CPL causing elliptically polarised light, specified by angle φ .

For circular dichroism, linearly polarised light is no longer rotated, like in optical rotation, but it becomes elliptically polarised due to the differential absorption of the left- and right-circularly polarised light. This differential absorption causes E_L and E_R to become two different amplitudes, which no longer combine to generate linearly polarised light, but create the elliptical polarisation as shown in Figure 2.03(b). The ellipticity (φ) can be calculated from the ratio of the minor and major axes of the ellipse as such:

$$\tan \varphi = \frac{(E_R - E_L)}{(E_R + E_L)} \quad (2.2.5)$$

For ellipticity, when the amplitude of E_R is greater than E_L , it is defined as positive, as a clockwise rotation of the electric field vector of the elliptically polarised beam occurs. Ellipticity is often the unit used when describing CD spectra, however the CD signals are usually very small with most proteins and biological samples showing ellipticities in the range of 10 millidegrees. Other than ellipticity, CD can also be quantified as the differential absorption of E_L and E_R where $A = \log \frac{I_0}{I_t} = \epsilon cl$ and is typically around 10^{-3} absorbance units for protein samples [8, 9].

2.2.3 Optical Rotatory Dispersion

Most applications of optical rotation use the rotation at some transparent wavelength, usually the sodium D line at 589 nm. However, optical rotatory dispersion (ORD) also exists, and measures the unequal rotation of polarisation at different wavelengths. Since both refraction and absorption are related, circular dichroism and optical rotatory dispersion have wavelength dependent spectra that are very close to conventional absorption and refraction. These related spectra for circular dichroism and optical rotatory dispersion in the absorption region are shown in Figure 2.04, and are related together by something known as the Cotton effect. From this relationship, the maximum ellipticity coincides with the optical rotatory dispersion curve at its point of inflection. For optically pure enantiomers, the Cotton effect ORD spectra are always opposite to each other but of equal magnitude.

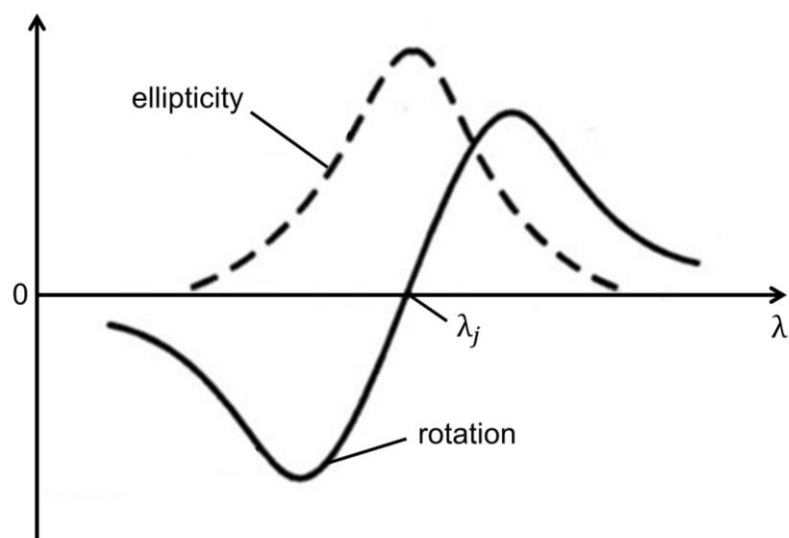


Figure 2.04 Ellipticity and related optical rotatory dispersion curves centred around the electronic absorption wavelength λ_j .

With the Cotton effect, the ellipticity and optical rotatory dispersion always have relative signs to each other, where a positive Cotton effect is seen when the ORD spectra rises to a peak at higher wavelengths and a trough at lower wavelengths (shown in Figure 2.04), and a negative Cotton effect when the ORD spectra is reversed. This is due to the fact that CD and ORD can be related to each other by a Kramers-Kronig (KK) relation [10], resulting in the relationship seen in Figure 2.04.

2.3 Superchirality

2.3.1 Superchiral Fields

Chiral light-matter interactions are relatively weak, as shown for circular dichroism spectroscopy, where absorption differences are typically $<10^{-3}$. This can be thought of as a consequence of the mismatch between the helical pitch of circularly polarised light, and the relatively small size of chiral molecules such as proteins. The circularly polarised wave has a helicity that depends upon the wavelength of the light, so that the circularly polarised field rotates a full 360° in one wavelength (typically a few hundred nanometres for UV/Visible light). This is considerably larger than the size of chiral molecules (around the tens of nanometres) so the circularly polarised field undergoes a barely perceptible twist over the distance of molecular dimensions [11].

In recent years, it was recognised that an enhanced dissymmetry should occur if the field lines were reoriented over a distance that is much shorter than the wavelength, ideally close to the dimensions of molecules [12, 13]. When this occurs, the spatial scale of molecular chirality and the chirality of the light would match. It was identified that chiral interactions required a time-even pseudoscalar to fully describe the chirality of electromagnetic fields. In 1964, Lipkin introduced a series of conserved quantities, which he called 'zilch', to describe electromagnetic waves in a vacuum [14]. However, these quantities were dismissed as having no physical significance by both Lipkin, and others after him [15, 16]. It has since been realised that one of these quantities satisfies the need for a time-even pseudoscalar, and has been termed optical chirality, C [12].

$$C = \frac{\varepsilon_0}{2} \mathbf{E} \cdot \nabla \times \mathbf{E} + \frac{1}{2\mu_0} \mathbf{B} \cdot \nabla \times \mathbf{B} \quad (2.3.1)$$

Where ε_0 and μ_0 are the permittivity and permeability of free space respectively, and \mathbf{E} and \mathbf{B} are the time-dependent electric and magnetic fields. This optical chirality parameter captures the degree to which the electric and magnetic field vectors, \mathbf{E} and \mathbf{B} , wrap around a helical axis at each point in space, i.e. the tightness of the helix. In circular dichroism, the dissymmetry factor, g , is a dimensionless quantity that measures the enantioselectivity of a system [17]:

$$g = \frac{A^L - A^R}{\frac{1}{2}(A^L + A^R)} \quad (2.3.2)$$

Where the superscripts L and R refer to left- and right-circularly polarised light respectively. This dissymmetry factor, g , was then rewritten to include the optical chirality parameter, C [12, 13]:

$$g = g_{CPL} \left(\frac{cC}{2U_e\omega} \right) \quad (2.3.3)$$

Where g_{CPL} is the dissymmetry factor under circularly polarised light, c is the speed of light, C is the optical chirality, U_e is the local electric energy density, and ω is the angular frequency. Equation 2.3.3 shows that, unlike circular dichroism, the magnitude of the dissymmetry factor, g , is dependent on the optical chirality, C , and not solely governed by the chirality of matter. Since the field vectors completely rotate once per wavelength at a constant rate for circularly polarised light, the quantity $cC/2U_e\omega$ equals 1. Therefore, to increase the dissymmetry factor an increase in the

optical chirality, C , leading to the quantity $cC/2U_e\omega$ being greater than 1 in some regions of space would be necessary. When this occurs, these fields have been termed as ‘superchiral’ fields, as they have a much greater helicity than that of circularly polarised light.

The first time that these ‘superchiral’ fields were produced was by creating an optical standing wave constructed of two counter propagating waves of circularly polarised light with opposite handedness, equal frequency, and a slightly different intensity. This was generated by reflecting circularly polarised light of one handedness off of a partially reflecting mirror at normal incidence, which creates the perfect conditions to generate ‘superchirality’ [12]. Now, the most common and simplest way to get an enhancement of the optical chirality, C , is through the use of plasmonic nanostructures [18-22]. By using plasmonic nanostructures, strong electric and magnetic fields in the near field of the nanostructure can be created using visible/IR radiation. To get the optimum enhanced optical chirality, C , over a continuous region it has been shown that the nanostructures must be designed to optimise this parameter by using planar chiral nanostructures, ideally without sharp corners [19]. The first experiment to utilise this theory of ‘superchiral’ fields, by using chiral gammadion nanostructures, showed a dissymmetry enhancement of $\sim 10^6$ when detecting biomolecules, compared with using circularly polarised light alone for biomolecular detection [18].

2.4 Plasmonics

2.4.1 Plasmonic Oscillations

Plasmonic oscillations can occur in metallic thin films (at metal-dielectric interfaces) [23], and metallic nanostructures [24], typically made of gold or silver. This is due to the large distance between the valence electrons and positive core of a metal ion, causing them to be weakly bound to each other. When these atoms come together to form a thin film or nanoparticle, the valence electrons are influenced by the potential energy of all other atoms in the system. This allows the valence electrons to freely move throughout the system around a background of positive ion cores, essentially generating an electron cloud or plasma. These electrons move throughout the entire system in a random motion and keep the overall charge of the system at 0. When an electric field is applied to the system, the electron plasma is displaced by a distance, x , Figure 2.05(b).

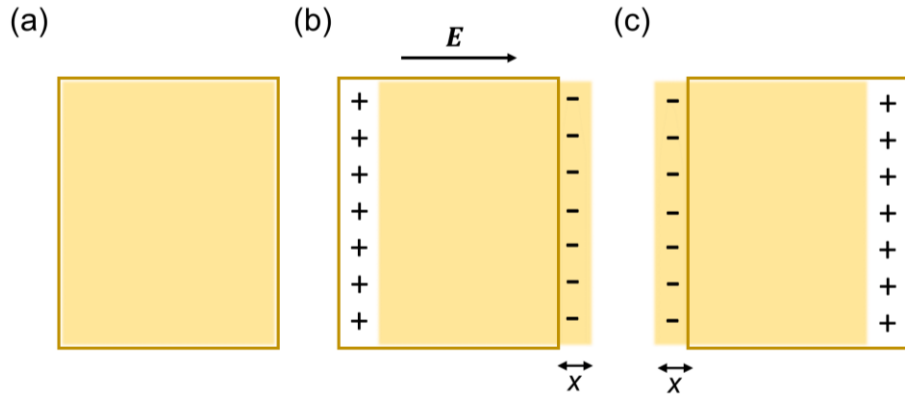


Figure 2.05 Graphical representation of plasmonic oscillations. (a) bulk metal with no electric charge applied, (b) shows after application of an electric field causing displacement of the electron cloud, (c) shows oscillation of electron cloud in opposite direction when electric field turned off.

When the external electric field is switched off, the electrons in the metal will be accelerated by the surface charges created back to their original position. Once they have returned to their original positions (Figure 2.05(a)), they have acquired momentum and will then keep moving in the other direction to create an electric field of opposite sign from before, Figure 2.05(c). This will be repeated in each direction and hence produce a plasmonic oscillation with a plasma frequency, ω_p [25, 26]:

$$\omega_p^2 = \frac{ne^2}{m\epsilon_0} \quad (2.4.1)$$

Where n is valence electron density, e is the charge of an electron, m mass of an electron, and ϵ_0 is the permittivity of free space. This collective oscillation can then be thought of as an oscillation that is produced by an electric field, due to all the electrons in the system, called a bulk plasmon, as it is throughout the bulk material.

2.4.2 Surface Plasmon Polaritons

Surface plasmon polaritons (SPP) are electromagnetic excitations that propagate along a metal-dielectric interface, and are evanescently confined in the perpendicular direction. These electromagnetic surface waves occur via the coupling of the electromagnetic fields to the oscillating electron plasma of the metal [27]. This happens when an incident electromagnetic wave, creates a charge oscillation on the metal surface that propagates along the surface at the metal-dielectric interface. The

collective oscillation of these surface charges excites the surface plasmon polaritons with a different frequency than the bulk plasma frequency seen in equation 2.4.1, and now becomes:

$$\omega_{spp} = \frac{\omega_p}{\sqrt{1 + \epsilon_d}} \quad (2.4.2)$$

Where ω_p is the bulk plasma frequency, and ϵ_d is the relative permittivity of the dielectric. From this, it can be seen that the surface plasmon polariton frequency is lower than the bulk frequency, so can be excited at lower energies.

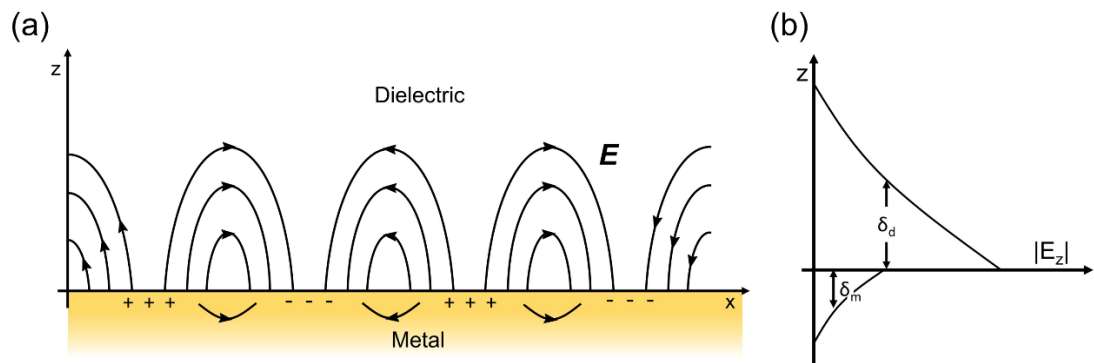


Figure 2.06 Graphical representation of (a) the surface charges and resultant electromagnetic wave at the metal-dielectric interface, and (b) the electric field strength in the z direction for both the dielectric and metal. δ_d and δ_m are the penetration depths of the SPP wave into the dielectric and metal respectively.

Once the surface plasmon polariton mode has been excited it will propagate along the metal surface, however it will gradually attenuate due to the losses arising from absorption in the metal. Therefore, the propagation length of the surface plasmon is limited by the internal damping of the metal, and is dependent on the dielectric constant of the metal and the incident wavelength of light. As a result of this surface propagating wave, associated non-propagating evanescent fields extend perpendicular to the surface into both the metal and the dielectric (Figure 2.06). The distance that these fields extend into the metal and dielectric both depend on the relative permittivities of the two interface materials, and decay exponentially with distance from the interface (Figure 2.06(b)). The distance that the evanescent fields extend can be thought of as penetration depths, δ_m and δ_d , for the metal and dielectric respectively. For example, with gold and water as the metal and dielectric, the penetration depths with incident light at 630 nm are 29 nm for δ_m and 162 nm for δ_d [28]. It can be seen that the penetration depth for the dielectric is much larger than for

the metal, and as they decay exponentially are much more concentrated near to the interface.

2.4.3 Plasmon Excitation

For surface plasmon polaritons, the parameter of surface plasmon polariton dispersion can be obtained by solving Maxwell's equations for the appropriate conditions to give [29]:

$$k_{spp} = k \sqrt{\frac{\epsilon_d \epsilon_m}{\epsilon_d + \epsilon_m}} \quad (2.4.3)$$

Where k_{spp} is the wavevector of the surface plasmon, k is the wavevector of a photon in free space, and ϵ_d and ϵ_m are the relative permittivities of the dielectric and the metal respectively. Typically, the square root term in equation 2.4.3 $\left(\sqrt{\frac{\epsilon_d \epsilon_m}{\epsilon_d + \epsilon_m}}\right)$ is positive and larger than 1, as ϵ_m must be large and negative, and ϵ_d must be small and positive for a surface plasmon resonance to exist, and is fulfilled at metal-dielectric interfaces for visible frequencies [30]. For example, gold has a ϵ_m value at 620 nm of $-9.728 + i1.314$, and silicon oxide has a ϵ_d value of 2.127 [31, 32]. From equation 2.4.3, it can be seen that the momentum of the surface plasmon polariton ($\rho = \hbar k_{spp}$) is larger than the momentum of light in free space ($\rho = \hbar k$) at the same frequency, giving a mismatch in the momentum of the light and the surface plasmon polariton [29].

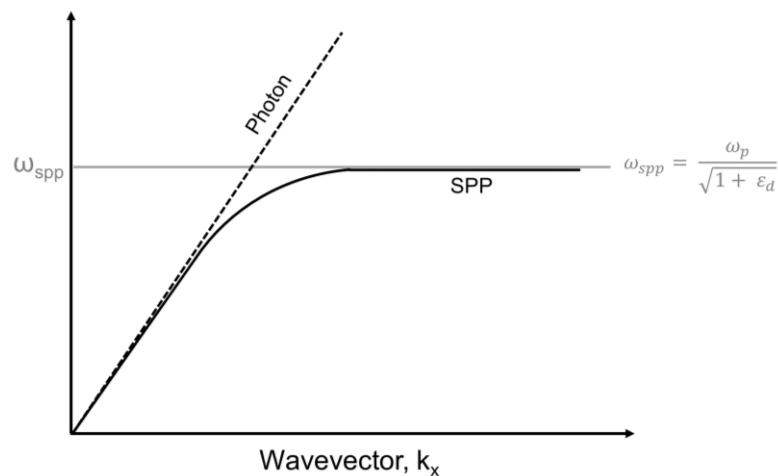


Figure 2.07 Dispersion curves for surface plasmon polariton, and light in a vacuum. Wavevector for SPP is always higher than for light at the same frequency.

From this momentum mismatch, due to the wavevector of the SPP always being larger than the wavevector of a photon (Figure 2.07), light illuminating a smooth metal surface cannot be coupled to the surface polaritons directly. To combat this problem, the momentum of the light and surface plasmon polariton must be matched using prism couplers or grating features [33, 34]. The two most popular methods for prism coupling are the Kretschmann [35], and the Otto [36] configurations.

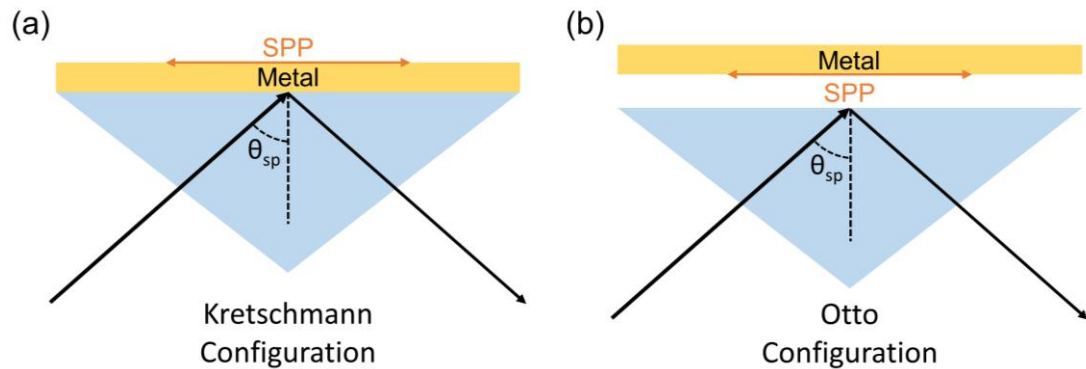


Figure 2.08 Prism coupling methods of SPP excitation at a metal-dielectric interface. (a) Kretschmann configuration, and (b) Otto configuration.

In the Kretschmann configuration, the incident light passes through a dielectric prism at an angle of incidence greater than that of total internal reflection. The wavevector of the light increases through the prism and tunnels through the metal film, where the light couples to the surface plasmon resonances. In the Otto configuration, the light from the prism tunnels through a small air gap between the prism and the metal, coupling to the SPP at that interface, so can be used for thicker metal films than the Kretschmann configuration.

Using the same principles as the prism coupling, surface plasmons can also be coupled by using a diffraction grating to match the momentum of the light and the SPP. Some of the diffracted components of the light will match the wavevector of the SPP, and these can couple to give an excitation.

2.4.4 Localised Surface Plasmon Resonances

Similar to the surface plasmon oscillations that occur in metal films, at the metal-dielectric interface, plasmon oscillations can also occur in metallic nanostructures and nanoparticles. Unlike the surface plasmons on the metal films, these localised surface plasmons can be excited directly through simple reflection. This is possible since the

plasmons are no longer propagating, so the momentum matching conditions for the surface plasmon is not required [37].

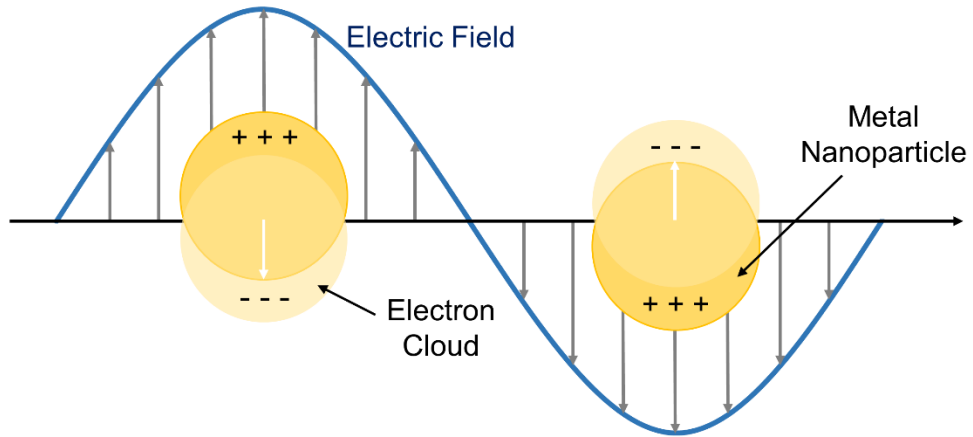


Figure 2.09 Graphical representation of localised surface plasmons on metallic nanospheres.

Localised surface plasmons occur when incident light interacts with metallic nanoparticles (such as nanospheres) that are much smaller than the incident wavelength (Figure 2.09). Instead of these plasmons propagating along the surface of a metal film, the plasmons oscillate locally around the nanoparticle. This oscillation results in evanescent fields that extend around the nanoparticle surface into the dielectric environment, the same as for surface plasmons, however the decay length of these fields for localised surface plasmons can be 40-50 times shorter than that of SPPs [38]. These localised surface plasmon resonances, having such a short decay length from the nanoparticle, are sensitive to the dielectric constant or refractive index ($\epsilon = n^2$) of the dielectric that surrounds them. So, by adsorbing a molecule or biomaterial to the surface of the nanoparticles, the position of the resonance would shift due to the change in the local environment around the metallic nanostructure. This shift can be calculated through:

$$\Delta\lambda = m\Delta n \left[1 - \exp\left(-2d/l_d\right) \right] \quad (2.4.4)$$

Where m is the bulk refractive index response of the nanoparticles, Δn is the change in the refractive index from the adsorbate, d is the thickness of the adsorbed layer, and l_d is the evanescent field decay length. This relationship forms the basis of most LSPR shift sensors that use a wavelength shift for detection. However, the line shape and position of the LSPR spectra strongly depends on many factors, such as the material, shape, size, and local dielectric properties of the nanoparticles [39-41]. For

example, where spherical nanoparticles will have only one resonance, metallic nanorods split the plasmon resonance into a low- and high-energy resonance. This occurs as the surface plasmons are unevenly distributed in nonspherical nanoparticles. So for the metallic nanorods, the high energy resonance corresponds to the plasmon oscillations in the direction perpendicular to the major axis (or transverse mode), while the lower energy resonance arises from the plasmon oscillations along the major axis (or longitudinal mode) of the nanorods [42].

2.4.5 Plasmonic Hybridisation

The surface plasmon polariton (SPP) and localised surface plasmon (LSP) described in the previous sections have been for individual plasmon resonances. However, these plasmon resonances can essentially couple to each other when the nanostructures are in close enough proximity to each other, or aggregation of the nanoparticles begins to occur [43]. This electromagnetic coupling has previously been observed between metallic films-nanostructures [44], solid-solid structures [45], solid-inverse structures [46], and inverse-inverse structures [47] within a plasmonic system. In all of these systems, it has been shown that the coupling of two (or more) plasmonic structures leads to hybridised plasmon modes. To characterise the hybridisation of these plasmon modes, a simple model was proposed where the plasmon coupling in metallic nanostructures could be thought of as an analogue to molecular orbital hybridisation [48]. A simple example of this hybridisation model, and one that has been demonstrated many times, is the dipole-dipole interactions between a metallic nanorod dimer [45, 49]. In this system when the gap between the two metallic nanorods becomes small enough to create overlap between the individual plasmon modes on each of the rods, in the longitudinal direction for Figure 2.10, there is a strong near field interaction between the nanoparticles. This interaction is the basis of the hybridisation of the plasmon modes on each individual particle, and forms the coupled modes over the whole structure. As shown in Figure 2.10, when the individual particles of the dimer couple to each other, they can couple to form both in-phase and out-of-phase combinations.

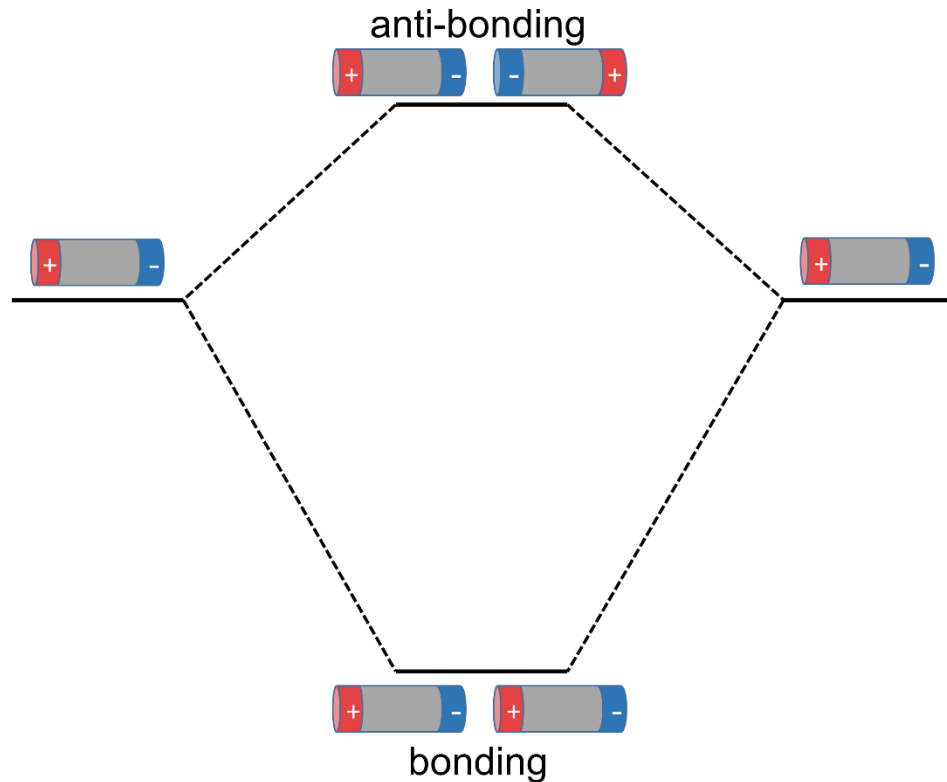


Figure 2.10 Hybridisation (energy level) diagram of two nanorods aligned longitudinally to each other and separated by a small gap.

So, when the plasmon oscillations on each individual nanorod are in-phase with each other, along the aligned axis, then a symmetric mode occurs. Conversely, when the oscillations of the individual nanorods are 180° out-of-phase along the aligned axis, the anti-symmetric mode occurs. The molecular analogy used in this model means that these in-phase and out-of-phase modes correspond to the bonding and anti-bonding orbitals respectively. Similar to the bonding and anti-bonding orbitals used in molecular orbitals, the in-phase and out-of-phase modes of the plasmon hybridisation model differ in energies. The in-phase (bonding) mode has a lower energy and an enhanced electromagnetic field in the gap between the two rods, whereas the out-of-phase (anti-bonding) mode has a higher energy, and a negligible electromagnetic field in the gap between the nanorods [50]. The in-phase mode of the system typically has a large dipole moment, and interacts strongly with the incident light. However, the out-of-phase mode only has a small dipole moment as the dipoles in the individual nanoparticles are aligned anti-parallel. This out-of-phase mode, due to the small dipole moment, does not interact strongly with the incident light. As a result of this, the in-phase and out-of-phase modes are often called the bright and dark modes of the system. Although, this hybridisation model has been applied to simple structures,

such as the metallic nanorods, it can also be applied to more complex structures by analysing them in terms of their constituent parts (such as nanospheres, nanoshells, etc.) [48].

2.5 Interference Effects

As mentioned in the previous section, and shown in Figure 2.10, the simple case of two metallic nanorods can couple to each other to form in-phase and out-of-phase plasmon modes. The in-phase mode, has a strong dipole moment and can interact directly with the incident light, whereas the out-of-phase mode has a negligible dipole moment and cannot interact directly with the incident radiation. These modes are often termed as the bright and dark modes of the system for this reason. To understand the interference effects within these systems, the simplest analogy is to relate the classical model of two coupled harmonic oscillators, driven by an external force, to the metamaterial systems [51].

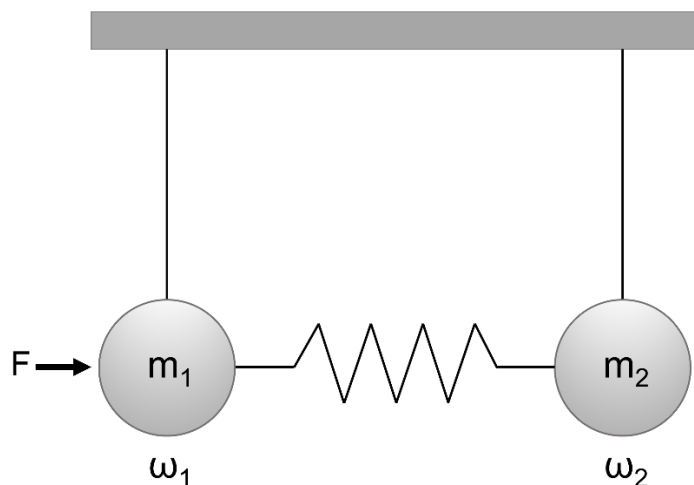


Figure 2.11 Schematic of the coupled oscillator model between bright and dark modes.

In this system, an external force (corresponding to the electromagnetic field) is applied to one of the oscillators. When the external force, F , is applied to the mass, m_1 , it begins to oscillate at the frequency, ω_1 . When the resonant frequencies of m_1 and m_2 overlap, the oscillation of m_1 caused by the external force will couple to the mass m_2 and induce an oscillation with a frequency, ω_2 . This oscillation of m_2 cannot be induced by the external force, but only by the oscillation of m_1 . This analogy corresponds to m_1 being the in phase (bright) plasmon mode, and m_2 being the out of phase (dark) plasmon mode. The generation of interference effects are highly

dependent on the relative phase of the coupled oscillators, where the phase difference of the two oscillators can be given by [52]:

$$\varphi_2 - \varphi_1 = \pi - \theta \quad (2.5.1)$$

where the extra phase shift, θ , can be defined as:

$$\theta = \tan^{-1} \left(\frac{\gamma_2 \omega}{\omega_2^2 - \omega^2} \right) \quad (2.5.2)$$

Where γ is the damping parameter, ω is the frequency of the external force, and ω_2 is the resonant frequency of the oscillator. From this it can be seen that a single forced oscillator has a π change in phase when it goes through the resonance ω_2 . This means that below the frequency, ω_2 , the oscillator and the external force are in phase, whereas above the frequency, the oscillator and external force are out of phase with each other. For the two coupled oscillators, at the resonant frequency of the second oscillator, there are two forces acting upon the first oscillator. These two forces are out of phase to each other and would interfere destructively by cancelling each other out, which gives rise to the interference effects within the plasmonic structures [51].

2.5.1 Fano Resonance

A common interference phenomena caused by this coupling of in-phase and out-of-phase plasmon modes is Fano resonance. Fano resonances occur when there is constructive or destructive interference between a narrow discrete state and a broad resonance or continuum.

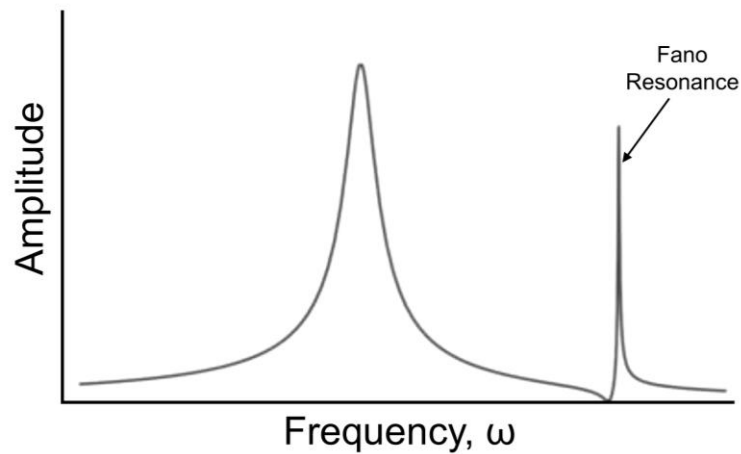


Figure 2.12 Asymmetric Fano resonance produced from the coupling of optically bright and dark plasmon modes.

For plasmonic materials, broad and narrow resonances occur for all eigenmodes of the structures, and so satisfy the condition of a Fano resonance, where the broad and narrow resonances spectrally overlap [53]. Using the analogy of the two coupled nanorod dimers, the bonding mode, or bright mode, has a broadened resonance, and the anti-bonding mode, or dark mode, with no net dipole moment shows a sharp resonance that couple to each other to form the Fano resonance [54]. The Fano resonance, does not display the typical Lorentzian line shape seen for other resonances, but displays a more asymmetric line shape that can be seen in Figure 2.12. With the line shape of the resonance defined by the function:

$$I \propto \frac{(F\gamma + \omega - \omega_0)^2}{(\omega - \omega_0)^2 + \gamma^2} \quad (2.5.3)$$

where ω_0 and γ denote the position and line width of the resonance respectively, with F being the Fano parameter that describes the degree of asymmetry [54].

2.5.2 Electromagnetically Induced Transparency

Electromagnetically induced transparency (EIT) is a quantum interference effect that allows the propagation of light through an atomic medium, and produces a narrow transparency window within an absorption peak [55]. A typical three level EIT system can be seen in Figure 2.13(a).

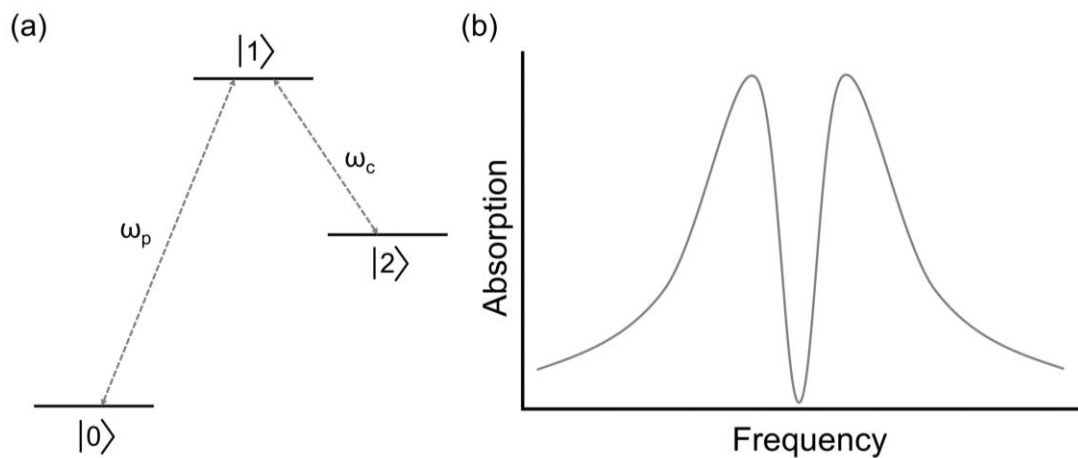


Figure 2.13 (a) Three level EIT system where ω_p and ω_c are the frequency of the probe and coupling beams, and (b) EIT absorption spectra showing a narrow transparency dip within a broad absorption band.

Requirements for EIT in a three-level system are that two of the possible transitions must be dipole allowed, and the other transition must be dipole forbidden, with one of the three states being connected to the other two by two optical fields, as shown in Figure 2.13(a). The system is irradiated with two beams, the probe beam and the coupled beam. The probe and coupled beams have frequencies ω_p and ω_c respectively. When the system is irradiated with a probe beam that is tuned near to the resonance between two of the states, the absorption spectrum of that transition can be measured. However, when a coupling beam that is near the frequency of the resonance of the other dipole allowed transition is used, the transparency window can also be detected by the probe beam. In the three-level exemplar EIT system shown in Figure 2.13(a), the probe beam drives the coupling directly between the $|0\rangle - |1\rangle$ pathway, and once the coupled beam is added, a second pathway occurs between $|0\rangle - |1\rangle - |2\rangle - |1\rangle$. These two pathways interfere destructively with each other, and if energy level $|2\rangle$ has a longer lifetime compared with the other levels, a transparency window appears completely within the absorption line, as shown in Figure 2.13(b) [56].

2.5.3 Plasmonic Electromagnetically Induced Transparency

For plasmonic electromagnetically induced transparency, instead of a three-level system, coherent coupling can occur between two resonances. These resonances can be thought of as the bright and dark resonances of the plasmonic system, like in the nanorod system in section 2.4.5. The bright mode of the system is typically a broad resonance with a large scattering cross section, and the dark mode a sharp resonance with a much larger quality factor. The dark mode of the plasmonic system is analogous to the metastable level $|2\rangle$ in the atomic system. Therefore, when coupling of the bright and dark mode happens, destructive interference between the two modes occurs, and produces the induced transparency window within the absorption line. This is analogous to the atomic system as the two possible pathways that destructively interfere here are the direct excitation of the bright mode by the incident EM field, and the coupling between the bright and dark modes. The strength of the electromagnetically induced transparency depends on the spectral overlap of the resonances, and their coupling strength, where an increase in coupling between the resonances widens and deepens the transparency window [57]. This means the EIT spectra produced by these plasmonic systems can be modified and tuned by varying the coupling of these modes via structural tuning. These EIT like spectra

produced by plasmonic systems have been shown to have excellent potential for sensing applications, with some structures being shown to have refractive index sensitivity of $\sim 588 \text{ nm/RIU}$ [58].

2.5.4 Plasmonic EIT Modelling

Plasmonic electromagnetically induced transparency can be modelled mathematically, to reproduce the spectra created from plasmonic EIT systems. A coupled oscillator model was first proposed by Zhang et al. [57], and variations of this approach have been used by Tassin et al. [59]. The model system used to fit the plasmonic EIT spectra can be described by a set of two coupled harmonic oscillators:

$$\omega_r^{-2}\ddot{p}(t) + \gamma_r\omega_r^{-1}\dot{p}(t) + p(t) = gf(t) - \tilde{k}q(t) \quad (2.5.3)$$

$$\omega_d^{-2}\ddot{q}(t) + \gamma_d\omega_d^{-1}\dot{q}(t) + q(t) = -\tilde{k}p(t) \quad (2.5.4)$$

The radiative (bright) resonator is described by the excitation $p(t)$, with a resonance frequency ω_r , and a damping factor γ_r . Where the dark mode is described by the excitation $q(t)$, with a resonance frequency ω_d , and a damping factor γ_d . The two resonators are coupled by a complex coupling constant \tilde{k} , with the bright mode being driven by an external force $f(t)$, and a constant describing the coupling strength between the oscillator and the external force, g . In addition to some previous utilisations of this coupled oscillator model for plasmonic EIT, two terms are introduced in the solutions, $e^{-i\theta}$ and $e^{-i\phi}$. These terms account for any retardation phase shifts that occur in the bright and dark mode excitations, θ and ϕ respectively. Since both resonators are linearly coupled by the complex coupling coefficient $\tilde{k} = ke^{-i(\omega t)}$, the solutions to equations 2.5.3 and 2.5.4 take the form:

$$p(t) = e^{-i\theta}P(\omega)e^{-i(\omega t)} \quad (2.5.5)$$

$$q(t) = e^{-i\phi}Q(\omega)e^{-i(\omega t)} \quad (2.5.6)$$

From these equations and using an effective medium approximation, an expression can be derived for fitting the reflectivity spectra obtained from plasmonic EIT systems, giving a deeper understanding of EIT metamaterials as a function of their microscopic parameters (Appendix A). This procedure for fitting plasmonic EIT reflectance spectra will be further developed throughout the experimental and results chapters of this thesis.

2.6 References

1. Barron, L.D., *Molecular Light Scattering and Optical Activity*. 2nd ed. 2004: Cambridge University Press.
2. Cahn, R.S., C. Ingold, and V. Prelog, *Specification of Molecular Chirality*. Angewandte Chemie International Edition, 1966. **5**(4): p. 385-415.
3. Barron, L.D., *Symmetry and molecular chirality*. Chemical Society Reviews, 1986. **15**(2): p. 189-223.
4. Harris, A.B., R.D. Kamien, and T.C. Lubensky, *Molecular chirality and chiral parameters*. Reviews of Modern Physics, 1999. **71**(5): p. 1745-1757.
5. Blackmond, D.G., *The origin of biological homochirality*. Cold Spring Harb Perspect Biol, 2010. **2**(5): p. a002147.
6. Brown, C., *Chirality in drug design and synthesis*. 1990: Academic Press.
7. Nguyen, L.A., H. He, and C. Pham-Huy, *Chiral Drugs: An Overview*. International Journal of Biomedical Science : IJBS, 2006. **2**(2): p. 85-100.
8. Kelly, S.M. and N.C. Price, *The use of circular dichroism in the investigation of protein structure and function*. Curr Protein Pept Sci, 2000. **1**(4): p. 349-84.
9. Kelly, S.M., T.J. Jess, and N.C. Price, *How to study proteins by circular dichroism*. Biochimica et Biophysica Acta (BBA) - Proteins and Proteomics, 2005. **1751**(2): p. 119-139.
10. Polavarapu, P.L., *Kramers–Kronig Transformation for Optical Rotatory Dispersion Studies*. Journal of Physical Chemistry A, 2005. **109**(32): p. 7013-7023.
11. Mason, S.F., *Molecular optical activity and the chiral discriminations*. 1982: Cambridge University Press.
12. Tang, Y. and A.E. Cohen, *Optical Chirality and Its Interaction with Matter*. Physical Review Letters, 2010. **104**(16): p. 163901.
13. Tang, Y. and A.E. Cohen, *Enhanced Enantioselectivity in Excitation of Chiral Molecules by Superchiral Light*. Science, 2011. **332**(6027): p. 333-336.
14. Lipkin, D.M., *Existence of a New Conservation Law in Electromagnetic Theory*. Journal of Mathematical Physics, 1964. **5**(5): p. 696-700.
15. Kibble, T.W.B., *Conservation Laws for Free Fields*. Journal of Mathematical Physics, 1965. **6**(7): p. 1022-1026.
16. Przanowski, M., B. Rajca, and J. Tosiek, *On some conservation laws in the Maxwell electrodynamics in vacuum*. Acta physica Polonica. B, 1994. **25**(7): p. 1065-1077.
17. Choi, J.S. and M. Cho, *Limitations of a superchiral field*. Physical Review A, 2012. **86**(6): p. 063834.
18. Hendry, E., et al., *Ultrasensitive detection and characterization of biomolecules using superchiral fields*. Nature nanotechnology, 2010. **5**(11): p. 783-787.
19. Schäferling, M., et al., *Tailoring Enhanced Optical Chirality: Design Principles for Chiral Plasmonic Nanostructures*. Physical Review X, 2012. **2**(3): p. 031010.
20. Meinzer, N., E. Hendry, and W.L. Barnes, *Probing the chiral nature of electromagnetic fields surrounding plasmonic nanostructures*. Physical Review B, 2013. **88**(4): p. 041407.

21. Valev, V.K., et al., *Chirality and Chiroptical Effects in Plasmonic Nanostructures: Fundamentals, Recent Progress, and Outlook*. *Advanced Materials*, 2013. **25**(18): p. 2517-2534.
22. Schäferling, M., et al., *Reducing the Complexity: Enantioselective Chiral Near-Fields by Diagonal Slit and Mirror Configuration*. *ACS Photonics*, 2016. **3**(6): p. 1076-1084.
23. Raether, H., *Surface plasmons on smooth surfaces*. 1988: Springer Berlin Heidelberg.
24. Willets, K.A. and R.P. Van Duyne, *Localized surface plasmon resonance spectroscopy and sensing*. *Annu. Rev. Phys. Chem.*, 2007. **58**: p. 267-297.
25. Pines, D., *Collective Energy Losses in Solids*. *Reviews of Modern Physics*, 1956. **28**(3): p. 184-198.
26. Enoch, S. and N. Bonod, *Plasmonics: from basics to advanced topics*. Vol. 167. 2012: Springer.
27. Maier, S.A., *Plasmonics: fundamentals and applications*. 2007: Springer Science & Business Media.
28. Homola, J., S.S. Yee, and G. Gauglitz, *Surface plasmon resonance sensors: review*. *Sensors and Actuators B: Chemical*, 1999. **54**(1–2): p. 3-15.
29. Junxi, Z., Z. Lide, and X. Wei, *Surface plasmon polaritons: physics and applications*. *Journal of Physics D: Applied Physics*, 2012. **45**(11): p. 113001.
30. Murray, W.A. and W.L. Barnes, *Plasmonic materials*. *Advanced materials*, 2007. **19**(22): p. 3771-3782.
31. Rakić, A.D., et al., *Optical properties of metallic films for vertical-cavity optoelectronic devices*. *Applied Optics*, 1998. **37**(22): p. 5271-5283.
32. Palik, E.D., *Handbook of optical constants of solids*. Vol. 3. 1998: Academic press.
33. Zayats, A.V. and I.I. Smolyaninov, *Near-field photonics: surface plasmon polaritons and localized surface plasmons*. *Journal of Optics A: Pure and Applied Optics*, 2003. **5**(4): p. S16-S50.
34. Zayats, A.V., I.I. Smolyaninov, and A.A. Maradudin, *Nano-optics of surface plasmon polaritons*. *Physics Reports*, 2005. **408**(3–4): p. 131-314.
35. Kretschmann, E. and H. Raether, *Notizen: radiative decay of non radiative surface plasmons excited by light*. *Zeitschrift für Naturforschung A*, 1968. **23**(12): p. 2135-2136.
36. Otto, A., *Excitation of nonradiative surface plasma waves in silver by the method of frustrated total reflection*. *Zeitschrift für Physik*, 1968. **216**(4): p. 398-410.
37. Lis, D. and F. Cecchet, *Localized surface plasmon resonances in nanostructures to enhance nonlinear vibrational spectroscopies: towards an astonishing molecular sensitivity*. *Beilstein journal of nanotechnology*, 2014. **5**(1): p. 2275-2292.
38. Haes, A.J., et al., *A Nanoscale Optical Biosensor: The Long Range Distance Dependence of the Localized Surface Plasmon Resonance of Noble Metal Nanoparticles*. *The Journal of Physical Chemistry B*, 2004. **108**(1): p. 109-116.
39. Kelly, K.L., et al., *The Optical Properties of Metal Nanoparticles: The Influence of Size, Shape, and Dielectric Environment*. *The Journal of Physical Chemistry B*, 2003. **107**(3): p. 668-677.
40. Haes, A.J., et al., *Plasmonic Materials for Surface-Enhanced Sensing and Spectroscopy*. *MRS Bulletin*, 2005. **30**(5): p. 368-375.

41. Sherry, L.J., et al., *Localized Surface Plasmon Resonance Spectroscopy of Single Silver Nanocubes*. Nano Letters, 2005. **5**(10): p. 2034-2038.
42. Link, S., M.B. Mohamed, and M.A. El-Sayed, *Simulation of the Optical Absorption Spectra of Gold Nanorods as a Function of Their Aspect Ratio and the Effect of the Medium Dielectric Constant*. The Journal of Physical Chemistry B, 1999. **103**(16): p. 3073-3077.
43. Maurer, T., P.-M. Adam, and G. L ev eque, *Coupling between plasmonic films and nanostructures: from basics to applications*. Nanophotonics, 2015. **4**(1).
44. Cesario, J., et al., *Electromagnetic coupling between a metal nanoparticle grating and a metallic surface*. Optics Letters, 2005. **30**(24): p. 3404-3406.
45. Jain, P.K., S. Eustis, and M.A. El-Sayed, *Plasmon Coupling in Nanorod Assemblies: Optical Absorption, Discrete Dipole Approximation Simulation, and Exciton-Coupling Model*. The Journal of Physical Chemistry B, 2006. **110**(37): p. 18243-18253.
46. Hentschel, M., et al., *Babinet to the Half: Coupling of Solid and Inverse Plasmonic Structures*. Nano Letters, 2013. **13**(9): p. 4428-4433.
47. Artar, A., A.A. Yanik, and H. Altug, *Multispectral Plasmon Induced Transparency in Coupled Meta-Atoms*. Nano Letters, 2011. **11**(4): p. 1685-1689.
48. Prodan, E., et al., *A Hybridization Model for the Plasmon Response of Complex Nanostructures*. Science, 2003. **302**: p. 419-422.
49. Paolo, B., H. Jer-Shing, and H. Bert, *Nanoantennas for visible and infrared radiation*. Reports on Progress in Physics, 2012. **75**(2): p. 024402.
50. Park, W., *Optical interactions in plasmonic nanostructures*. Nano Convergence, 2014. **1**(2): p. 1-27.
51. Miroshnichenko, A.E., S. Flach, and Y.S. Kivshar, *Fano resonances in nanoscale structures*. Reviews of Modern Physics, 2010. **82**(3): p. 2257-2298.
52. Yong, S.J., M.S. Arkady, and K. Chang Sub, *Classical analogy of Fano resonances*. Physica Scripta, 2006. **74**(2): p. 259.
53. Verellen, N., et al., *Fano Resonances in Individual Coherent Plasmonic Nanocavities*. Nano Letters, 2009. **9**(4): p. 1663-1667.
54. Luk'yanchuk, B., et al., *The Fano resonance in plasmonic nanostructures and metamaterials*. Nature materials, 2010. **9**(9): p. 707-715.
55. Harris, S.E., *Electromagnetically induced transparency*. Physics Today, 1997. **50**: p. 36-42.
56. Fleischhauer, M., A. Imamoglu, and J.P. Marangos, *Electromagnetically induced transparency: Optics in coherent media*. Reviews of Modern Physics, 2005. **77**(2): p. 633-673.
57. Zhang, S., et al., *Plasmon-Induced Transparency in Metamaterials*. Physical Review Letters, 2008. **101**(4): p. 047401.
58. Liu, N., et al., *Planar Metamaterial Analogue of Electromagnetically Induced Transparency for Plasmonic Sensing*. Nano Letters, 2010. **10**(4): p. 1103-1107.
59. Tassin, P., et al., *Electromagnetically Induced Transparency and Absorption in Metamaterials: The Radiating Two-Oscillator Model and Its Experimental Confirmation*. Physical Review Letters, 2012. **109**(18): p. 187401.

Chapter 3: Experimental

3.1 Introduction

This chapter provides a brief overview of the fabrication and experimental procedures employed throughout this thesis. This includes the fabrication of templated chiral substrates, and the experimental procedures and techniques for all spectroscopic measurements performed. Fabrication and characterisation of all samples were carried out in the James Watt Nanofabrication Centre, and the School of Engineering, at the University of Glasgow. With spectroscopic measurements for all experiments, and all protein purification being carried out in the School of Chemistry, at the University of Glasgow, unless otherwise stated.

3.2 Nanostructure Fabrication

3.2.1 Template Fabrication

To create the templated plasmonic substrates (TPSs), an initial metal nanopatterned template must be created. This template (known as a shim) can then be used to replicate the nanostructures many times, using the high-throughput injection moulding technique. To ensure that the same shim can be used for multiple batches of substrates, over an extended period of time, it has to be cleaned and stored between runs. This is done by washing the shim in ethanol and isopropyl alcohol (IPA) sequentially, and then cleaning it with oxygen plasma before and after each use. The shim is then stored in a clean room environment when not in use.

To fabricate the metal shim, the structures are first produced lithographically using electron beam lithography (EBL). Firstly, a silicon wafer is cleaned with several rounds of solvent washing (acetone, methanol, and IPA consecutively) and sonicated, and then dried under a constant stream of N₂ gas. A poly(methyl methacrylate) (PMMA, Lucite International, MW = 2010) resist layer is then spin coated onto the surface of the wafer to a thickness of 100 nm. The substrate is then left to bake in a 180°C oven for 5 minutes in order to evaporate any solvent. The nanopatterns are then written into the resist layer using an electron beam writer (Vistec VB6), and the substrate is developed using a 2.5:1 ratio of IPA and methyl isobutyl ketone (MIBK) for 60 seconds at 25°C. Once the resist has been developed, the substrate is electroplated with nickel (1mm), and acetone is then used to remove any remaining PMMA allowing the separation of the now nanopatterned nickel shim and the silicon

wafer. Nickel is used to fabricate the templated shim due to its low surface roughness, which limits the defects in the final injection moulded structures, and increases reproducibility [1].

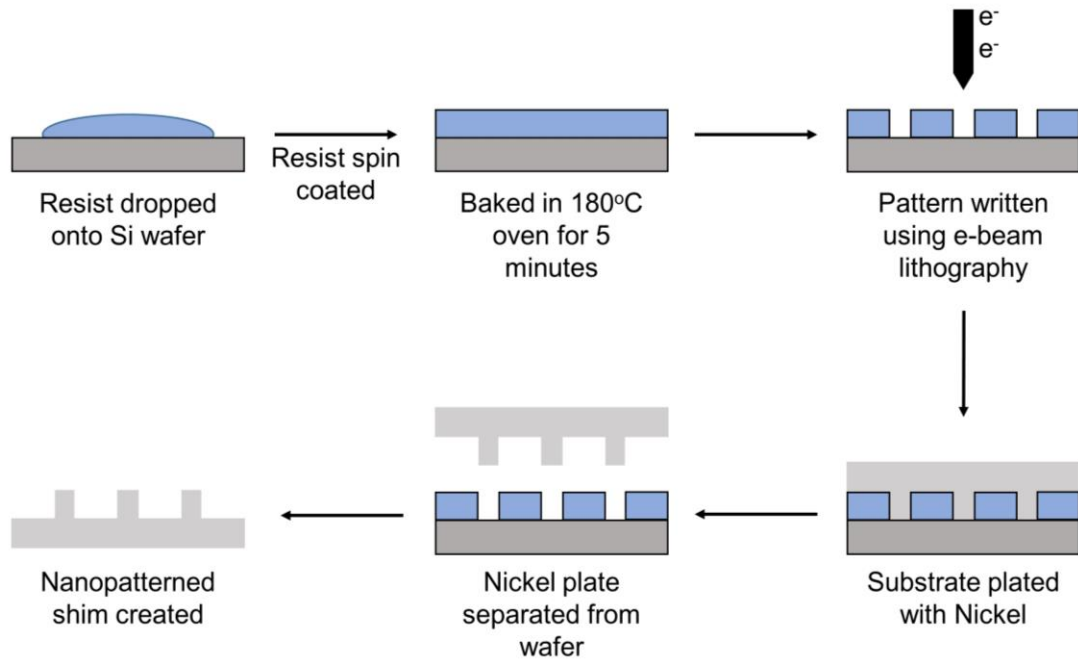


Figure 3.01 Graphical description of nickel shim fabrication for injection moulding process.

3.2.2 Injection Moulding

All samples were injection moulded using an Engel Victory 28 hydraulic injection moulder, shown in Figure 3.02(a), and made using clear polycarbonate (Makrolon OD 2015). The injection moulding process begins by fitting the nickel shim into the moulding tool and setting the appropriate parameters for flow and temperature of the polycarbonate. These parameters are vital to ensure that the polycarbonate flows completely over the templated shim, and ensures that all the features are replicated to a high quality. Stock polycarbonate beads, a few millimetres in diameter, are fed into the machine and heated to their melting point of 280°C, ready to be injected into the mould cavity. The process of creating the samples begins when the moving plate, containing the shim, moves towards the fixed plate and they lock together. The molten polymer is then injected under pressure into the cavity, at a constant rate, where the temperature is kept above the polymers glass transition temperature of 145°C. The molten polymer then rapidly cools upon contact with the nickel shim, reproducing the nanofeatures in a solid substrate surface.

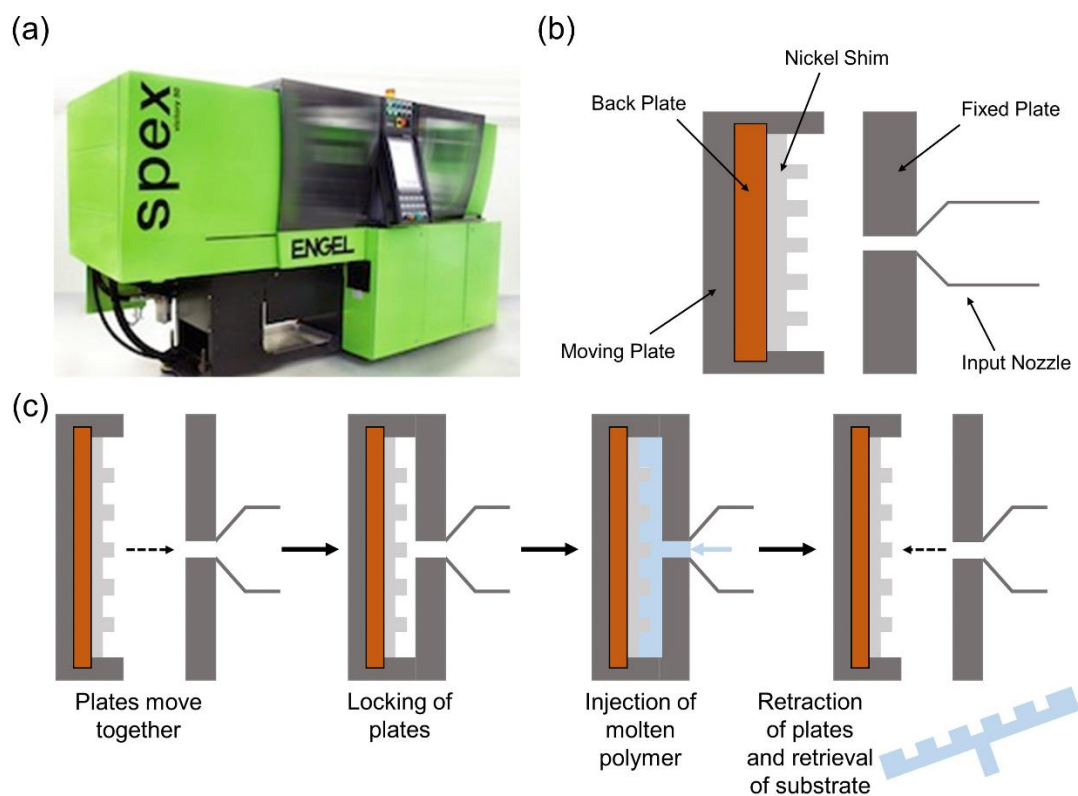


Figure 3.02 (a) Picture of Engel Victory 28 injection moulder, (b) graphical description of the injection moulder tool showing the nickel shim within the moulding cavity, and (c) graphical description of the high-throughput injection moulding process for creating each templated substrate.

The moving plate then retracts away from the fixed plate, allowing the solid polymer substrate to be retrieved from the tool. Once the sample is retrieved from the tool, the process (represented in Figure 3.02(c)) can be repeated as many times as necessary to create multiple replicates of the substrate. The whole process, from polymer injection to retrieval of the sample, is fully automated resulting in a high-throughput method of easily producing many identical substrates. A typical injection moulding session will produce upwards of 200 samples over approximately 2-3 hours, with one sample being produced every 20 seconds.

3.2.3 TPS Preparation

To complete the TPS process, each slide is rinsed with methanol and IPA consecutively, before being dried under a constant stream of nitrogen. The clean injection moulded slides (Figure 3.03 left) are then placed in an electron beam

evaporator (Plassys MEB-400s), where 100 ± 1.5 nm of gold is evaporated onto the substrate surface with a rate of ≈ 0.3 nm s⁻¹ under a chamber pressure of 1×10^{-7} mbar. This creates the final gold coated TPSs, Figure 3.03 right, which are cleaned before each experiment in an oxygen plasma cleaner (Gala Instruments, Plasma Prep 5) for 20 seconds at 160 W.

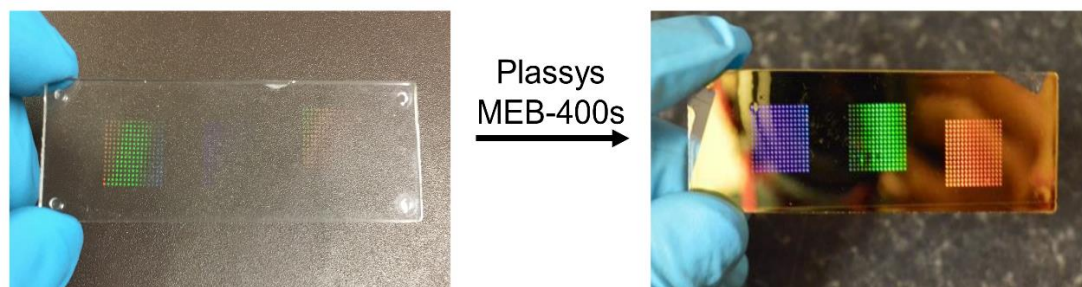


Figure 3.03 Photo of injection moulded substrates before, and after 100 nm gold is evaporated onto the nanopatterned surface.

3.2.4 Nanostructure Geometry

As a result of the injection moulding process, the nanopatterned surface of the polymer substrates consists of periodic arrays of chiral indentations, Figure 3.04(a). The chiral nanostructure indentations that are produced for use in this thesis are all six-fold symmetric “Shuriken” structures. These structures consist of a central circular section, with six equally sized and spaced arms extending out from the centre in both a curved left- and right-handed fashion (Figure 3.04 (c)). The size of these indentations (after being coated with 100 nm of gold) are 500 nm in diameter, between the widest two points of the shuriken structure, with a periodicity of 700 nm (SEM in section 3.3). The thickness of the arms for each structure is 32 nm wide, and the indentations have a depth into the polymer substrate of 80 nm. The dimensions of the arrays for both left- and right-handed shuriken structures are $300 \mu\text{m} \times 300 \mu\text{m}$, with each array consisting of 430 shurikens along each side, giving a total number of 184,470 shurikens per array. When the structures are coated with the 100 nm gold layer, the vertical side walls of the indentations are also completely covered. Resulting in a continuous gold film with periodic shuriken shaped indentations, containing a gold shuriken shaped structure at the base of these indentations (AFM data in section 3.3).

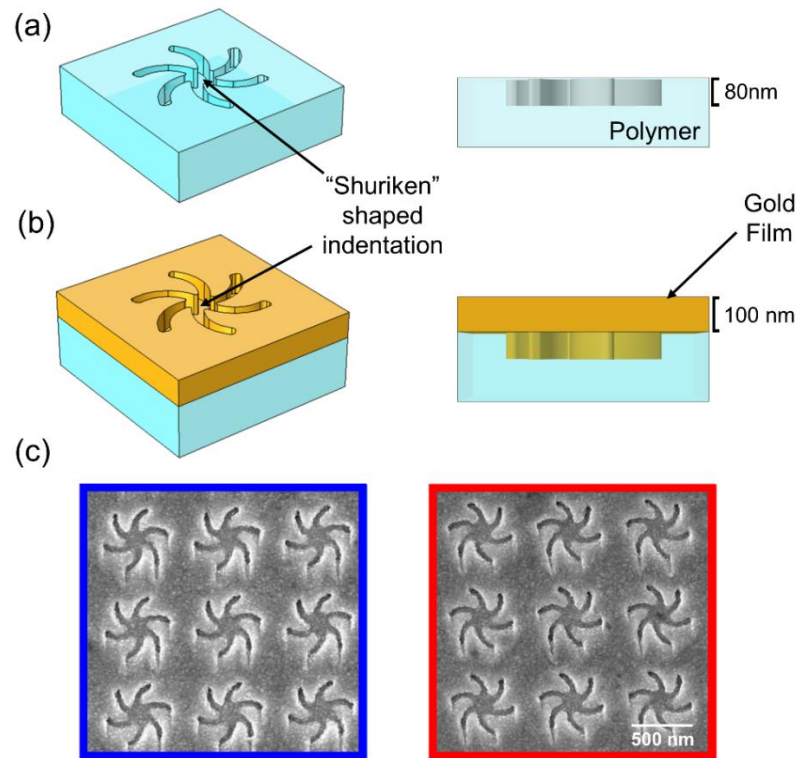


Figure 3.04 (a) Top and side view of shuriken indentation in injection moulded polymer substrate (80 nm depth), (b) shuriken indentations after evaporation with 100 nm gold, showing continuous gold film and indentations, and (c) SEM images of both right- (blue border) and left-handed (red border) shuriken structures with diameter of 500 nm and periodicity of 700 nm.

3.2.5 Nanostructure Hybridisation

Since the metamaterial structures consist of a solid shuriken shaped nanostructure, and an identical shaped void above it, they can be considered as ‘hybrid’ structures (or solid-inverse structures). With the roles of electric and magnetic fields being switched between the solid and inverse structures [2]. The result of this, is that symmetry equivalent electric and magnetic modes of the solid and inverse structures are located directly above each other, leading to effective coupling between the modes. To understand the coupling between the electric and magnetic modes of the hybrid structures in Figure 3.04, a hybridisation scheme (which is analogous to a molecular orbital diagram) can be created [3]. Since the solid and inverse structures consist of the same shape, positioned directly above each other, the electric and magnetic modes are symmetry identical, and belong to the C_6 point group. Hence, both modes belong to the A, B, E_1 , and E_2 symmetry species (C_6 character table in Appendix B). From the C_6 character table, it can be seen that modes with A and E_1

symmetry are optically bright since they have dipolar character, with only the E_1 mode being accessible with the normal incident geometry used. There are also two optically dark modes, B and E_2 , however the lowest energy dark mode with quadrupolar character is E_2 . Hence, the hybrid shuriken structures possess a bright dipolar mode with E_1 symmetry, and a dark quadrupolar mode with E_2 symmetry.

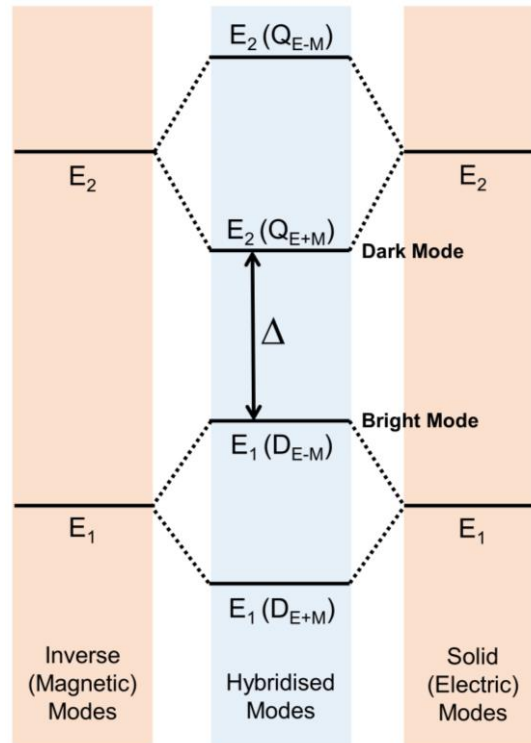


Figure 3.05 Hybridisation scheme between electric and magnetic modes of the shuriken nanostructures. Δ is the energy separation between the bright and dark modes.

Figure 3.05 shows the hybridisation scheme for the hybrid shuriken structures. The hybridisation of the two modes, can generate in-phase (bonding) and out-of-phase (antibonding) hybrid modes, with the bonding modes having lower energy, as described in chapter 2. The in-phase and out-of-phase combinations for the dipole hybrid modes are labelled D_{E+M} and D_{E-M} respectively, with the similar quadrupole modes labelled Q_{E+M} and Q_{E-M} . The energy separation between the bright and dark modes, Δ , dictates the coupling between D_{E-M} and Q_{E+M} . Hence, by controlling the coupling between the two modes, the optical properties of the structures can be controlled. With strong coupling within the hybrid structures, resulting in the interference effects described in Chapter 2, such as the plasmonic analogue of electromagnetically induced transparency [2].

3.3 Structure Characterisation Microscopy

3.3.1 Scanning Electron Microscopy (SEM)

Scanning electron microscopy (SEM) is a type of electron microscopy that uses a focused beam of electrons to scan the surface of a sample, and create a detailed image. This electron beam generally scans the surface of the sample in a raster scan pattern, and then combines the position and detected signal to create an image of the surface topography of the sample. Typically, the detected signal of the SEM system can be either secondary electrons (SE) or back-scattered electrons (BSE), with secondary electron detectors being the most common. These signals result from the focused electron beam interacting with atoms at various depths within the sample (depending on the substrate material and the voltage parameters of the SEM system), with the signal generated depending on the penetration depth. Very close to the surface, the beam of electrons interacts with the sample inelastically and results in ionisation of the sample. Secondary electrons (SE) are then emitted, which have an energy much lower than the primary electron beam, and can normally produce high-resolution images of sample surfaces with details of around 1 nm. In comparison, back-scattered electrons (BSE) are produced by elastic scattering from the sample and emerge from a larger depth from the surface. As these back-scattered electrons are generated from deeper locations within the sample, the resolution of the images are generally worse than images created from secondary electrons.

One important point to note for SEM images, especially when measured in secondary electron mode, is that non-conductive samples become charged when scanned with the primary electron beam, and this can cause scanning faults and artefacts on the SEM image. To prevent this accumulation of electrostatic charge, samples must be electrically conductive (at least on the surface), and so non-conductive materials are typically coated with a conductive material such as gold or platinum.

The structures used throughout this thesis were initially characterised using two different SEM microscopes; an FEI Nova NanoSEM 630, and a Hitachi S4700 SEM. All images were recorded through the secondary electron method described above. The resolution limit of the FEI Nova NanoSEM 630 is ~5 nm at 10 keV, and the Hitachi S4700 SEM has a resolution limit of ~10 nm at 10 keV. The Hitachi S4700 SEM microscope, with the lower resolution limit, was initially used to quickly monitor the quality of the fabrication process throughout, with the FEI Nova NanoSEM 630 used to obtain high quality images for the characterisation of the final substrates.

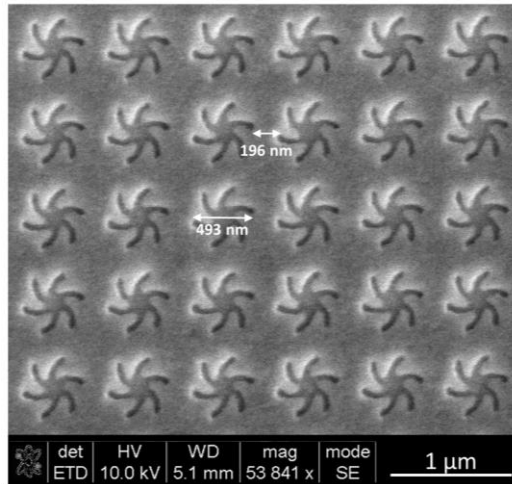


Figure 3.06 SEM image of right handed shuriken structures recorded using the FEI Nova NanoSEM 630, after the evaporation of 100 nm gold onto the nanostructured surface.

3.3.2 Atomic Force Microscopy (AFM)

Atomic force microscopy is a type of scanning probe microscopy that uses a mechanical probe to gather information from a samples surface, and has a resolution on the order of sub-nanometres.

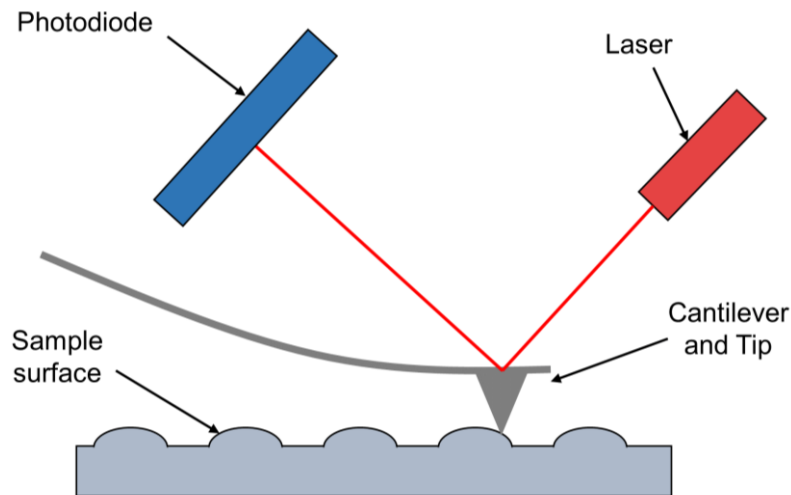


Figure 3.07 Graphical description of atomic force microscopy (AFM) system.

The atomic force microscope consists of a cantilever with a sharp tip at its end, known as the probe, which typically has a radius at its end on the order of a few nanometres to tens of nanometres. There are two main modes in which the microscope can be operated; either in static mode, where the tip is in contact with the sample surface, or

dynamic mode, where the cantilever is oscillated at a given frequency along the sample surface. In static or contact mode, the AFM tip is essentially dragged along the surface of the sample measuring the contours of the surface directly. Whereas, in dynamic or tapping mode, the tip is brought into close proximity of the sample surface, and oscillates at its resonant frequency. As the tip is in close proximity to the surface, this allows short range forces to act upon the tip, such as Van der Waals forces, dipole-dipole interactions, and electrostatic forces, causing the frequency of the cantilevers oscillation to change. This amplitude change alerts the system to alter the height of the cantilever till the initial oscillation amplitude is restored. This is continually adjusted as the tip scans the sample surface, and the height change modulates the reflection of the laser off the top of the cantilever. This change in reflection is then detected by the photodiode (Figure 3.07), and allows an accurate topological image of a surface to be achieved. The thickness of the AFM tip often dictates the resolution achieved by the system, as a thinner tip will be more accurate and will be able to decipher the smaller features of the sample surface with more accuracy.

The AFM data collected when characterising the nanostructure substrates used throughout this thesis were collected using a Bruker Dimension Icon Atomic Force Microscope. The data were collected in tapping mode, with the vertical noise of the system being < 30 pm.

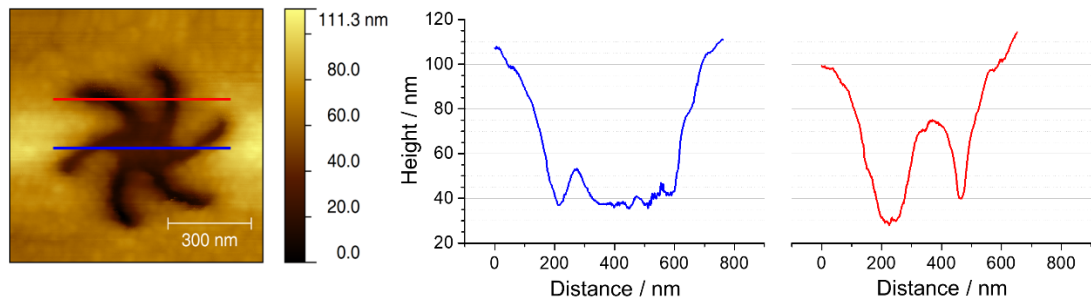


Figure 3.08 AFM image, and height profiles, for shuriken structures covered with 100 nm gold. Red and blue lines overlaying the AFM image correspond to the regions where the similarly coloured height profiles were measured.

The AFM images and height profiles, Figure 3.08, show that the depth of the shuriken structures after deposition of 100 nm gold is ~70 – 80 nm. It can also be observed that the height profile does not sharply drop off to a minimum, but gradually decreases over a small distance. This shows that the vertical walls of the indentations slope

gradually to the base of the structure, resulting in a continuous gold film, as the side walls are completely coated with gold.

3.4 Spectroscopy

3.4.1 Polarisation Microscope

All linear spectroscopic measurements throughout this thesis were recorded using a custom built polarisation microscope, as shown in Figures 3.09 and 3.10. A 50W tungsten halogen lamp (Thorlabs) serves as an unpolarised broadband light source, with the light passing through a collimating lens, and then a Glan-Thompson calcite polariser (Thorlabs), to generate a vertically polarised beam of light. This polarised beam of light then passes through a 50:50 beamsplitter, with the diverted beam passing through a 10x objective lens with 0.3 numerical aperture (Olympus UPlanFLN 10x). The light is then reflected from the sample and passes back through the beamsplitter, and then through a further Glan-Thompson polariser (Thorlabs) before passing through a second 50:50 beamsplitter. One output from the second beamsplitter is sent to a camera (Thorlabs CMOS Camera, DCC1645C), to image the surface and assist in aligning the microscope, with the second output being collected by the spectrometer (Ocean Optics USB4000).

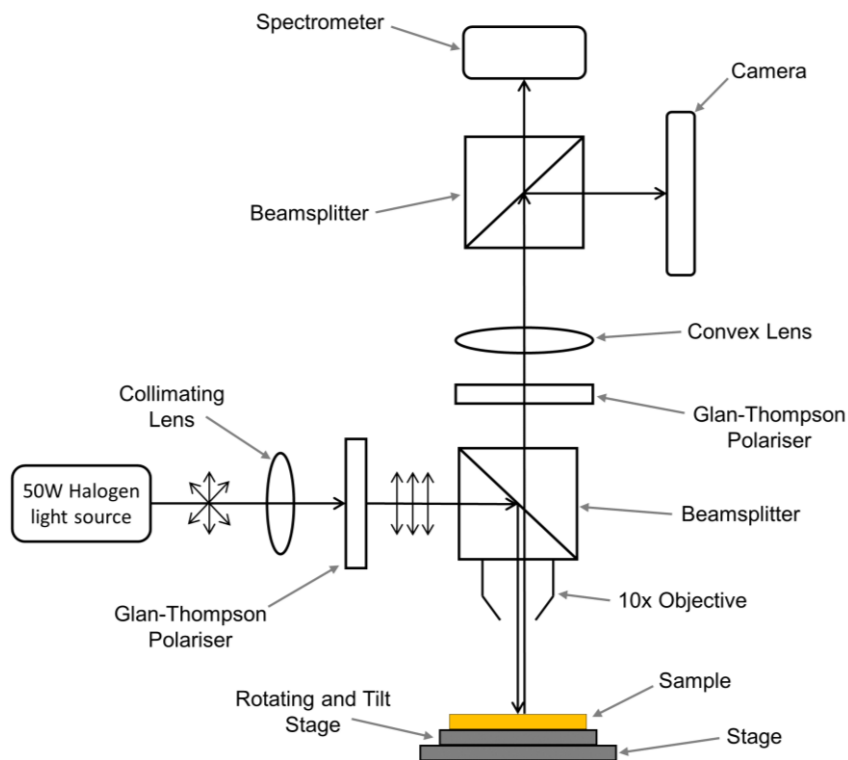


Figure 3.09 Schematic representation of the custom built polarisation microscope.

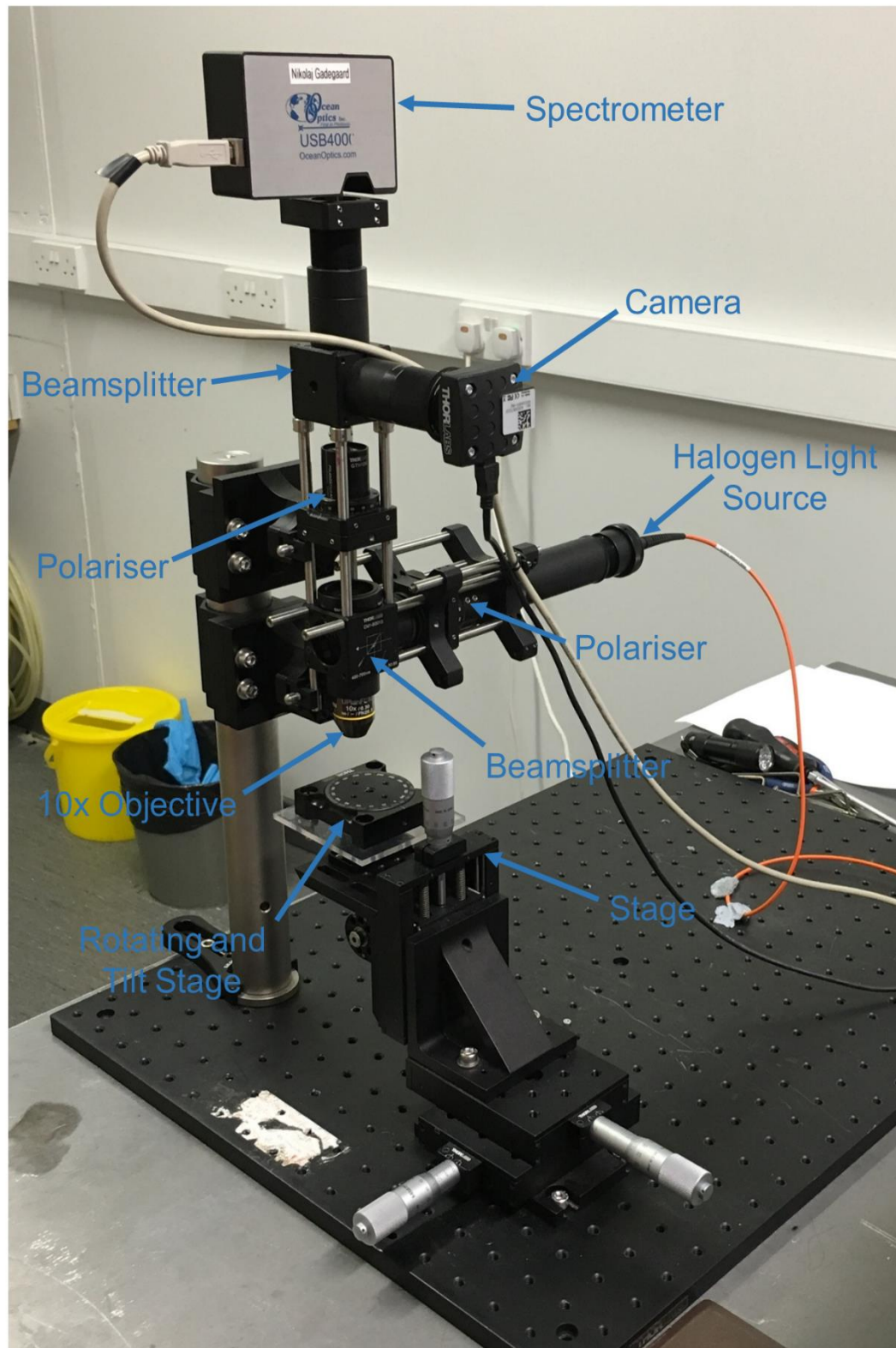


Figure 3.10 Photograph detailing the custom built polarisation microscope.

The Thorlabs camera (DCC1645C) is used to assist in the positioning and focus of the nanostructure array. The camera is positioned after the second beamsplitter and gives a clear image of the reflected beam off the surface, with an approximate field of view of 350 x 350 μm , Figure 3.11.

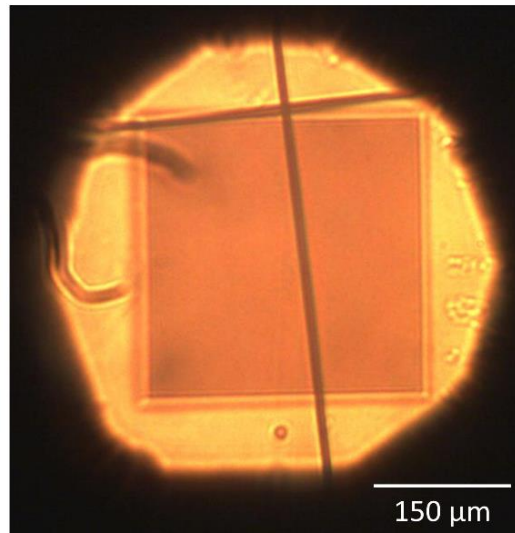


Figure 3.11 Picture from Thorlabs DCC1645C camera showing field of view for custom built polarisation microscope.

The image in the camera allows the sample to be consistently positioned in the same place for each measurement. The sample position can then be fine-tuned by adjusting the rotation and tilt stage, so that the reflected beam is normal to the sample surface.

3.4.2 Optical Rotatory Dispersion Spectroscopy

Optical rotatory dispersion (ORD) spectra can be measured for both the left- and right-handed plasmonic structures. Using Stokes parameters, the ORD spectra can be calculated by measuring the light intensity at four different polarisation angles relative to the incident polarisation. The measurements are recorded at 0° , 45° , 90° and 135° (equivalent to -45°), and the ORD calculated as:

$$ORD = \frac{1}{2} \tan^{-1} \frac{(I_{45} - I_{135})}{(I_0 - I_{90})} \quad (3.4.1)$$

To reduce background noise, measurements are collected from both left-handed and right-handed structures, as well as the flat gold surface, and repeated for four sets of measurements. The ORD measured from the flat gold background is then subtracted

from the left- and right-handed nanostructure spectra. For each handedness of the chiral nanostructures, left- and right-handed shurikens, the ORD spectra will be equal and opposite, resulting in a bisignate shape shown in Figure 3.12. The ORD spectra arises due to a plasmonic excitation, with the wavelength of these plasmonic resonances depending on the refractive index of the surrounding medium. So, when the refractive index above the chiral nanostructures increases, the wavelength position of the plasmonic resonance would experience a red shift.

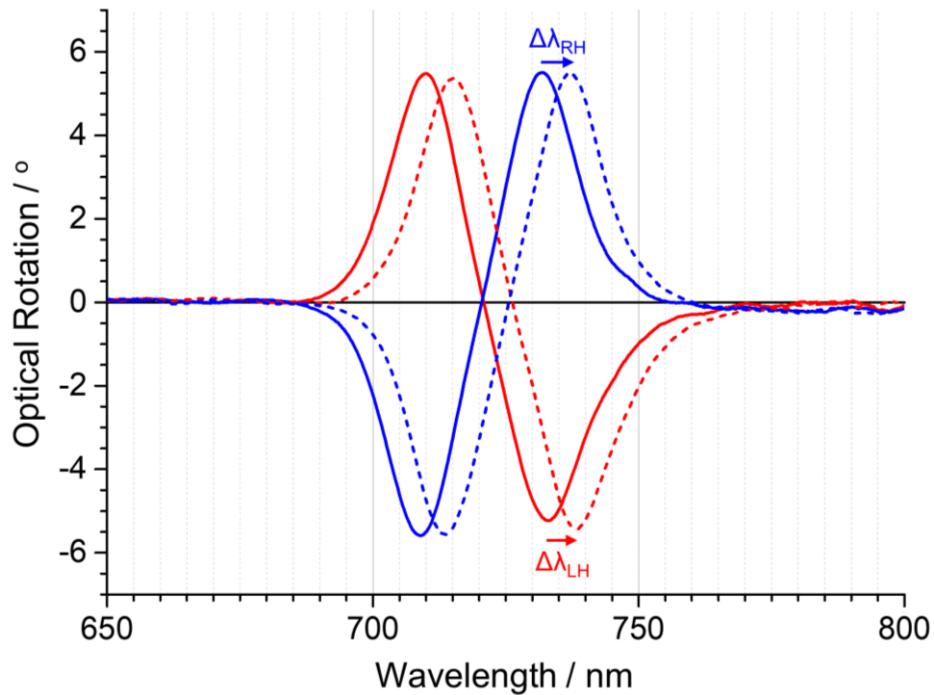


Figure 3.12 Example ORD spectra measured from left- (red) and right-handed (blue) nanostructures with water (solid) and a higher refractive index solution (dashed) on the substrate surface.

To characterise the asymmetry in the wavelength position, between left- and right-handed nanostructures, ORD spectra for both handedness of nanostructures are recorded for water/buffer as a reference. The higher refractive index solution, or protein solution, is then adsorbed onto the substrate surface, and the ORD spectra measured the same way as before. Each measurement, buffer and analyte, are repeated four times and averaged to further reduce the noise and error in the system. The peak positions of these ORD spectra are then measured, and the change in wavelength is calculated for both left- and right-handed structures as follows:

$$\Delta\lambda_{RH/LH} = \lambda_{(Analyte)} - \lambda_{(Buffer)} \quad (3.4.2)$$

This gives the $\Delta\lambda_{RH/LH}$ wavelength shift parameter for both the left- and right-handed nanostructures, as shown in Figure 3.12. An asymmetry parameter, $\Delta\Delta\lambda$, can then be defined from the wavelength shift of each handedness of nanostructure, $\Delta\lambda_{RH}$ and $\Delta\lambda_{LH}$, and can be measured as:

$$\Delta\Delta\lambda = \Delta\lambda_{RH} - \Delta\lambda_{LH} \quad (3.4.3)$$

For achiral media, such as salt solutions, the solution is completely isotropic, and would have the same contribution to both left- and right-handed chiral fields. This results in the wavelength shift of the resonance for left- and right-handed nanostructures being equal, giving a zero $\Delta\Delta\lambda$ value. Contrary to achiral solutions, when a solution containing chiral molecules (such as protein solutions) is placed above the substrate surface, the wavelength of the plasmonic resonance shifts asymmetrically for the left- and right-handed nanostructures. Resulting in a measurable change of the $\Delta\Delta\lambda$ value. This occurs as the adsorbed species are no longer isotropic, and therefore would interact asymmetrically with the chiral fields of opposing handedness.

The asymmetry parameter, $\Delta\Delta\lambda$, will be used in chapter 4 to quantify higher order structural changes in two well characterised proteins, which undergo ligand induced conformational changes.

3.4.3 Reflectance Spectroscopy

In addition to the optical rotatory dispersion spectra, reflectance spectra can also be obtained from the chiral gold nanostructures. However, instead of measuring the light intensity with the output polariser at 4 different angles, all of the reflectance measurements are measured with the analyser at 0°. The reflected light intensity is measured from the nanostructures, both left- and right-handed, and then measurements are taken from the flat gold. These measurements are taken with buffer, as reference, and then with the desired solution on the surface of the substrate. All these measurements are repeated 8 times, and then averaged to reduce the noise and error within the system. Reflectance spectra can then be calculated as:

$$Relative\ Reflectance = \left(\frac{I_{Nanostructure}}{I_{Background\ Gold}} \right) \quad (3.4.4)$$

Contrary to the opposite ORD spectra we see from the chiral nanostructures, the reflectance spectra generated by both left- and right-handed shurikens show a near identical shape to each other, Figure 3.13.

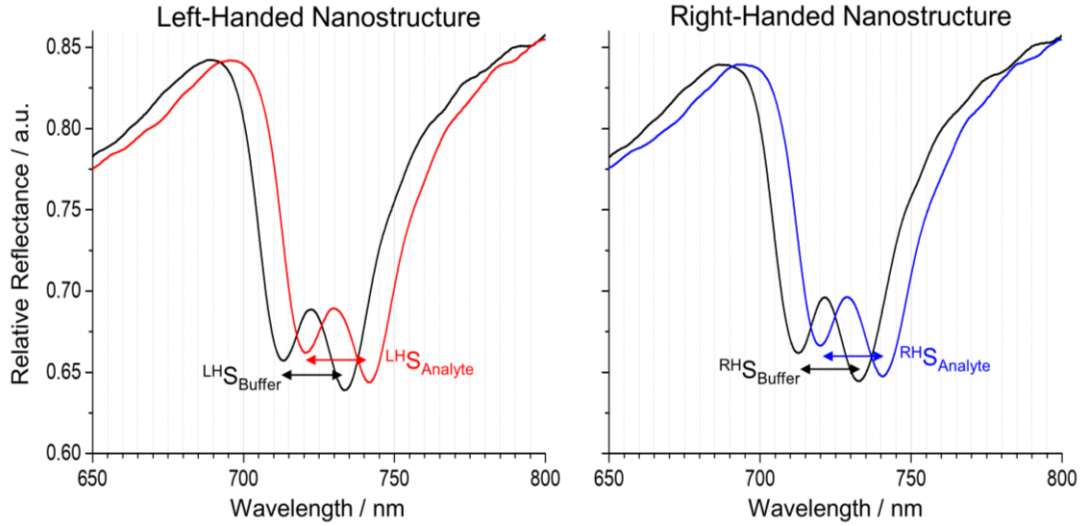


Figure 3.13 Example reflectance spectra for both left- and right-handed shuriken structures with water (black), and a higher refractive index solution (coloured) on the substrate surface.

The main resonance in the reflectance spectra, shown in Figure 3.13, shows a peak of reflectivity occurring within a significant reflectance dip. This occurs, as described in Chapter 2, as a result of the plasmonic analogue of electromagnetically induced transparency. Where strong coupling occurs between the optically bright dipolar and the optically dark quadrupolar modes of the nanostructures [4].

From the reflectance spectra, a new asymmetry parameter can be introduced. Instead of measuring the wavelength shift of the resonance, which was measured for the ORD results, the separation between the two reflectance dips can be measured for differing solutions (Figure 3.13). This value is quantified in a similar fashion to $\Delta\Delta\lambda$, where the $\Delta S_{RH/LH}$ value must first be calculated using:

$$\Delta S_{RH/LH} = {}^{RH/LH}S_{(Analyte)} - {}^{RH/LH}S_{(Buffer)} \quad (3.4.5)$$

This $\Delta S_{RH/LH}$ value, can be measured for both the left- and right-handed nanostructures, as shown in Figure 3.13, to give a ΔS value for each handedness. Therefore, to obtain the final asymmetry parameter for the reflectance data, the $\Delta\Delta S$ value can be calculated using:

$$\Delta\Delta S = \Delta S_{RH} - \Delta S_{LH} \quad (3.4.6)$$

The separation asymmetry parameter, $\Delta\Delta S$, can be used to characterise and identify changes that are seen in the reflectance spectra due to changes in the solutions or proteins adsorbed to the substrate surface. In agreement with the ORD measurements, there should be no separation asymmetry in the reflectance spectra when achiral solutions of a higher refractive index are added to the substrate. However, when a solution of chiral molecules, or protein solution, is adsorbed on the substrate surface, the effect on the left- and right-handed spectra will be unequal, creating an asymmetrical change, which can be measured by the $\Delta\Delta S$ parameter.

This change in the $\Delta\Delta S$ parameter will be used in chapters 5, 6 and 7 to quantify protein conformational changes, variations in surface immobilised orientation, and concentration differences of Immunoglobulin G within spiked human blood serum solutions.

3.4.4 Electromagnetic Modelling

To determine the spatial distribution, and level of chiral asymmetries, in the fields generated by the shuriken nanostructures, electromagnetic (EM) simulations for linearly polarised light with wavelength in the resonance region of 700 nm were performed using COMSOL Multiphysics software. The chiral asymmetries of the evanescent fields generated by the chiral shuriken structures was characterised using the optical chirality parameter first proposed by Tang and Cohen [5], and is described in chapter 2.

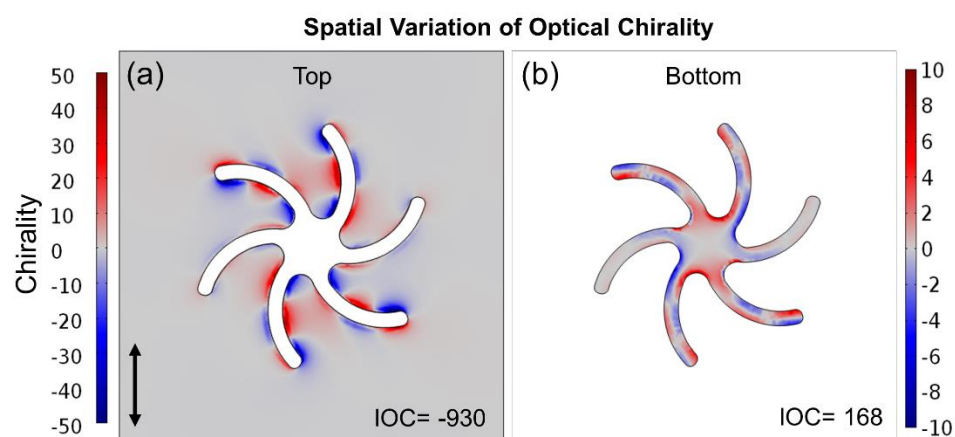


Figure 3.14 EM simulation of chiral field plots for (a) top surface, and (b) bottom surface of the shuriken structure. The black arrow represents the direction of incident polarisation.

From the results shown in Figure 3.14, when the structure was excited with linearly polarised light, chiral evanescent fields of both left- and right-handed chiral asymmetries are generated, with one handedness generated in excess. The chiral fields are largest at the top surface of the nanostructure, with the bottom surface showing chirality values almost an order of magnitude smaller. From Figure 3.14(a) and (b), it looks as though the magnitude of the chiral fields produced with opposite handedness (blue and red) would cancel each other out at the surface. However, when the chirality values are integrated over the respective surface, an integrated optical chirality value is achieved. With these values being -930 and 168, for the top and bottom surfaces respectively, indicating that there is a large chiral asymmetry value overall. This reinforces the fact that the shuriken shaped nanostructures generate evanescent fields with enhanced chiral asymmetries relative to circularly polarised light, with the overall asymmetry being governed by the handedness of the structure [6, 7].

3.4.5 Refractive Index Measurements

To initially characterise the sensitivity of the chiral shuriken nanostructures, calibration measurements using solutions of achiral media of increasing refractive index were performed. Solutions of NaCl of differing concentrations, as well as ethanol, were used to give different refractive index solutions, without changing the chirality on the surface of the substrate. The calibration solutions consisted of water, 1 M NaCl solution, 2.2 M NaCl solution, ethanol, and 4.4 M NaCl solution, with the measured refractive index of each solution being 1.334, 1.343, 1.353, 1.361, and 1.370 respectively. ORD measurements were recorded in the presence of each solution on the nanostructure surface, starting with water and increasing the refractive index to the final solution of 4.4 M NaCl solution. Figure 3.15 shows the ORD spectra for both left- and right-handed structures for all refractive index salt solutions, and graphs showing the peak positions for each solution, and asymmetry parameter between each solution and water. In Figure 3.15(c), blue and red lines are also included to show the asymmetry parameter values produced from two exemplar proteins, that will be studied in chapter 4, relative to the salt solution values. The reflectance measurements were characterised in the same way as the ORD spectra, described above. Calibration solutions consisting of water and salt solutions were produced with refractive indices of 1.333, 1.337, 1.340, and 1.344. With the reflectance spectra for each refractive index being shown in Figure 3.16(a).

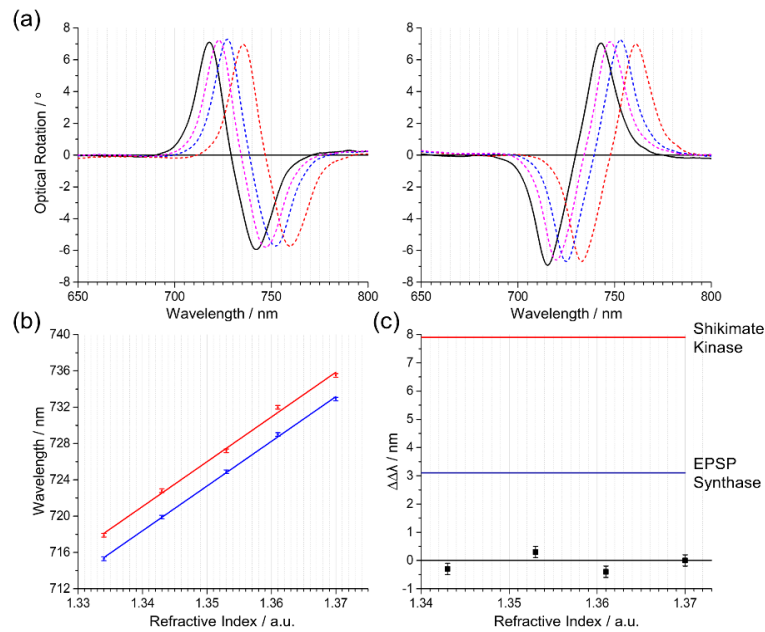


Figure 3.15 (a) ORD spectra for left- and right-handed nanostructures in the presence of achiral salt solutions of increasing refractive index, (b) peak positions for left- (red) and right-handed (blue) shuriken structures with increasing refractive index solutions, and (c) asymmetry values relative to water for increasing refractive index, with comparison of asymmetry values for two exemplar proteins, EPSP Synthase and SK (Chapter 4). The error bars represent the standard error calculated from 8 spectra measurements.

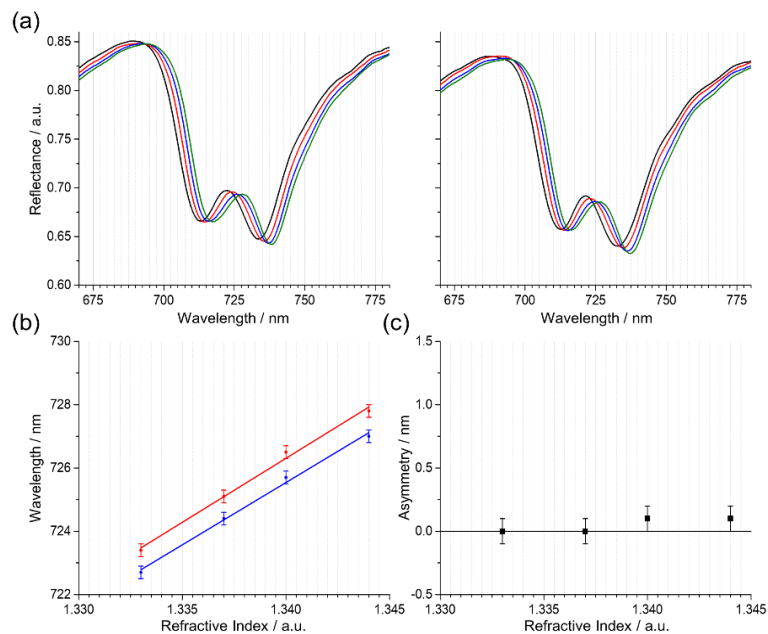


Figure 3.16 (a) Reflectance spectra for left- and right-handed nanostructures in the presence of achiral salt solutions of increasing refractive index, (b) average positions for left- (red) and right-handed (blue) shuriken structures with increasing refractive index solutions, and (c) asymmetry values relative to water for increasing refractive index. The error bars represent the standard error calculated from 8 spectra measurements.

From Figures 3.15(a) and 3.16(a), it can be seen that by adding the achiral salt solutions of increasing refractive index, the plasmonic resonance in the ORD spectra and the positions of the reflectance spectra experience a red shift in their wavelength. When we look at the wavelength shifts for the left- and right-handed shuriken structures, for both ORD and reflectance, the shift is linear for both structures with the magnitude of the shift being equal between left- and right-handed structures, shown in Figures 3.15(b) and 3.16(b). As expected for achiral media, like salt solutions, there is no asymmetry difference within experimental error for the increasing refractive index relative to the initial water measurements. These results are shown for the ORD and reflectance measurements in Figures 3.15(c) and 3.16(c) respectively. This is due to the right- and left-handed chiral fields interacting equally with the achiral media, and hence producing no net chiral asymmetry, as described previously.

3.5 Surface Functionalisation and Preparation

3.5.1 Nitrilotriacetic Acid (NTA) Functionalisation

To functionalise the gold substrate surface, a thiolated nitrilotriacetic acid (NTA) monolayer was co-adsorbed with triethylene glycol mono-11-mercaptoundecyl (EG-thiol), using a process previously described in the literature by Sigal et al. [8]. Firstly, the gold substrates are cleaned in an oxygen plasma cleaner for 20 seconds at 160W before being immersed in a 95% ethanol solution and bubbled with nitrogen. A further solution, in 95% ethanol, is made containing 0.1 mM NTA (Prochimia Surfaces) and 0.9 mM EG-thiol (Sigma Aldrich) giving a total thiol concentration of 1 mM. The clean gold substrates are then placed into the thiol solution and bubbled with nitrogen gas for a further 5 minutes. After bubbling with nitrogen, the substrates are left in the thiol solution to incubate overnight (16-20 hours), which allows for the formation of a self-assembled monolayer (SAM) on the substrate surface. The samples are removed from the thiol solution before being rinsed with 95% ethanol, and then incubated in 1 mM sodium hydroxide for 5 minutes. They are then rinsed with water, and left to incubate for 1 hour in a 40 mM nickel (II) sulphate solution. Finally, the samples are removed and rinsed with ~1 ml HBS (HEPES buffered saline, 10 mM HEPES and 150 mM NaCl in water at pH 7.2), and then ~5 ml of water before being dried under a stream of nitrogen.

When the nickel (II) sulphate solution is added to the self-assembled monolayer, the Ni^{2+} adsorbs to the surface NTA groups to create an NTA/ Ni^{2+} complex.

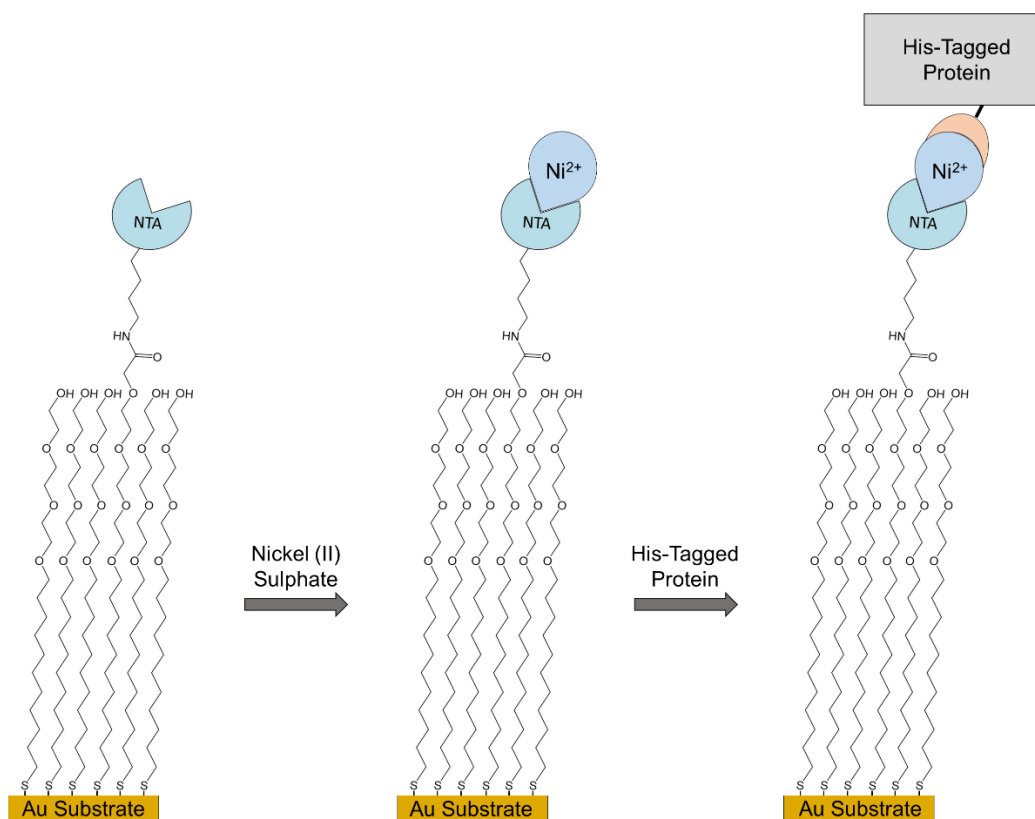


Figure 3.17 Scheme showing NTA monolayer functionalisation, binding of Ni²⁺, and final binding of His-tagged protein to the NTA/Ni²⁺ complex.

The NTA/Ni²⁺ chelate formed on the surface, has a high affinity for specifically binding His-tagged proteins, through the binding of the two vacant sites on the Ni²⁺ ions and the histidine group attached to the protein. This allows the proteins to be attached to the surface of the gold substrate with a consistent and uniform orientation over the whole area. Binding proteins to the gold surface using this method has previously been shown to have very little effect on the bound proteins ability to interact with other proteins or ligands in solution [9, 10].

In chapters 4 and 6, the gold substrates were functionalised, as described above, with a mixed monolayer of NTA and EG-thiol. However, in chapter 7, the gold substrates were functionalised with a monolayer consisting of NTA only, and no nickel (II) sulphate solution was added. This resulted in a completely charged monolayer, consisting of NTA, and possessing a negative charge across the whole surface, suitable for preferentially binding the net positively charged immunoglobulin G protein.

3.5.2 Protein Preparation

The preparation of the His-tagged proteins were all done, by the Laphorn lab at the university of Glasgow, following the same method described here, unless otherwise stated.

Existing genes of the protein, cloned into a pET 22b vector are transformed and over expressed in BL21 star cells. Liquid Luria Broth (1 litre) is used to grow the cells, and protein expression is induced with isopropyl β -D-1-thiogalactopyranoside (IPTG) at an optical density of 0.6 at 600 nm. The cells are harvested 3 hours after induction by centrifugation and re-suspended in 50 mM Tris/HCl buffer at pH 7.8, before being lysed using sonication and centrifuged at 2000 rpm to remove all insoluble matter. The protein is then purified from the cell lysate by NTA nickel chromatography, with the protein being eluded using 300 mM imidazole, 300 mM NaCl in 100 mM Tris/HCl buffer at pH 7.8. Next, the protein is concentrated by centrifugal concentration and buffer exchanged by dialysis in 50 mM Tris/HCl buffer pH 7.5. The purity of the protein is then assessed by SDS-Page gel electrophoresis and the enzyme activity checked using a phosphate release assay.

3.5.3 Microfluidic Chamber

To perform the spectroscopic measurements on the gold substrates, in the presence of buffer or other solutions, the substrate needs to be inserted into a custom made microfluidic cell. This microfluidic cell was custom designed and 3D printed to produce a chamber that had the perfect size to accommodate the TPS, and allow a chamber with an approximate volume of 300 μ l.

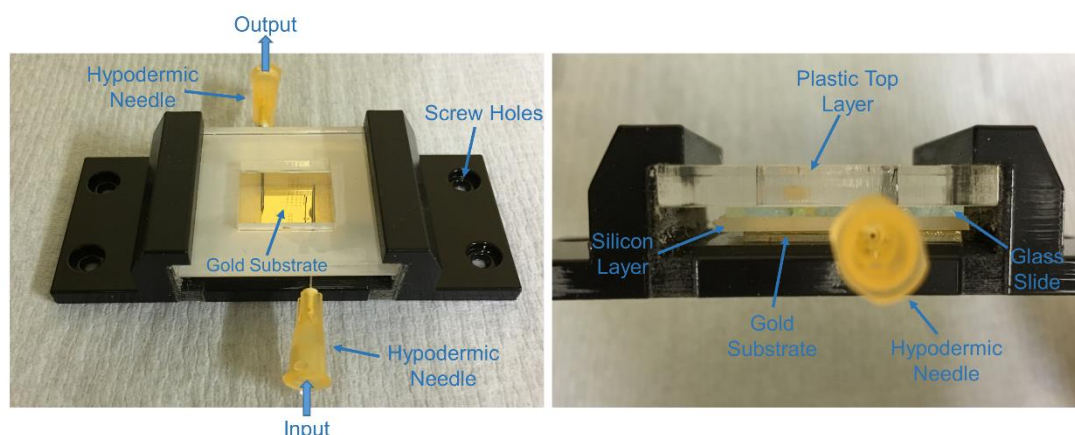


Figure 3.18 Labelled photo, showing top and side view, of custom made 3D printed microfluidic chamber for TPSs.

The watertight microfluidic chamber is made by placing the clean TPS at the base of the 3D printed structure, then a silicon layer with a hole cut in the middle is added to expose the chiral nanostructures on the TPS. A clean glass microscope slide is placed on top of this, and the plastic top layer inserted to apply pressure to the system, and create the watertight seal between the glass slide and TPS using the silicon layer. Two hypodermic needles are inserted at opposing sides, that allow for insertion and extraction of any solutions added, to complete the assembly of the microfluidic chamber.

3.6 Modelling

3.6.1 Mathematical Model for EIT

The basis of the model used to fit plasmonic induced transparency spectra within this thesis was first proposed by Zhang et al. [4], and subsequently used by Tassin et al. [11]. This classical model, used to describe plasmonic induced transparency, is based on two coupled oscillators, and is described in chapter 2. To generate the fitting spectra, and change the data to accurately fit the experimental results, a script was created in MATLAB (Mathworks R2016b) to implement the coupled oscillator equations. To accurately fit the data, ten parameters were initially changed to achieve the best fit possible for all water/buffer reference measurements. The ten parameters and their definitions are shown in Table 3.01.

Parameter	Definition
ω_r	Radiative mode resonance frequency
ω_d	Dark mode resonance frequency
k	Coupling coefficient
γ_r	Radiative mode damping
γ_d	Dark mode damping
θ	Radiative mode phase
ϕ	Dark mode phase
g	Incident light coupling coefficient
n_e	Refractive index of solution
c_{Au}	Multiplier for Au contribution to susceptibility

Table 3.01 Descriptions of the parameters that are used to implement the mathematical model for plasmonic induced transparency.

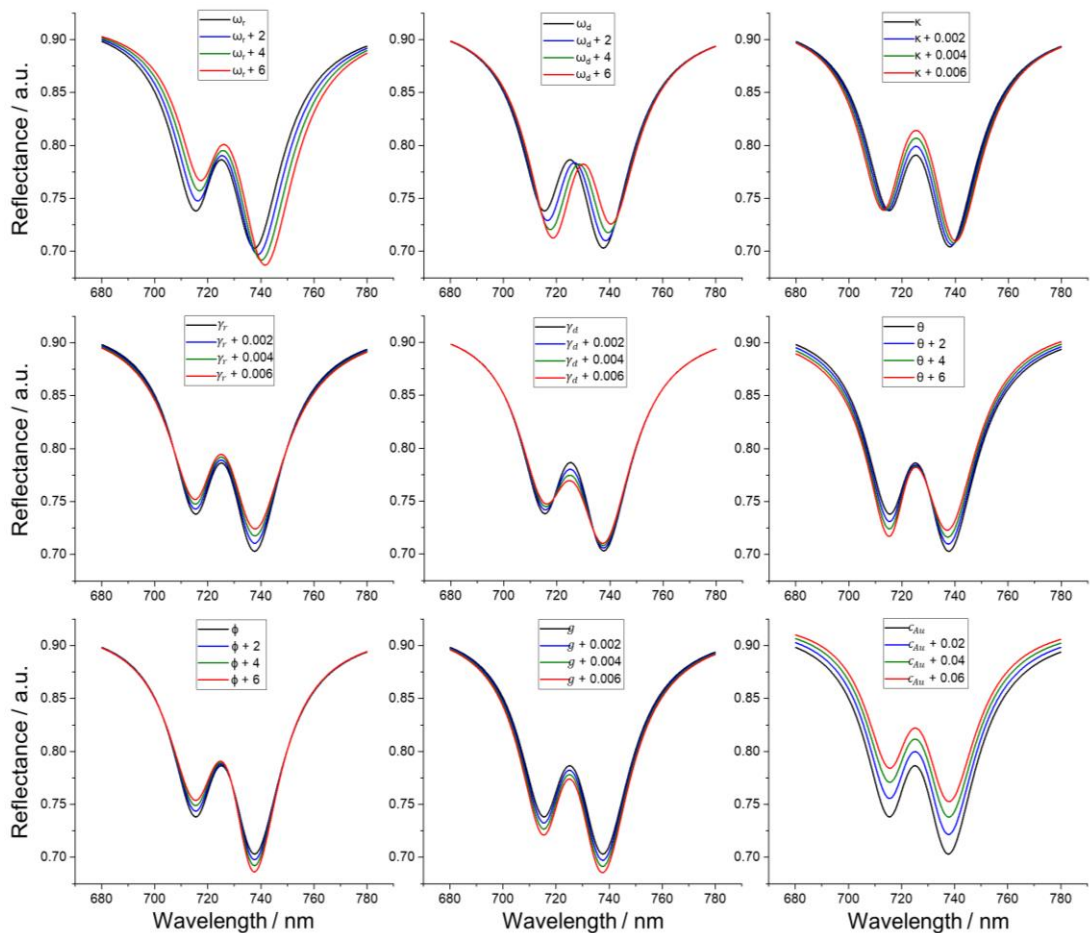


Figure 3.19 Effect of varying each parameter in the model by small increments from the initial values.

Figure 3.19 shows the results of varying each parameter by a small amount, relative to the initial values for each parameter, and how these small changes affect the size and shape of the reflectance spectra formed. By varying all these parameters, we can tune the fitting spectra for the buffer to be relatively similar. However, when fitting the protein or solution data, added after taking the water/buffer measurements, only five of the parameters are changed from the initial water/buffer fit; ω_r , ω_d , κ , θ , and ϕ . From these five parameters, ω_r and ω_d shift the bright and dark modes respectively, κ controls the coupling strength and affects the separation between the two reflectance dips, and θ and ϕ vary the heights of the reflectance dips as shown in Figure 3.19, with θ also slightly tilting the whole spectra.

3.6.2 Salt Solution Modelling

To test the model sensitivity and accuracy at modelling the experimental reflectance data, the salt solutions shown in Figure 3.16 were modelled. All ten parameters were initially allowed to vary to fit the water data, with the five listed parameters varying to fit the subsequent salt solution spectra. The values for each parameter used to fit the salt solution data are shown in Table 3.02, with the values of each of the five variable parameters plotted against refractive index in Figure 3.20.

Parameter	Left-handed				Parameter	Right-handed			
	Water 1.333	Salt 1 1.337	Salt 2 1.34	Salt 3 1.344		Water 1.333	Salt 1 1.337	Salt 2 1.34	Salt 3 1.344
ω_r	724.8	726.5	727.9	729.2	ω_r	725.0	726.7	728.1	729.3
ω_d	722.0	723.7	725.1	726.4	ω_d	720.7	722.4	723.8	725.0
k	0.0298	0.0299	0.0297	0.0299	k	0.0286	0.0287	0.0286	0.0286
γ_r	0.031	0.031	0.031	0.031	γ_r	0.032	0.032	0.032	0.032
γ_d	0.0278	0.0278	0.0278	0.0278	γ_d	0.0260	0.0260	0.0260	0.0260
θ	-20.5	-20.6	-20.6	-20.4	θ	-19.5	-19.6	-19.5	-19.6
ϕ	-21.8	-21.7	-21.9	-21.8	ϕ	-23.0	-23.2	-23.1	-22.9
g	0.0176	0.0176	0.0176	0.0176	g	0.0162	0.0162	0.0162	0.0162
n_e	1.33	1.33	1.33	1.33	n_e	1.33	1.33	1.33	1.33
c_{Au}	0.1445	0.1445	0.1445	0.1445	c_{Au}	0.1380	0.1380	0.1380	0.1380

Table 3.02 Parameter values used to fit the experimental salt solution spectra for left- and right-handed shuriken structures.

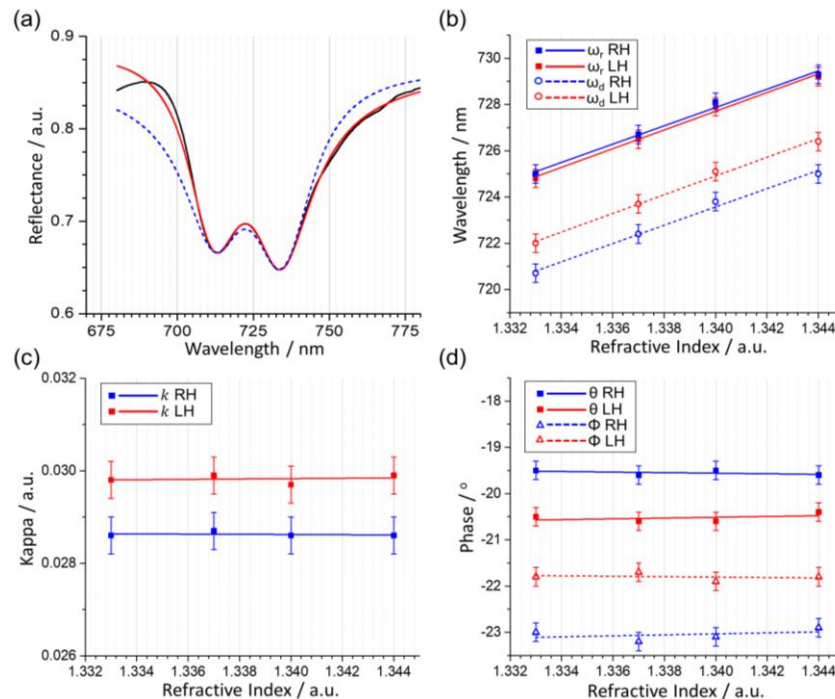


Figure 3.20 (a) Experimental reflectance spectra (black) and fitting of data without the consideration of phase (blue dashed), and with the introduction of phase (red), and (b-d) fitting results for ω_r , ω_d , k , θ , and ϕ compared to the refractive index of solutions. The error bars represent the standard error calculated from 8 spectra measurements.

Figure 3.20(a) shows optimised modelled spectra for the reflectance spectra of water, from the shuriken structures, when phase is ignored (blue dashed), and when the phase is considered in the fitting parameters (red). From this figure, it is important to note that the reflectance spectra, recorded for the shuriken structures here, cannot be well replicated using the coupled oscillator model previously used [4, 11], but requires any retardation phase shifts to be considered (Figure 3.20(a)). The requirement of including phase in the fitting model, is a result of retardation effects becoming significant due to the size of the nanostructures now being comparable to the wavelength of light, which is different to EIT in atomic systems. In previous studies, where plasmonic induced transparency has been modelled using the coupled oscillator model without the introduction of phase shifts, the nanostructures used have been of a much smaller size and therefore retardation effects would have been much less significant [4]. In Figure 3.20(b-d), the values ω_r , ω_d , k , θ , and ϕ for the fitted spectra were plotted against the refractive index of the solutions. As is expected for achiral solutions, both ω_r and ω_d exhibit a wavelength shift that increases linearly as a function of the refractive index for both left- and right-handed nanostructures. All four values, radiative and dark resonances for both handedness of structures, show the same refractive index sensitivity, within the precision of our measurements, of ~ 400 nm/RIU. All three of the other variable parameters, k , θ , and ϕ , all show no changes within the error of our measurements, meaning there are no refractive index dependencies on the coupling or phase parameters for achiral media.

3.7 References

1. Gadegaard, N., S. Mosler, and N.B. Larsen, *Biomimetic Polymer Nanostructures by Injection Molding*. Macromolecular Materials and Engineering, 2003. **288**(1): p. 76-83.
2. Hentschel, M., et al., *Babinet to the half: coupling of solid and inverse plasmonic structures*. Nano Letters, 2013. **13**(9): p. 4428-4433.
3. Prodan, E., et al., *A hybridization model for the plasmon response of complex nanostructures*. Science, 2003. **302**(5644): p. 419-422.
4. Zhang, S., et al., *Plasmon-Induced Transparency in Metamaterials*. Physical Review Letters, 2008. **101**(4): p. 047401.
5. Tang, Y. and A.E. Cohen, *Optical chirality and its interaction with matter*. Physical Review Letters, 2010. **104**(16): p. 163901.
6. Hendry, E., et al., *Ultrasensitive detection and characterization of biomolecules using superchiral fields*. Nature Nanotechnology, 2010. **5**(11): p. 783-787.
7. Tang, Y. and A.E. Cohen, *Enhanced enantioselectivity in excitation of chiral molecules by superchiral light*. Science, 2011. **332**(6027): p. 333-336.
8. Sigal, G.B., et al., *A Self-Assembled Monolayer for the Binding and Study of Histidine-Tagged Proteins by Surface Plasmon Resonance*. Analytical Chemistry, 1996. **68**(3): p. 490-497.
9. Bornhorst, J.A. and J.J. Falke, *Purification of proteins using polyhistidine affinity tags*, in *Methods in Enzymology*. 2000, Academic Press. p. 245-254.
10. Chaki, N.K. and K. Vijayamohanan, *Self-assembled monolayers as a tunable platform for biosensor applications*. Biosensors and Bioelectronics, 2002. **17**: p. 1-12.
11. Tassin, P., et al., *Electromagnetically Induced Transparency and Absorption in Metamaterials: The Radiating Two-Oscillator Model and Its Experimental Confirmation*. Physical Review Letters, 2012. **109**(18): p. 187401.

Chapter 4: Detection of Ligand Induced Changes in Protein Higher Order Structure

4.1 Introduction

Traditionally, X-ray crystallography [1], and nuclear magnetic resonance (NMR) [2] are the two common techniques that are routinely employed to determine and characterise the higher order structure of proteins. These techniques however, require a lot of material, and are very time consuming, with NMR failing when larger proteins are being elucidated. As a result of these limitations, X-ray crystallography and NMR are unsuitable for the high throughput characterisation of proteins required for many analytical applications.

Optical spectroscopic techniques typically do not provide a spectral fingerprint of the higher order structure of proteins, such as the tertiary or quaternary structural changes seen for many protein-ligand interactions. In this chapter, we will demonstrate that the optical response of the chiral plasmonic nanostructures are sensitive to the higher order structural changes observed in many proteins. The phenomenon introduced here, 'superchiral' polarimetry, is a label-free and chirally sensitive spectroscopic technique. Which will be shown to be sensitive to ligand induced changes in the higher order structures of two well characterised proteins, that are not detected when using conventional methods, such as circular dichroism. This increased sensitivity arises from the smaller mismatch between the effective helical pitch of the superchiral fields and the length scale of the protein structures, when compared with circularly polarised light. This is demonstrated using two proteins from the Shikimate pathway, EPSP Synthase and Shikimate Kinase, which both undergo well defined ligand induced structural changes. Each protein differs in size, ligand affinity, and the nature of the ligand induced conformational change, making them the ideal test for exhibiting this new approach.

The phenomenon, 'superchiral' polarimetry, relies upon measuring optical rotatory dispersion (ORD) spectra, and characterising the changes in these spectra using the asymmetry parameter, $\Delta\Delta\lambda$, described in Chapter 3. This is a rather simplistic interpretation of the data measured from the chiral shuriken structures, and further protein binding characteristics will be examined in chapters 5, 6, and 7 using a more detailed interpretation of the reflectance spectra recorded from each nanostructure.

4.2 Proteins

4.2.1 The Shikimate Pathway

The shikimate pathway is a seven step metabolic process, found only in microorganisms and plants, that leads to the production of aromatic amino acids. Since the pathway is not found in animals, interrupting this pathway is an important target for many herbicides, such as glyphosate [3]. Two of the enzymes from the shikimate pathway, 5-enolpyruvylshikimate-3-phosphate (EPSP) synthase from *Escherichia coli* and shikimate kinase (SK) from *Erwinia chrysanthemi*, were chosen for this study, as they both undergo ligand induced conformational changes but differ in size, ligand affinity, and the nature of the conformational changes.

4.2.2 5-enolpyruvylshikimate-3-phosphate (EPSP) synthase

The enzyme 5-enolpyruvylshikimate-3-phosphate (EPSP) synthase is the sixth enzyme in the shikimate pathway, and catalyses the reaction between shikimate-3-phosphate (S3P) and phosphoenolpyruvate (PEP) to form 5-enolpyruvylshikimate-3-phosphate (EPSP). It is a 46 kDa molecular weight protein, that folds into two similar domains, as seen in Figure 4.01(a).

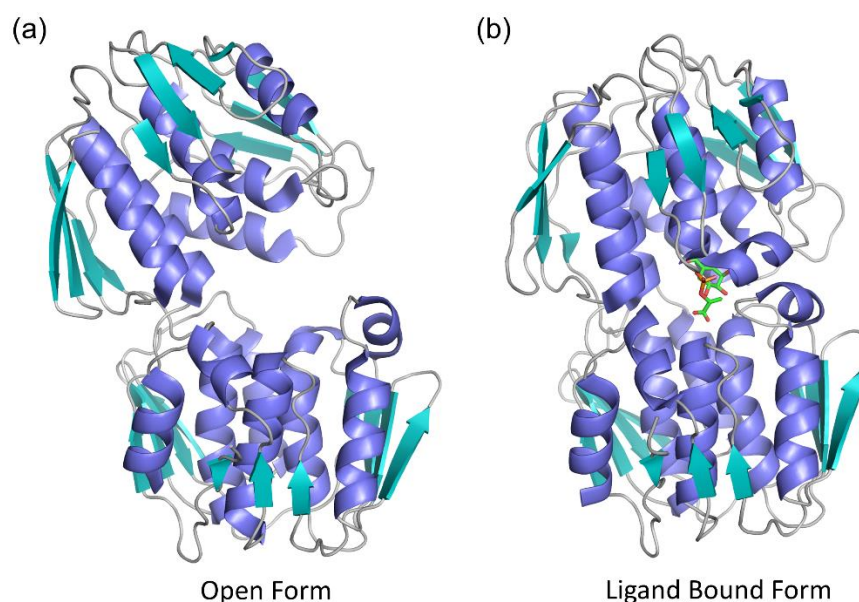


Figure 4.01 Ribbon representations of the crystal structure of EPSP Synthase (a) open form of protein (PDB 2BJB), and (b) closed form of protein after binding (PDB 2O0E) of glyphosate and shikimate-3-phosphate ligand.

Protein crystallography data has been extensively studied for EPSP Synthase, which provides high resolution structures for both the open form and ligand bound form of the specific protein, or closely related species [4, 5]. The crystal structures, and ribbon representations shown in Figure 4.01, show that EPSP Synthase exists as a monomer that is comprised of two similar domains connected by a flexible strand. Upon ligand binding, the ligand interacts with both domains of the protein bringing them closer together in a screw-like movement, with the active site being in the interdomain cleft, Figure 4.01(b) [6]. As a result of this 'hinge' closure, a more compact structure and rigid alignment of the α - helices and β -sheets is produced. The ligands that bind to EPSP Synthase to irreversibly induce this conformational change are; shikimate-3-phosphate (S3P), and the inhibitor glyphosate. Glyphosate acts as the primary inhibitor of EPSP Synthase and is the active ingredient found in most commercially available herbicides. Both these ligands, S3P and glyphosate, bind to EPSP Synthase with low micromolar affinities [7].

4.2.3 Shikimate Kinase (SK)

Shikimate kinase (SK) is the fifth enzyme in the shikimate pathway, and is responsible for catalysing the ATP dependent phosphorylation of the 3-hydroxyl group of shikimic acid, to form shikimate-3-phosphate. The structure of shikimate kinase is very different compared with EPSP Synthase, as it is a much smaller protein at 19 kDa, and is a single domain structure, as shown in Figure 4.02.

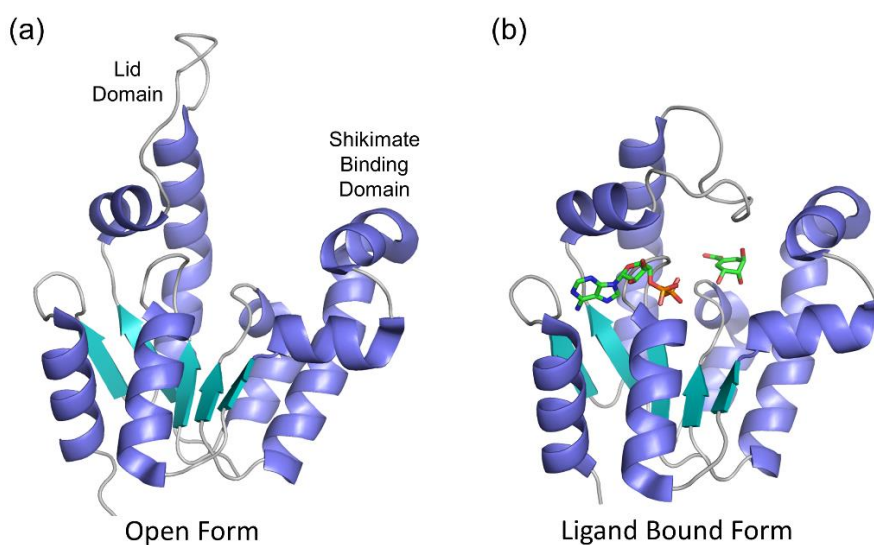


Figure 4.02 Ribbon representations of the crystal structure of SK (a) open form of protein (PDB 2IYV), and (b) closed form of protein after binding (2IYQ) of ADP, shikimic acid and $MgCl_2$.

Protein crystallography data, as well as molecular modelling, has been used to provide detailed structures for the open, and closed ligand bound structures of shikimate kinase [8, 9]. The SK enzyme is an α/β protein that is composed of two major domains; the lid domain, and the shikimate binding (SB) domain. Upon ligand binding, a hinged movement of the lid domain and shikimate binding domain occurs, bringing them closer to each other, and towards the active centre of the protein [10]. This results in the small lid domain 'closing' over the active site on ADP binding, and the helix-loop-helix of the SB domain becoming more ordered, as shown in Figure 4.02(b). This conformational change is induced by ligand solutions containing ADP, shikimic acid, and $MgCl_2$, with the protein binding these ligands with high micromolar to low millimolar affinities [11].

4.3 Results and Discussion

4.3.1 Immobilisation Coverage

As the two proteins used throughout this study undergo significant structural changes upon ligand binding, the surface coverage of the protein becomes an important parameter. To control the surface coverage of the proteins, self-assembled monolayers of increasing NTA concentrations were immobilised onto the nanostructure surface, and EPSP synthase added. Figure 4.03 shows the correlation between the overall coverage of EPSP synthase, and the asymmetry value produced.

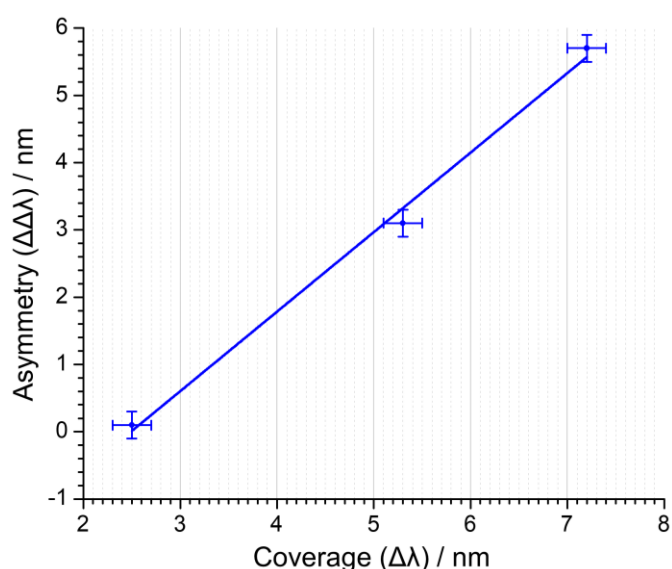


Figure 4.03 Asymmetry values against corresponding surface coverage for increasing coverage of EPSP synthase immobilised onto the shuriken nanostructures. The error bars represent the standard error calculated from 8 spectra measurements.

Figure 4.03 shows that as the coverage of EPSP Synthase on the surface of the nanostructures increases, as measured by the average shift from the left- and right-handed structures, there is a linear increase in the asymmetry value observed. Even though a greater surface coverage of the protein produces a much larger asymmetry, it is not always beneficial to have such a high coverage. The middle coverage shown in Figure 4.03, is the NTA concentration used throughout this chapter, with an NTA/EG-thiol concentration of 0.1 mM/0.9 mM, respectively. This coverage was chosen throughout as it gives a significant asymmetry response for the proteins with the chiral shuriken structures, but also creates large enough spacing between the immobilised proteins to allow unhindered structural changes upon binding of the respective ligands.

4.3.2 Measurement of Protein Structural Changes

The proteins, EPSP Synthase and shikimate kinase, were both recombinant histidine tagged (His-tagged) proteins that were immobilised on the gold substrate surface using an established methodology [12], described in chapter 3. This allows the proteins to be adsorbed to the surface in a well-defined fashion, as the His-tag is positioned on the N-terminus of the proteins, giving a consistent relative binding orientation across the whole substrate. As a result of the defined binding orientation of the protein to the surface, and the spacing of the protein binding sites created by the NTA/EG-thiol monolayer, the conformational changes in the structure can occur unhindered upon ligand binding to the protein. ORD measurements were taken for both handedness of shuriken structures, after the formation of the NTA/EG-thiol SAM on the substrate surface, in the presence of buffer, and used as the initial reference spectra. This was repeated after the adsorption of the proteins, and after the introduction of the ligand solutions to the adsorbed proteins. The spectra for each measurement was then plotted for buffer alone, immobilised protein in buffer, and immobilised protein in the presence of ligand solution, Figure 4.04. The ORD spectra for ligand only solutions, and the average shifts for each stage of the protein measurements (protein immobilisation, ligand binding to adsorbed proteins, and ligand only solutions), are included in Appendix C. The average shifts for the structures can be thought of as being analogous to surface plasmon resonance measurements, and were calculated as $\Delta\lambda_{Avg} = (\Delta\lambda_R + \Delta\lambda_L)/2$, where $\Delta\lambda_R$ and $\Delta\lambda_L$ are the shifts for the right- and left-handed nanostructures respectively.

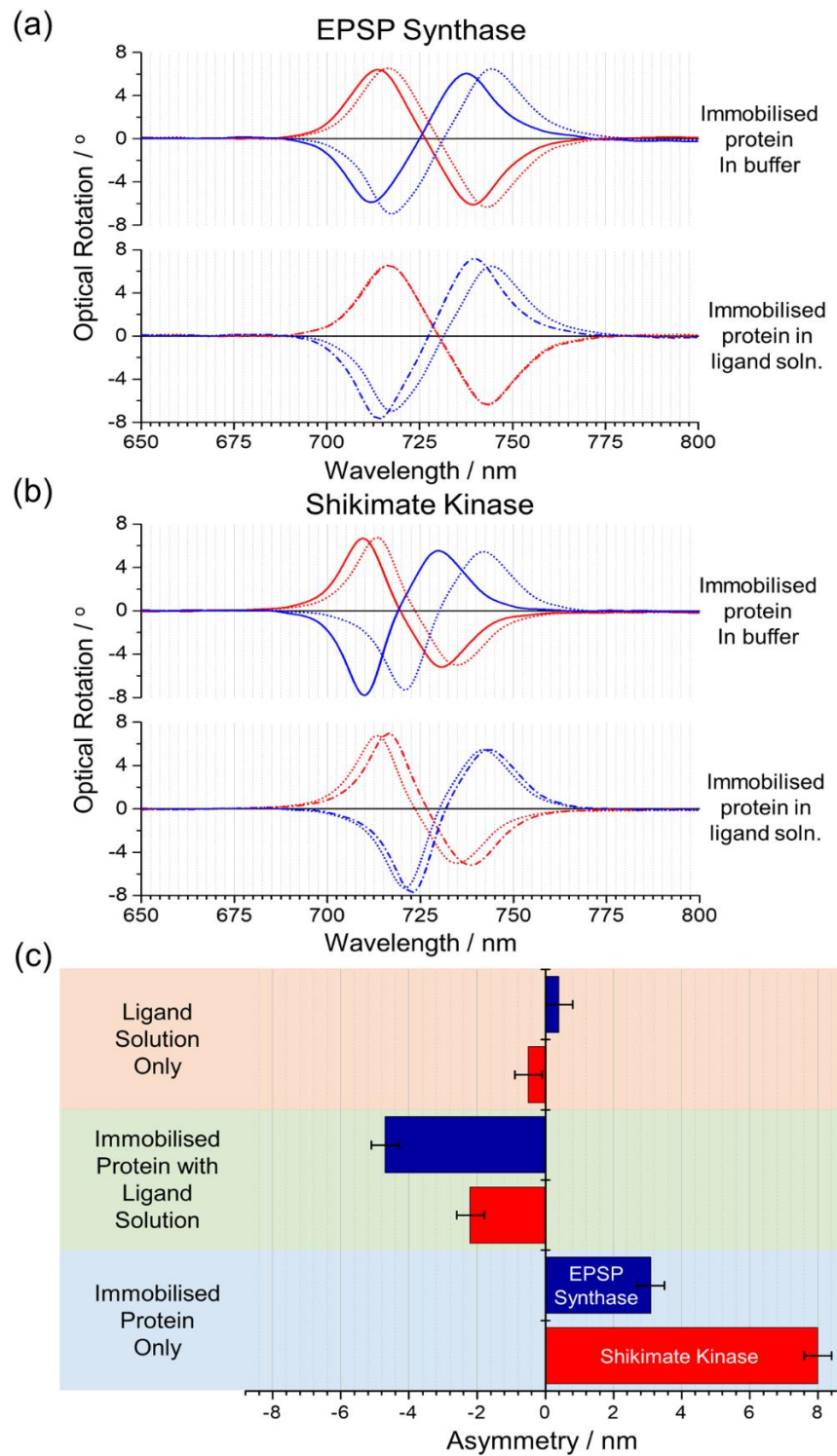


Figure 4.04 ORD data for (a) EPSP Synthase, and (b) shikimate kinase. The top graph of each show the spectra in the presence of buffer only (solid line) to immobilised protein in the presence of buffer (dotted lines), and the bottom graph of each shows the spectra for immobilised protein (from top graph) and immobilised protein in the presence of ligand solutions (dash-dot line). (c) shows $\Delta\Delta\lambda$ values calculated from the ORD spectra for immobilised protein, protein in the presence of ligand solution, and ligand solution only. The error bars represent the standard error calculated from 8 spectra measurements.

Figure 4.04 shows the spectra for both proteins, EPSP Synthase and shikimate kinase, after immobilisation of the protein relative to the initial buffer measurements, and after addition of the ligand solutions to the immobilised proteins, relative to the previous immobilised protein only measurements. The ligand solutions also contain chiral molecules, with shikimic acid, ADP, and shikimate-3-phosphate all containing chiral centres. As a control on the effect of the chirality of the ligand solutions, ORD measurements were recorded in the presence of each respective ligand solution, in the absence of any adsorbed protein. The asymmetry parameter values, $\Delta\Delta\lambda$ introduced in chapter 3, for the immobilised protein, immobilised protein in the presence of ligand solution, and ligand solution only in the absence of protein are also included in Figure 4.04(c), showing no asymmetry for either solution within experimental error. The asymmetry parameter for the immobilised protein is calculated relative to the initial buffer measurement, and relative to the immobilised protein position for the protein and ligand solution measurements.

Upon immobilising the proteins on the substrate surface, both EPSP Synthase and shikimate kinase produced positive asymmetry values significantly larger than the values seen for the ligand solutions alone. When the ligand solutions were added to the respective adsorbed proteins, the conformational changes induced for each protein both produce a large negative $\Delta\Delta\lambda$ response, relative to the initial immobilisation value. With EPSP synthase showing the largest asymmetry upon ligand binding, as seen in Figure 4.04.

4.3.3 Circular Dichroism Spectroscopy

As a comparison to conventional spectroscopy, UV-Vis circular dichroism (CD) spectra were also recorded for both protein systems. The CD spectra were collected for both proteins on their own, as well as with the relative ligand solutions present, meaning spectra could be obtained for the proteins in their unliganded (open) and ligand bound (closed) states. The spectra were also collected for both the far and near UV regions, which are sensitive to the secondary and tertiary protein structure respectively. The UV-Vis CD spectra for both proteins in the near and far UV regions, for both open and closed ligand bound structures are shown in Figure 4.05.

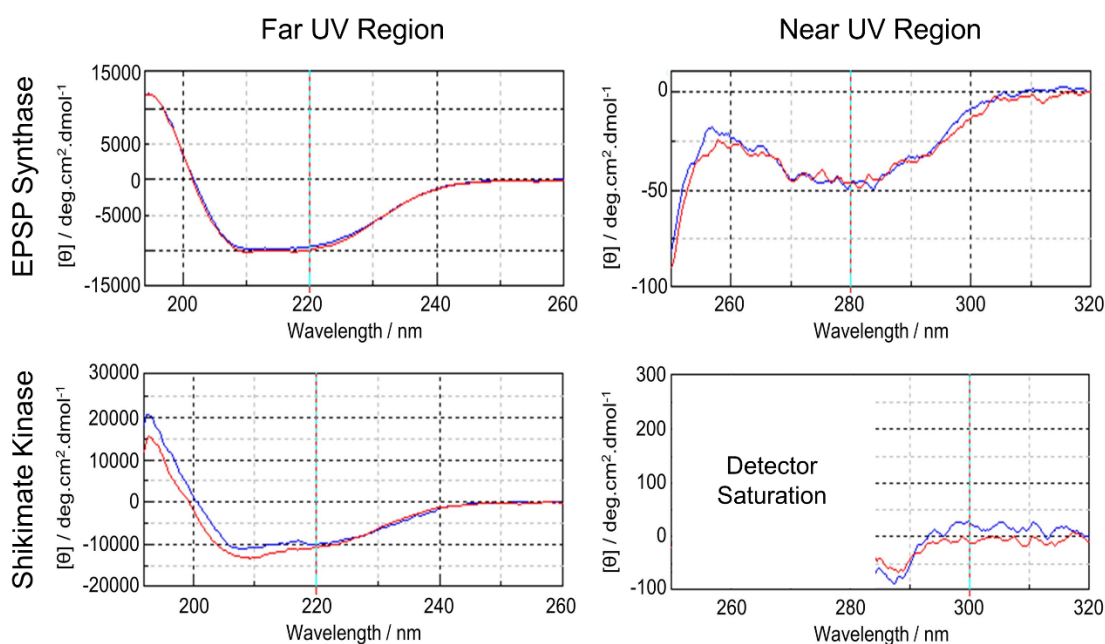


Figure 4.05 CD spectra for unliganded (blue) and ligand bound (red) protein, for EPSP Synthase and shikimate kinase in the top and bottom panels respectively. Spectra are shown for both the far UV and near UV spectra, in the left and right panels respectively.

In CD spectroscopy, the far UV and near UV regions are sensitive to the secondary and tertiary structure of the proteins respectively, with the tertiary sensitivity of near UV arising from changes in the surrounding environments of the aromatic amino acids present within the structure. [13]. In the CD spectra for EPSP Synthase, it can be seen that there are no changes in either the far UV or near UV spectra when the protein goes from its unliganded open form, to its closed ligand bound form. Indicating that in the case of EPSP Synthase, CD spectroscopy is insensitive to the large changes in the quaternary structure that occur upon the ligand induced conformational change. In the case of shikimate kinase, the near UV spectra is uninformative as it overlaps a region where the unbound ligand solution absorbs light, limiting the collection of good quality data in this region. In the far UV region, a small change can be seen upon ligand binding for shikimate kinase, with no significant change seen in the near UV spectra for the limited range observable. This would suggest for the shikimate kinase that there is a slight change in the secondary structure of the protein, but no significant change in the tertiary structure. These results differ from the bench mark protein crystallography data published, however similar behaviour in the CD spectra for shikimate kinase has been observed in a related study [14]. These changes in the far UV region CD spectra for shikimate kinase upon ligand binding were attributed to an altering of the relative orientations of

the secondary structure, α -helices and β -sheets, rather than a change in the secondary structure content. These results suggest that the conformational changes observed in the higher order structure of these two proteins, are unobservable using conventional circular dichroism spectroscopy.

4.3.4 Discussion

Since the proteins are immobilised on the nanostructure surface through the binding of the His-tag to the NTA/EG-thiol self-assembled monolayer, the proteins are immobilised with a consistent orientation relative to the surface. Superchiral polarimetry has been shown to be sensitive to the anisotropy of chiral molecules, and has previously been used to distinguish between globular proteins, with high α -helical content, and more structurally anisotropic proteins, with high β -sheet content [15]. The two proteins, EPSP Synthase and shikimate kinase, do not undergo any significant changes to their secondary structure content upon ligand binding, but do undergo changes in the quaternary and tertiary structures respectively, as seen from the X-ray structures of both proteins. As circular dichroism measurements, and other chiroptical spectroscopy measurements, are typically only sensitive to the secondary structure content of proteins, and a much lesser extent tertiary structure, the changes that occur here upon ligand binding to the proteins cannot be detected using these methods. This is proven in the circular dichroism measurements shown for both example proteins in Figure 4.05. However, by employing the phenomenon of plasmonic polarimetry, ligand induced structural changes can be detected in the tertiary and quaternary structures of shikimate kinase and EPSP Synthase respectively, as shown in Figure 4.04. Figure 4.04(c) also shows the asymmetry values resulting from the addition of ligand solutions to the nanostructured surface, in the absence of any adsorbed protein. These results show that the ligand solutions alone, even though they contain chiral small molecules, do not have any significant effects on the ORD spectra produced. This is to be expected for the small molecules within the ligand solutions, as they occupy a much smaller volume of the available chiral fields. Hence, compared with the protein samples, have a much lesser impact on the fields, and do not produce any net chiral asymmetry. This reinforces the results induced by the protein structural changes, as it confirms that the asymmetry differences produced are due to the conformational changes of the protein upon ligand binding, without the ligand solutions contributing to the $\Delta\Delta\lambda$ values.

The increased sensitivity of plasmonic polarimetry, to higher order structural changes in protein molecules, is due to the superchiral nature of the evanescent fields produced by the chiral nanostructures, compared with the circularly polarised light used in circular dichroism measurements. This means that the effective helical pitch of the chiral evanescent field matches the length scale of the higher order protein structure, typically 10-100 nm, a lot more closely than that of circularly polarised light. However, the sensitivity of plasmonic polarimetry relative to conventional optical spectroscopy techniques can in part be attributed to the quadrupolar contribution to optical activity [15]. Normally, conventional chiroptical phenomena such as circular dichroism is derived from the higher-order effects, with the largest of the contributions coming from the electric dipole-magnetic dipole (dipolar) and electric dipole-electric quadrupole (quadrupolar) interactions. However, the electric dipole-electric quadrupole interactions average to zero in achiral media. With conventional excitation by circularly polarised light in CD spectroscopy, the dipolar and quadrupolar terms can contribute to the optical activity with the same order of magnitude for anisotropic materials [16]. Alternatively, the superchiral fields produced around the chiral shuriken nanostructures here, can display steep field gradients. These steep field gradients were found by Efrima [17] to enhance any quadrupolar contributions, relative to the dipolar contributions, to optical activity. The influence of these gradients of localised electromagnetic fields around the chiral nanostructures on the quadrupolar contribution to optical activity, has been shown to increase the asymmetry factors produced for anisotropic media [17]. However, this will be further investigated for the chiral shuriken structures in chapters 5 and 6, using the coupled oscillator model described in chapter 3, to create a deeper understanding of any effects the dipolar and quadrupolar contributions have on the optical properties of the nanostructures.

4.4 Conclusion

In this chapter, we have introduced a new optical spectroscopy phenomenon, 'superchiral' polarimetry, using injection moulded chiral shuriken nanostructures. This phenomenon shows the power of using chiral evanescent fields with enhanced chiral asymmetries for probing the higher order structures of biomolecules. Two proteins, EPSP Synthase and shikimate kinase, were used as exemplar systems to show the sensitivity of superchiral polarimetry as a probe into the changes induced upon ligand

binding. With both proteins undergoing higher order structural changes, in the tertiary and quaternary structure, with no changes in the secondary structure content.

The sensitivity of this method to higher order structural changes, exploits the generation of superchiral fields around the chiral shuriken structures, combined with the chiral fields around the nanostructures displaying steep field gradients. Chirally sensitive spectroscopy methods, such as circular dichroism, are based on the differential interaction of left- and right-handed circularly polarised light, which results in them being inherently insensitive to higher order structural changes. The superchiral fields generated by our chiral shuriken nanostructures have been shown, through the electromagnetic modelling simulations (shown in chapter 3), to display a chiral asymmetry an order of magnitude greater than that of circularly polarised light. With the local chiral fields around the nanostructures displaying steep field gradients that enhance any quadrupolar contributions to optical activity, resulting in an increase in any asymmetry obtained for anisotropic media. This provides a rather simplistic interpretation of the data, and in chapters 5, 6, and 7, a greater understanding of the chiral nanostructure interactions will be developed using the coupled oscillator model described in chapter 3.

In summary, the results shown throughout this chapter demonstrate that superchiral polarimetry can readily detect higher order structural changes in immobilised proteins, which cannot be measured with conventional CD spectroscopy. The conformational changes detected for the two exemplar proteins demonstrate that, in agreement with previous studies of this phenomenon [15], superchiral polarimetry is sensitive to any changes in the anisotropy of the protein structures. Hence, in effect, can detect any changes in the relative positions of the secondary structure units within the protein.

4.5 References

1. Drenth, J., *Principles of protein X-ray crystallography*. 3rd ed. 2007: Springer Science & Business Media.
2. Kainosho, M., et al., *Optimal isotope labelling for NMR protein structure determinations*. *Nature*, 2006. **440**(7080): p. 52-57.
3. Herrmann, K.M. and L.M. Weaver, *The shikimate pathway*. *Annual Review of Plant Biology*, 1999. **50**(1): p. 473-503.
4. Pereira, J.H., et al., *Structural bioinformatics study of EPSP synthase from Mycobacterium tuberculosis*. *Biochemical and Biophysical Research Communications*, 2003. **312**(3): p. 608-614.
5. Park, H., et al., *Structural studies of Streptococcus pneumoniae EPSP synthase in unliganded state, tetrahedral intermediate-bound state and S3P-GLP-bound state*. *Molecular Microbiology*, 2004. **51**(4): p. 963-971.
6. Schönbrunn, E., et al., *Interaction of the herbicide glyphosate with its target enzyme 5-enolpyruvylshikimate 3-phosphate synthase in atomic detail*. *Proceedings of the National Academy of Sciences*, 2001. **98**(4): p. 1376-1380.
7. Ream, J.E., et al., *EPSP synthase: binding studies using isothermal titration microcalorimetry and equilibrium dialysis and their implications for ligand recognition and kinetic mechanism*. *Biochemistry*, 1992. **31**(24): p. 5528-5534.
8. Pereira, J.H., et al., *Structure of shikimate kinase from Mycobacterium tuberculosis reveals the binding of shikimic acid*. *Acta Crystallographica Section D: Biological Crystallography*, 2004. **60**(12): p. 2310-2319.
9. Pauli, I., R.A. Caceres, and W.F. de Azevedo, *Molecular modeling and dynamics studies of Shikimate Kinase from Bacillus anthracis*. *Bioorganic & Medicinal Chemistry*, 2008. **16**(17): p. 8098-8108.
10. Dias, M.V.B., et al., *Effects of the magnesium and chloride ions and shikimate on the structure of shikimate kinase from Mycobacterium tuberculosis*. *Acta Crystallographica Section F: Structural Biology and Crystallization Communications*, 2007. **63**(1): p. 1-6.
11. Cerasoli, E., et al., *Effects of salts on the function and conformational stability of shikimate kinase*. *Biochimica et Biophysica Acta (BBA)-Proteins and Proteomics*, 2003. **1648**(1): p. 43-54.
12. Sigal, G.B., et al., *A Self-Assembled Monolayer for the Binding and Study of Histidine-Tagged Proteins by Surface Plasmon Resonance*. *Analytical Chemistry*, 1996. **68**(3): p. 490-497.
13. Kelly, S.M., T.J. Jess, and N.C. Price, *How to study proteins by circular dichroism*. *Biochimica et Biophysica Acta (BBA)-Proteins and Proteomics*, 2005. **1751**(2): p. 119-139.
14. Krell, T., J.R. Coggins, and A.J. Laphorn, *The three-dimensional structure of shikimate kinase1*. *Journal of Molecular Biology*, 1998. **278**(5): p. 983-997.
15. Hendry, E., et al., *Ultrasensitive detection and characterization of biomolecules using superchiral fields*. *Nature Nanotechnology*, 2010. **5**(11): p. 783-787.
16. Barron, L.D., *Molecular light scattering and optical activity*. 2004: Cambridge University Press.

17. Efrima, S., *Raman optical activity of molecules adsorbed on metal surfaces: Theory*. The Journal of Chemical Physics, 1985. **83**(3): p. 1356-1362.

Chapter 5: Orientation Determination of Adsorbed Structurally Similar Affimers

5.1 Introduction

The orientation of biomolecules, such as proteins, on surfaces can be crucial for a range of biological functions. This interface functionality is reliant upon the orientation of the surface bound proteins, as in many cases the active sites of immobilised proteins are inaccessible to targets in the solution [1]. Not only this, but proteins at interfaces with controlled orientations have been shown to possess higher activity than surfaces where the proteins are bound in random orientations [2]. However, since interfaces consist of a relatively small amount of material, conventional chiroptical spectroscopy cannot be used to determine the protein orientation due to a lack of sensitivity.

In this chapter, we will show how we can discriminate between three structurally similar protein fragments, called Affimers, adsorbed onto the metamaterial surface with differing orientations. In the previous chapter, the asymmetry parameter ($\Delta\Delta\lambda$), was interpreted as a way of detecting higher order structural changes in proteins. However, plasmonic polarimetry is a rather simplistic interpretation of the data, and produces much smaller changes when studied theoretically [3]. Here we will develop a greater understanding of the nanostructured system, using three new asymmetry parameters extracted from the experimental reflectance spectra. As the reflectance spectra from the chiral shuriken structures display plasmonic induced transparency (described in chapter 3), the experimental asymmetry parameter $\Delta\Delta S$ can be interpreted in a similar way to the previously used $\Delta\Delta\lambda$. The experimental data can then be modelled, using the coupled oscillator model introduced in chapter 3, to provide two asymmetry parameters for the phase retardation of the bright and dark plasmonic modes, $\Delta\Delta\theta$ and $\Delta\Delta\phi$ respectively.

We will show that by interpreting the reflectance data in this way, we can readily distinguish between the three structurally similar Affimer proteins when they are immobilised in different well-defined orientations. This phenomenon arises from the sensitivity of the phase retardation effects on the spatial arrangement of the Affimer molecules within the nearfield of the nanostructures. Hence, the immobilised Affimer proteins cause an asymmetry in the phase retardation between left- and right-handed structures due to the differential interaction of the chiral near fields with the chiral dielectric environment.

5.2 Affimers

Affimers, unlike antibodies, are based upon non-immunoglobulin scaffolds, with around 20 different types of non-antibody scaffolds being known [4]. All Affimers consist of the same scaffold protein, based on either mammalian Stefin A or plant Cystatin A, with a homologous tertiary structure throughout.

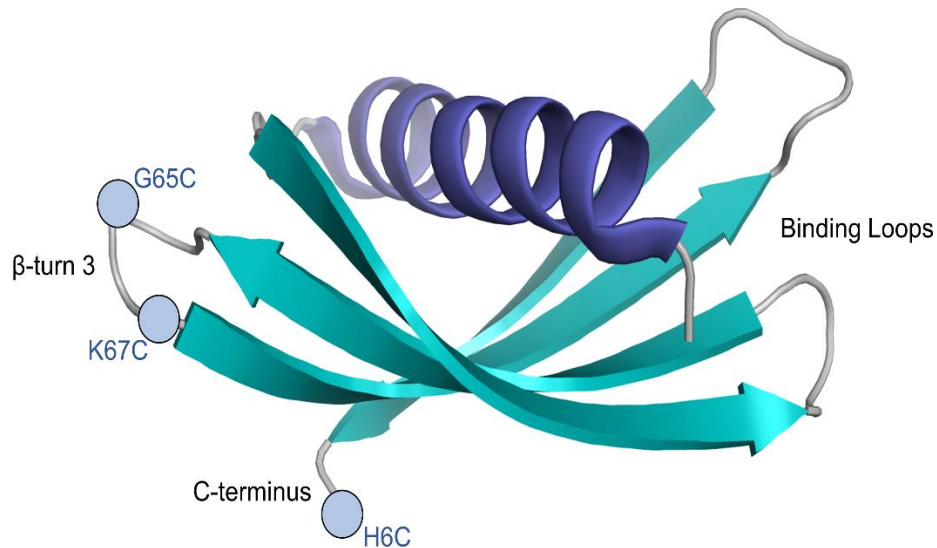


Figure 5.01 Ribbon representation of Affimer protein scaffold (PBD 4N6U), labelled with the positions of the inserted cysteines for the three different Affimers.

All three Affimers used throughout this study were based on the plant cystatin scaffold, that creates a well-defined tertiary structure composed of an anti-parallel β -sheet and a central helix, as shown in Figure 5.01. The scaffold produced by the Affimer proteins, has two binding loops which can be varied in the phage display library containing 10^{10} randomised sequences, that can be used to generate Affimers with high affinity surfaces (nM) for specific targets. However, the scaffold and binding loops of the Affimers have been engineered to contain no cysteine residues, which allows a cysteine to be inserted at a specific, unique site to provide a simple method of immobilising these Affimer molecules to surfaces with a known orientation [5]. Three variants of the Affimers have been used here (G65C, K67C, and H6C), with each one having the cysteine residue inserted into a different position. For G65C and K67C, the cysteine residue was inserted into the β -turn 3 loop of the Affimer, located on the opposite face to the binding loops, with the position of each only differing by two residues in the primary sequence. However, for the H6C Affimer, the cysteine residue was inserted into the C-terminus loop of the protein, shown in Figure 5.01. As

the binding loops can also be engineered, to provide specific binding of targets, two of the Affimer variants (G65C and K67C) were engineered to bind glutathione S-transferase (GST), and one of the Affimers (H6C) was engineered to be specific for immunoglobulin G (IgG). The three otherwise structurally identical Affimer structures can be immobilised onto the gold surface of the nanostructures, through the thiol of the cysteine residue, with different well-defined orientations.

5.3 Results and Discussion

5.3.1 Measurement of Affimers

As a measure for this new approach, three Affimer samples were obtained from Avacta life sciences. For each of the three Affimer variants, reflectance measurements were recorded at all stages of immobilisation and binding. This includes Affimer immobilisation, polyethylene glycol (PEG) filler immobilisation, and binding of target protein to Affimers (described in Appendix D). For each reflectance measurement, the average shifts were calculated as well as the separation asymmetry parameter, $\Delta\Delta S$, described in chapter 3. The average shift for each measurement is calculated as the average shift of the two dips in reflectance for left- ($\Delta\lambda_L$) and right-handed ($\Delta\lambda_R$) nanostructures, and then described as $\Delta\lambda_{Avg} = (\Delta\lambda_R + \Delta\lambda_L)/2$. The average shift measurements that are recorded here, can be thought of as being analogous to conventional surface plasmon resonance measurements, and are dependent on the surface coverage of the material. Figure 5.02 shows the average shift data, relative to buffer, for the initial immobilised Affimer, addition of the PEG filler, and binding of the relative target protein for all three Affimer variants. Upon initial binding of the Affimer, and addition of the PEG filler to the surface, all three Affimer variants (K67C, G65C, and H6C) produce an identical average shift value within experimental error. This shows that each of the three Affimer variants, as expected, have the same coverage on the nanostructure surface, due to them all containing the same protein scaffold. Meaning that the three different orientations would not be distinguishable using the average shift measurements obtained from the reflectance spectra.

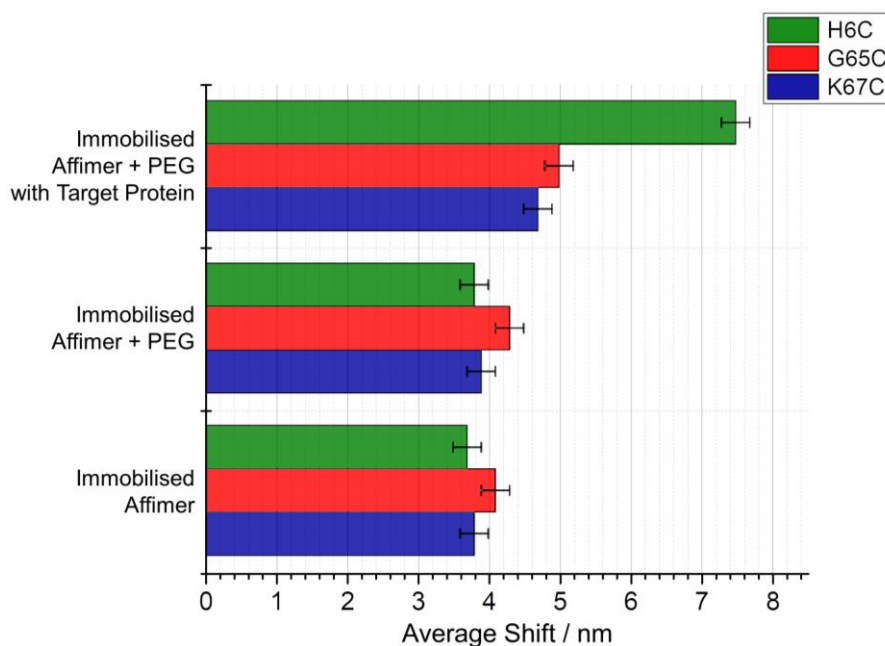


Figure 5.02 Bar chart showing average shifts for 3 Affimers; K67C (blue), G65C (red), and H6C (green). Showing average shifts for immobilisation of Affimer, addition of PEG filler, and binding of target protein to Affimer (K67C and G65C bind GST, and H6C binds IgG), all relative to initial buffer measurement. The error bars represent the standard error calculated from 8 spectra measurements.

When the respective target protein is added, either GST or IgG, the Affimers that bind the different proteins do become distinguishable. However, the two Affimers that both bind GST as the target protein (K67C and G65C) are still unable to be separated using the average shift measurements shown in Figure 5.02. This is caused by the differences in size of the target proteins, as GST is a 25 kDa sized protein with IgG being 150 kDa in size. This difference in size means that it is easy to distinguish between binding of IgG and GST, hence between H6C and the two GST binders, whereas it remains impossible to see the difference between K67C and G65C, as they both bind the same GST target.

To interpret the reflectance data measured for the three separate Affimer variants further, a separation asymmetry parameter is introduced, $\Delta\Delta S$, as described in chapter 3. This asymmetry parameter, like the $\Delta\Delta\lambda$ parameter introduced for the ORD spectra in the previous chapter, can be used to quantify any chiral asymmetry effects upon the left- and right-handed nanostructures resulting from the adsorbed proteins.

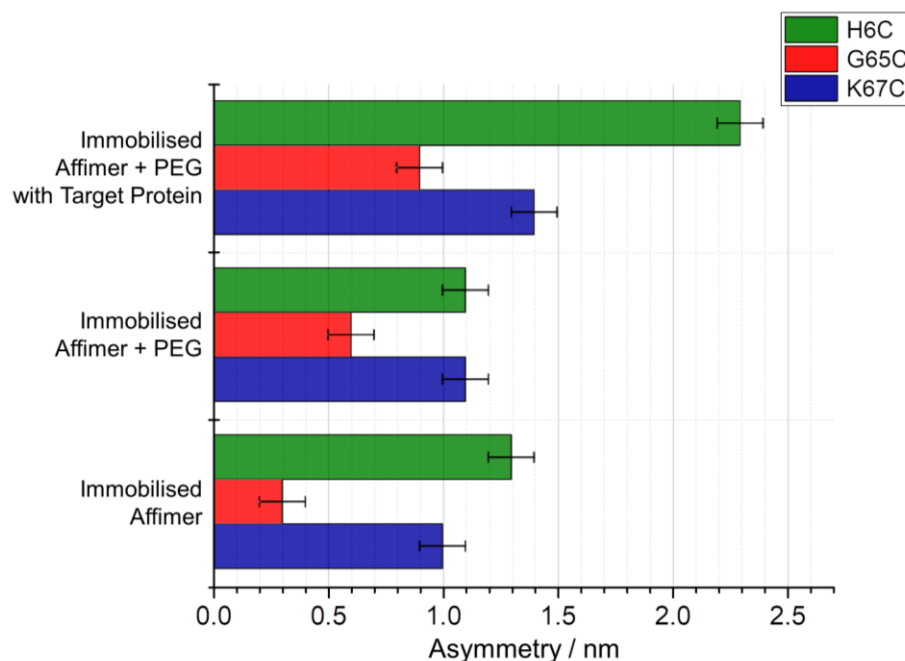


Figure 5.03 Bar chart showing asymmetry values calculated for 3 Affimers; K67C (blue), G65C (red), and H6C (green). Showing asymmetry values for immobilisation of Affimer, addition of PEG filler, and binding of target protein to Affimer (K67C and G65C bind GST, and H6C binds IgG), all relative to initial buffer measurement. The error bars represent the standard error calculated from 8 spectra measurements.

Figure 5.03 shows all $\Delta\Delta S$ values calculated for the immobilisation of the Affimers, addition of PEG filler, and binding of the target protein to immobilised Affimer for all three variants. Instantly, it can be seen that when the three different Affimers are immobilised on the nanostructure surface, they each give a unique response compared to what was observed for the average shift measurements. The results show, that even though all three Affimer variants share the same protein scaffold, by inserting the cysteine residue at a different position in the sequence, and hence changing the binding orientation of the Affimer to the surface, a significant difference in the separation asymmetry can be detected. Although the position of the cysteine residue in K67C and G65C only differs by two amino acid residues on the same β -turn 3 loop, the difference in orientation of the two Affimers on the surface produces a substantial difference in the asymmetry parameter of the two variants. With the H6C, IgG binding variant His-tagged on the C-terminus loop, producing the largest response. When the PEG filler is added to the immobilised Affimers, there are small responses for all three variants. This suggests that the binding of the PEG to fill in any gaps on the surface of the nanostructures, changes the orientation of the Affimers

slightly causing a small change in the asymmetry value obtained. After this has occurred, the difference between the two Affimers with the cysteine inserted in the β -turn 3 loop still produce significantly different responses to each other, however the H6C response becomes indistinguishable to the K67C variant. The responses from the three Affimers after the respective target proteins have been added, then again become three separate and distinct values, with the H6C Affimer producing the largest asymmetry overall, after IgG binding. This suggests that, before target protein binding to the respective Affimers, the orientation of the K67C and H6C Affimers are in similar orientations to each other, but then become easily identifiable after respective binding. Which is due to the differences of the two target proteins for both Affimer variants.

5.3.2 Non-Target Binding

To test the Affimer system, and as a control to see if IgG had as large an effect on non-IgG binding Affimers, IgG was added as a target solution to both the K67C and G65C Affimer variants. Both these Affimers are GST specific binders, and therefore should not bind any IgG at all.

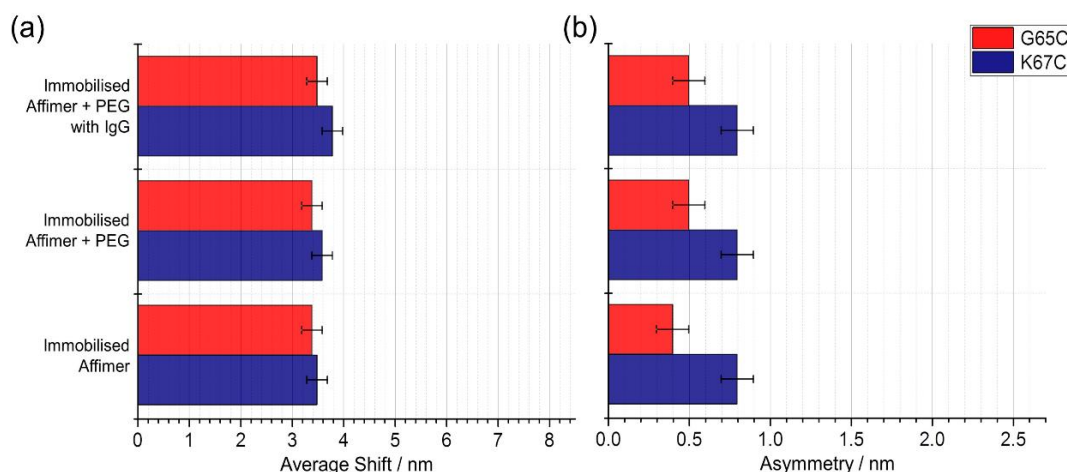


Figure 5.04 Bar charts showing (a) average shift, and (b) asymmetry for immobilised Affimer, addition of PEG filler, and addition of IgG target solution for GST binders, K67C (blue) and G65C (red), all relative to initial buffer measurements. The error bars represent the standard error calculated from 8 spectra measurements.

Figure 5.04 shows the average shift, and asymmetry values for both GST binding Affimers (K67C and G65C) after immobilisation on the surface, addition of PEG filler,

and after the addition of the IgG target solution which is then rinsed with buffer. As expected, since both of these Affimers should not bind IgG at all due to their high affinity and selectivity for GST, there is no change in the $\Delta\Delta S$ values after exposure to the IgG solution. There are also no changes, within error, to the average shift values meaning that the IgG from the target solution does not adsorb on the substrate surface, due to it already being filled with the Affimers, and PEG filler. This shows that the changes seen in Figure 5.03, after the addition of the target solution to the immobilised Affimer surface, is due to the Affimer specifically binding the protein and not due to any other factors, such as the protein itself becoming immobilised on the nanostructure surface.

5.3.3 Affimer Modelling

To further test, and gain a fuller understanding of the behaviour of the chiral nanostructures in the presence of these Affimer proteins, the reflectance spectra were modelled using a classical model to describe the plasmonic induced transparency.

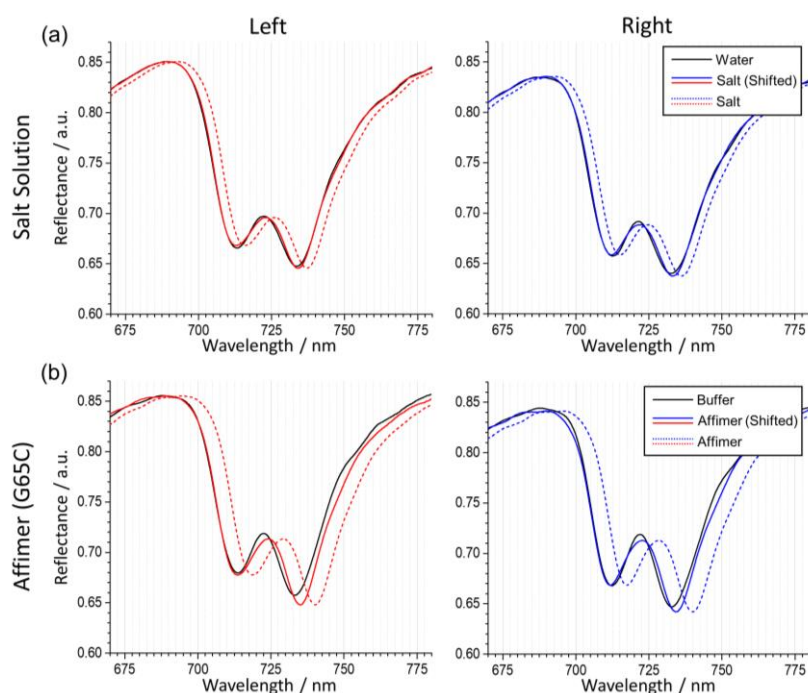


Figure 5.05 Graphs showing (a) reflectance spectra for water (black), and salt solution (dashed coloured) for both left- and right-handed shuriken structures, and (b) reflectance spectra for buffer (black) and, the adsorbed G65C Affimer (dashed coloured) for both handedness of shuriken structures. To aid comparison, both salt solution and Affimer spectra have been shifted (solid coloured) to overlap the initial water/buffer spectra.

This model used to replicate the reflectance spectra, was described in chapters 2 and 3, and is based on two coupled oscillators with variations of this approach having previously been reported [6, 7].

In Figure 5.05, salt solution spectra and Affimer spectra with similar refractive index shifts, relative to water/buffer, were compared for left- and right-handed shuriken structures. From this figure, it can be seen that, while the salt solution produces no significant change in the shape of the reflectance spectra relative to the water spectra, the adsorbed Affimer does produce a noticeable change in the shape relative to buffer in Figure 5.05(b). As this change in shape only happens for the adsorbed Affimer, and not for the achiral salt solutions, the Affimer is not only causing a shift due to the refractive index increase, but also affecting the reflectance properties of the left- and right-handed nanostructures. To measure these effects, the Affimer spectra for all three variants were modelled, as described and performed for the salt solutions data in chapter 3. However, only the data for the initial immobilisation of the Affimers were modelled, and not the spectra after the addition of the target protein.

Parameter	LH Buffer	LH K67C	RH Buffer	RH K67C	LH Buffer	LH G65C	RH Buffer	RH G65C	LH Buffer	LH H6C	RH Buffer	RH H6C
ω_r	728.8	729.9	728.1	729.3	725.2	727.3	722.7	725.7	728.0	729.4	726.3	728.0
ω_d	722.8	729.1	721.8	727.4	721.2	726.8	720.9	725.1	722.9	728.9	721.6	726.8
k	0.03125	0.03235	0.02965	0.03155	0.02890	0.03090	0.02675	0.02905	0.03060	0.03190	0.02875	0.03115
γ_r	0.0300	0.0300	0.0310	0.0310	0.0325	0.0325	0.0335	0.0335	0.0305	0.0305	0.0316	0.0316
γ_d	0.02950	0.02950	0.02805	0.02805	0.02645	0.02645	0.02515	0.02515	0.03125	0.03125	0.02845	0.02845
θ	-21.2	-24.7	-20.5	-25.0	-21.3	-25.5	-25.5	-28.0	-21.0	-25.0	-21.5	-23.9
ϕ	-26.5	-21.5	-27.5	-24.8	-26.1	-24.4	-28.1	-28.6	-26.8	-23.0	-27.9	-24.4
g	0.01605	0.01605	0.01600	0.01600	0.01755	0.01755	0.01720	0.01720	0.01632	0.01632	0.01580	0.01580
n_e	1.33	1.33	1.33	1.33	1.33	1.33	1.33	1.33	1.33	1.33	1.33	1.33
c_{Au}	0.1300	0.1300	0.1300	0.1300	0.1385	0.1385	0.1370	0.1370	0.1403	0.1403	0.1375	0.1375

Table 5.01 Model parameter values used to fit the left- and right-handed reflectance spectra for all three Affimer variant results.

Parameter	ΔLH K67C	ΔRH K67C	$\Delta \Delta x$ K67C	ΔLH G65C	ΔRH G65C	$\Delta \Delta x$ G65C	ΔLH H6C	ΔRH H6C	$\Delta \Delta x$ H6C
ω_r	1.1	1.2	0.1	2.1	3.0	0.9	1.4	1.7	0.3
ω_d	6.3	5.6	-0.7	5.6	4.2	-1.4	6.0	5.2	-0.8
k	0.0011	0.0019	0.0008	0.0020	0.0023	0.0003	0.0013	0.0024	0.0011
θ	-3.5	-4.5	-1.0	-4.2	-2.5	1.7	-4.0	-2.4	1.6
ϕ	5.0	2.7	-2.3	1.7	-0.5	-2.2	3.8	3.5	-0.3

Table 5.02 Asymmetry values for the five parameters used to fit the Affimer spectra; ω_r , ω_d , k , θ , and ϕ .

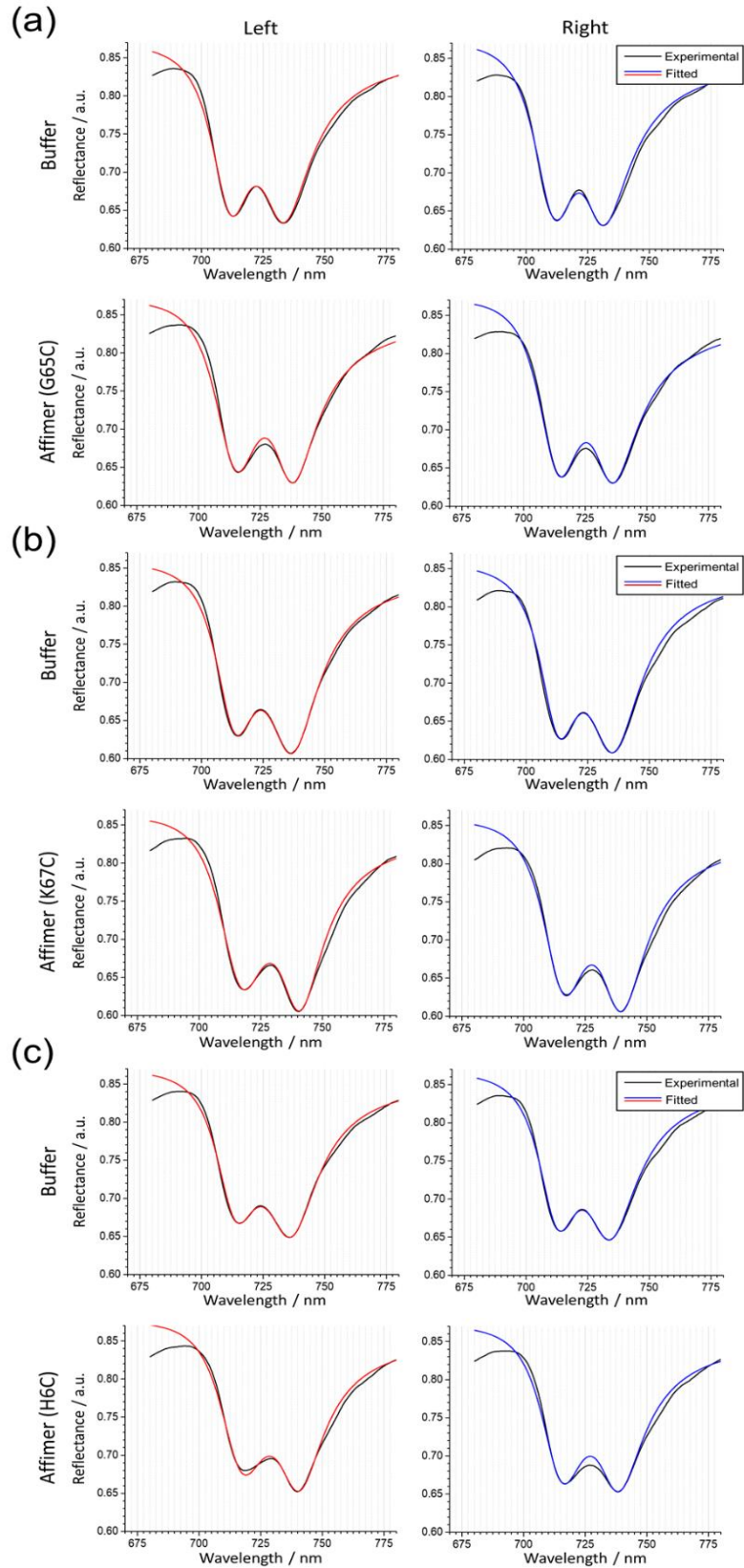


Figure 5.06 Graphs showing measured reflectance spectra (black), and fitted spectra (coloured) for buffer and Affimer measurements for (a) G65C, (b) K67C, and (c) H6C.

Figure 5.06 shows the fitted data directly overlapping the experimentally measured reflectance spectra for buffer, and all three of the Affimer variants, showing the quality of the fitting achieved. From the fitting spectra achieved for all three Affimers, G65C, K67C, and H6C, the fitting parameters are shown in Table 5.01. The differences observed in the fitting for ω_r , ω_d , k , θ , and ϕ are shown in Table 5.02, as well as the calculated asymmetry parameters for these quantities. With these asymmetry parameters being calculated as $\Delta\Delta x = {}^R\Delta x - {}^L\Delta x$, where $x = \omega_r, \omega_d, k, \theta, \text{ and } \phi$. For all three of the Affimer variants, in different orientations, all the asymmetry parameters possess a non-zero value. This shows that the presence of the Affimers on the metamaterial surface has a differential effect on the reflectance properties of both the left- and right-handed nanostructures. The asymmetry parameters calculated and arranged in Table 5.02, show all asymmetry values for all five parameters. However, to further understand the significance of these values, they were plotted as three separate bar charts in Figure 5.07. As well as $\Delta\Delta\lambda$ values, for all three Affimer variants, measured from the ORD spectra (Appendix D), as previously used in chapter 4. Figure 5.07(a) shows the $\Delta\Delta\lambda$ values for the Affimers, which are small and within experimental error of each other, emphasising the similarity between the structure of all three Affimer variants. Three bar charts relating to the modelled parameters were then plotted, the first containing the asymmetry values in phase, θ and ϕ , the second containing the asymmetry values for k , and the last graph displaying the asymmetry values for ω_r and ω_d calculated for all three Affimer variants. The asymmetry parameters calculated from the fitting data for k , ω_r , and ω_d are shown in Figure 5.07(c) and (d). For all three of the Affimer variants fitted, the values for these three parameters were all the same, within experimental error. Meaning, all three of the Affimer orientations were indistinguishable using these calculated fitting parameters. However, it is worthy to note that the asymmetry values for ω_r and ω_d have opposite signs to each other, with the latter values being roughly 1.5x larger than the ω_r values. In contrast to the obtained values for these three parameters, the asymmetry values in phase do differ significantly for each Affimer variant, as shown in Figure 5.07(b). As a result of these two phase parameters differing for each of the three Affimer variants, this provides a distinct fingerprint for the different Affimer orientations. Interestingly, when the cysteine residue was inserted into the β -turn 3 loop of the Affimer structure, the $\Delta\Delta\phi$ value is larger than $\Delta\Delta\theta$. However, this is reversed for the H6C Affimer, where the cysteine residue is inserted into the C-terminus strand.

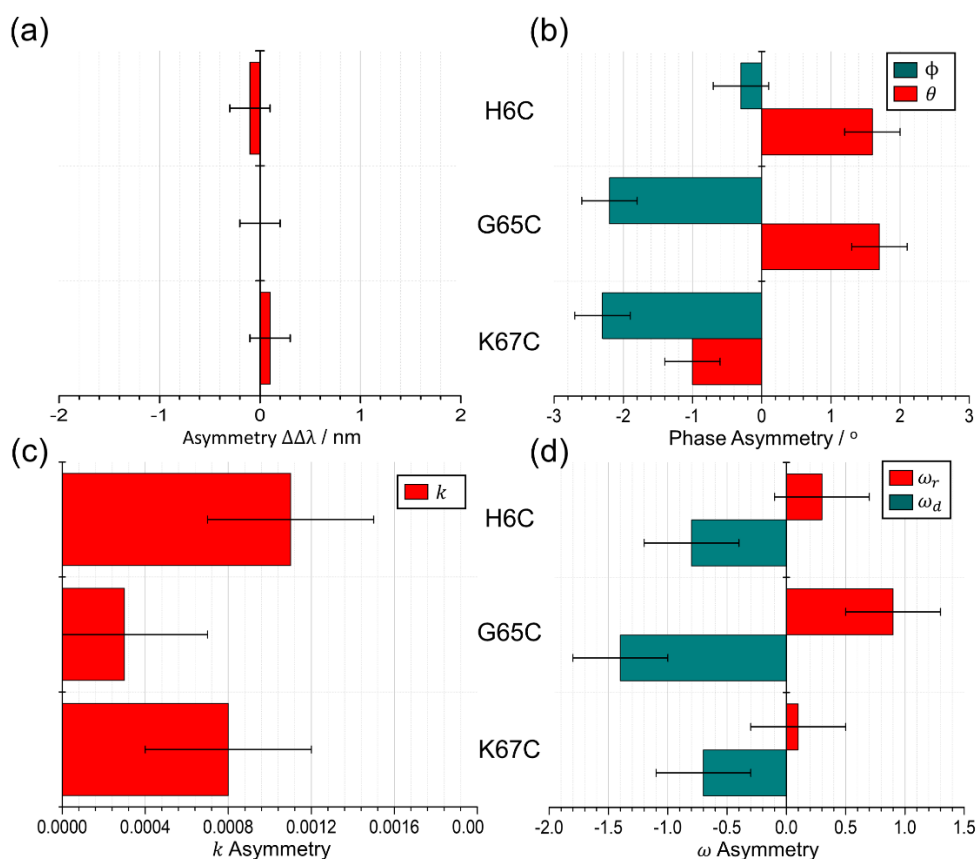


Figure 5.07 Bar graphs showing (a) $\Delta\Delta\lambda$ values from ORD spectra, (b) phase parameter (θ and ϕ) asymmetries, (c) coupling parameter (k) asymmetry, and (d) resonance frequency (ω_r and ω_d) asymmetries for all three Affimer variants. The error bars represent the standard error calculated from 8 spectra measurements.

5.3.4 Discussion

Two different interpretations of the reflectance data have been used throughout this chapter to determine the orientation differences of structurally similar Affimer proteins; the experimentally measured $\Delta\Delta S$ parameter, and the modelled retardation phase asymmetries, $\Delta\Delta\theta$ and $\Delta\Delta\phi$. The experimentally measured $\Delta\Delta S$ results, shown in Figure 5.03, show that this parameter can be used to distinguish between the different orientations of the same Affimer. Hence, even though the cysteine residue in G65C and K67C are only two positions in the sequence different, the two can easily be separated by the experimentally measured $\Delta\Delta S$ values. As the shape of the reflectance spectra is characteristic of plasmonic induced transparency, and is caused by the coupling of the optically bright dipolar and optically dark quadrupolar modes of the nanostructures (described in chapter 2). It has previously been shown, that any changes in the coupling between these two modes of the nanostructure

would have an effect on the shape and size of the reflectance spectra produced [8]. Due to the Affimer scaffold consisting of an α -helix, and anti-parallel β -sheet, the orientation of these secondary structure components can mediate the coupling between the two modes of the nanostructure. Since these secondary structure components are inherently chiral, the effect that the orientation of these structures has on the mediated coupling of the chiral nanostructures will be unequal for both the left- and right-handed shuriken structures. As the effect on each handedness of the nanostructure is asymmetrical, the induced changes in the reflectance spectra for both left- and right-handed structures will also be asymmetrical. Hence, with each of the Affimer variants being adsorbed to the surface with a different orientation, the separation effects in the two reflectance dips of the spectra for each handedness of structure will be unequal, resulting in the $\Delta\Delta S$ values observed in Figure 5.03.

In addition to this, the results shown in Figures 5.02 and 5.04 suggest that there are no significant structural perturbations of the Affimer upon immobilisation to the gold surface, with the surface stability of the Affimer protein scaffold being well documented [9, 10]. Previous studies using the quartz crystal microbalance (QCM) have shown that if there are any significant structural changes to the Affimer scaffold upon adsorption to the gold surface, then a loss of affinity and specificity for the target protein would occur [11]. However, from the results shown in Figure 5.02, it can be seen that there are substantial average shifts when the target protein binds to the respective Affimer, with H6C experiencing a shift of 3.8 nm upon IgG binding, and both G65C and K67C experiencing an average shift of 0.9 nm when exposed to GST. When the GST binding Affimers were exposed to IgG, in Figure 5.04, there was no measurable binding of the protein, resulting in no average shift or $\Delta\Delta S$ response. These results are in agreement with the high binding affinities of the Affimers to their target proteins observed in previous studies immobilised using the same method [12], and was indicative of a lack of perturbation to the secondary and tertiary structure of the Affimer.

Two significant differences between EIT in atomic systems, and plasmonic induced transparency are; coupling is achieved via nearfields for plasmonic induced transparency, and retardation effects become significant since the dimensions of the nanostructures used become comparable to the wavelength of light. Retardation is the effect of the phase difference between fields propagating from spatially separated regions of a nanostructure, giving rise to phase changes in the excited plasmon modes [13-15]. Since the chiral nanostructures can be shown to produce spatially varying superchiral fields (chapter 3), the sensitivity of the phase retardation effects,

shown in Figure 5.07(b), arise from the differential interaction of the superchiral near fields with a chiral dielectric. To validate that the changes seen in the phase retardation parameter in the reflectance spectra, result from the adsorption of the Affimer proteins, numerical EM simulations were performed. A 20 nm thick isotropic chiral dielectric layer covering the shuriken structures was simulated. The chiral dielectric layer was modelled based on the constitutive equations for an isotropic dielectric medium, previously reported, given by:

$$\mathbf{D} = \varepsilon_0 \varepsilon_r \mathbf{E} + i\xi \mathbf{B} \quad (5.3.1)$$

$$\mathbf{H} = \mathbf{B}/\mu + i\xi \mathbf{E} \quad (5.3.2)$$

Here, ε_0 is the permittivity of free space, ε_r is the relative permittivity, μ is the permeability, \mathbf{B} is the complex magnetic flux density, \mathbf{H} , \mathbf{E} and \mathbf{D} are the complex magnetic field, electric field and electric displacement field respectively, and ξ is a local parameter describing the chiral property of a molecular layer. Since ξ is a chiral descriptor, it only becomes a non-zero value for a chiral dielectric. Following a procedure previously described in the literature [16, 17], it can be calculated that for a protein layer, the parameter $\xi \approx 5 \times 10^{-4}$ for a wavelength of 700 nm. The simulation results are shown in Figure 5.08, and show the reflectance spectra for a chiral shuriken structure covered with water, and both the left- and right-handed shuriken structures covered with the chiral dielectric layer.

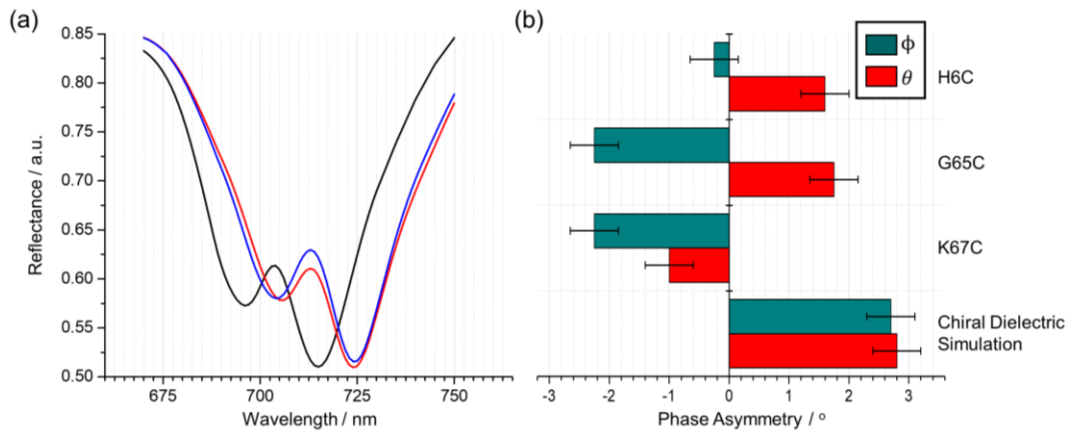


Figure 5.08 (a) Reflectance spectra from simulation with chiral dielectric covered left- (red) and right-handed (blue) shuriken nanostructures, as well as water covered shuriken structure (black), and (b) asymmetry in phase parameters for the simulated chiral dielectric layer compared with the three Affimer samples. The error bars represent the standard error calculated from 8 spectra measurements.

These results clearly demonstrate changes in the reflectance spectra when a chiral dielectric was added. The simulated reflectance spectra were also fitted with the coupled oscillator model, used previously, to extract the phase parameters, with all the modelled values for the simulated data shown in Appendix D. From Figure 5.08(b), an asymmetry in the phase parameters, θ and ϕ , is observed from the left- and right-handed structures, which is comparable in size to that observed in the experimental data. However, these simulations are not an exact reproduction of the experimentally observed changes, and are intended only as a proof of principle, since the Affimer layers are not isotropic in nature. Hence, the orientation and physical coverage of the Affimer layer cannot be replicated in a simulated environment. Even so, the simulations involving the isotropic chiral dielectric in Figure 5.08(a), still provide validation that the phase retardation of the chiral plasmonic resonators are dependent on the chirality of the surrounding dielectric.

The two main secondary structure protein motifs, α -helix and β -sheet, both differ in their dipole moments. The α -helix structure possesses a significant net dipole, which arises from the cumulative effect of the dipole moment of each amino acid backbone unit [18]. This is due to the peptide units in the α -helix all being aligned in the same orientation along the helical axis, resulting in the dipole moments also being aligned along this axis with a partial positive charge at the amino end, and a partial negative charge at the carboxy end. However, β -sheets are made up of β -strands that are aligned adjacent to each other, either parallel or anti-parallel. The anti-parallel β -sheet, that is present for the Affimer, is made up by the amino acids in adjacent strands having alternating directions [19]. This means, as the β -strands are aligned in opposite directions, the dipole moments of each strand are also in opposing directions, causing a negligible dipole moment, but would have quadrupolar or higher multipole moments. Since the Affimer structures contain a high anti-parallel β -sheet content ($\sim 55\%$), and the anisotropic nature of the Affimer layer is important due to the higher order contributions to optical activity, which cannot be replicated in the simulated environment, it can be speculated that the experimentally observed orientation dependency of the phase asymmetries, are due to these higher order moments.

5.4 Conclusion

In this chapter, we have introduced a new spectroscopic phenomenon to discriminate between protein fragments, which are structurally similar but immobilised on the gold nanostructures with differing orientations. The experimental asymmetry parameter, $\Delta\Delta S$, extracted from the reflectance spectra measured for both left- and right-handed chiral shuriken structures, was shown to be sensitive to the orientation of these exemplar Affimer systems. However, two of the Affimer variants (K67C and H6C) both produced a similar response, which could then only be separated after the addition of the respective target binding proteins.

By introducing a simple coupled oscillator model, described in chapters 2 and 3, the experimental reflectance spectra were modelled, and any retardation phase shifts extracted. These retardation phase shift asymmetries, $\Delta\Delta\theta$ and $\Delta\Delta\phi$, were then demonstrated to be sensitive to the differences in the immobilised orientation of the Affimers (Figure 5.07(b)). With these asymmetries in the retardation phase changes resulting from the differential interaction of the left- and right-handed chiral near fields of the structure with the chiral dielectric. When these results are compared with the asymmetry parameter ($\Delta\Delta\lambda$) introduced in the previous chapter, the results observed for $\Delta\Delta\lambda$ are all small and within the experimental error for all three immobilised orientations of the Affimer proteins. This inability of the previously used $\Delta\Delta\lambda$ parameter to detect the small differences between the immobilised Affimer layers, shows the greater incisiveness of the phase asymmetries to the orientation of the surface bound proteins. This represents a new source of retardation effects that can be induced through the dielectric properties of the surrounding environment, which has previously been attributed solely to size/geometry effects of the nanostructures [14, 20].

In summary, we have demonstrated that exemplar proteins which have similar structures, and only differ by a single amino acid (G65C and K67C), can be distinguished from each other using the phase retardation fingerprints introduced throughout this chapter. The results presented here are a more sensitive probe to the geometric structure of protein layers than previous applications of chiral plasmonic fields. Which have only been able to discriminate between proteins with significantly different secondary structure [21]. This phenomenon is a valuable addition to current bioanalytical methods, as it provides a unique way to rapidly obtain a simple fingerprint of interfacial structure that would otherwise not be possible.

5.5 References

1. Cha, T., A. Guo, and X.-Y. Zhu, *Enzymatic activity on a chip: The critical role of protein orientation*. *Proteomics*, 2005. **5**(2): p. 416-419.
2. Peluso, P., et al., *Optimizing antibody immobilization strategies for the construction of protein microarrays*. *Analytical Biochemistry*, 2003. **312**(2): p. 113-124.
3. Hendry, E., et al., *Chiral electromagnetic fields generated by arrays of nanoslits*. *Nano Letters*, 2012. **12**(7): p. 3640-3644.
4. Škrlec, K., B. Štrukelj, and A. Berlec, *Non-immunoglobulin scaffolds: a focus on their targets*. *Trends in biotechnology*, 2015. **33**(7): p. 408-418.
5. Ferrigno, P.K., *Non-antibody protein-based biosensors*. *Essays in biochemistry*, 2016. **60**(1): p. 19-25.
6. Zhang, S., et al., *Plasmon-induced transparency in metamaterials*. *Physical Review Letters*, 2008. **101**(4): p. 047401.
7. Tassin, P., et al., *Electromagnetically Induced Transparency and Absorption in Metamaterials: The Radiating Two-Oscillator Model and Its Experimental Confirmation*. *Physical Review Letters*, 2012. **109**(18): p. 187401.
8. Liu, N., et al., *Planar Metamaterial Analogue of Electromagnetically Induced Transparency for Plasmonic Sensing*. *Nano Letters*, 2010. **10**(4): p. 1103-1107.
9. Woodman, R., et al., *Design and validation of a neutral protein scaffold for the presentation of peptide aptamers*. *Journal of Molecular Biology*, 2005. **352**(5): p. 1118-1133.
10. Hoffmann, T., et al., *Structure-function studies of an engineered scaffold protein derived from stefin A. I: Development of the SQM variant*. *Protein Engineering, Design & Selection*, 2010. **23**(5): p. 403-413.
11. Weckman, N.E., et al., *Comparison of the specificity and affinity of surface immobilised Affimer binders using the quartz crystal microbalance*. *Analyst*, 2016. **141**(22): p. 6278-6286.
12. Estrela, P., et al., *Potentiometric detection of protein interactions with peptide aptamers*. *IEEE Sensors Proceedings*, 2008: p. 646-649.
13. Maier, S.A., *Plasmonics: fundamentals and applications*. 2007: Springer Science & Business Media.
14. Davis, T.J., K.C. Vernon, and D.E. Gómez, *Effect of retardation on localized surface plasmon resonances in a metallic nanorod*. *Optics Express*, 2009. **17**(26): p. 23655-23663.
15. Davis, T. and D. Gómez, *Colloquium: An algebraic model of localized surface plasmons and their interactions*. *Reviews of Modern Physics*, 2017. **89**(1): p. 011003.
16. Govorov, A.O. and Z. Fan, *Theory of chiral plasmonic nanostructures comprising metal nanocrystals and chiral molecular media*. *ChemPhysChem*, 2012. **13**(10): p. 2551-2560.
17. Abdulrahman, N.A., et al., *Induced chirality through electromagnetic coupling between chiral molecular layers and plasmonic nanostructures*. *Nano Letters*, 2012. **12**(2): p. 977-983.

18. Baker, E.G., et al., *Local and macroscopic electrostatic interactions in single α -helices*. Nature Chemical Biology, 2015. **11**(3): p. 221-228.
19. Branden, C.I., *Introduction to protein structure*. 1999: Garland Science.
20. Valev, V.K., et al., *Chirality and chiroptical effects in plasmonic nanostructures: fundamentals, recent progress, and outlook*. Advanced Materials, 2013. **25**(18): p. 2517-2534.
21. Hendry, E., et al., *Ultrasensitive detection and characterization of biomolecules using superchiral fields*. Nature nanotechnology, 2010. **5**(11): p. 783-787.

Chapter 6: Characterisation of Surface Orientation and Ligand Induced Conformational Changes for Heat Shock Protein 90

6.1 Introduction

High-throughput studies, and characterisation of target molecule binding to proteins is important for the discovery of effective drug targets. Current methods of determining protein-target interactions include; X-ray crystallography [1], nuclear magnetic resonance (NMR) [2], and label based fluorescence spectroscopy [3]. However, these methods are time consuming, and require a lot of material to work with. The labels required for fluorescence spectroscopy also often sterically hinder the molecular binding interactions with the protein, and leads to errors in the measurements [4]. This leads to the requirement for high-throughput label-free methods for the detection and characterisation of protein-target molecule interactions.

In this chapter, we will use the phenomena introduced in the previous chapter; both the asymmetry parameter ($\Delta\Delta S$), and the retardation phase asymmetries ($\Delta\Delta\theta$ and $\Delta\Delta\phi$) extracted from the reflectance spectra, to detect protein conformational changes upon binding of an inhibitor molecule. The protein, Heat Shock Protein 90 (HSP90), a therapeutic target for anti-cancer drugs, was immobilised on the chiral nanostructured surface with two differing orientations. The HSP90 inhibitor, 17-AAG, was used to bind to the surface immobilised protein, and induce an irreversible conformational change. We will show how we can detect the two different binding orientations of the immobilised protein, and then how the differing orientations of the HSP90 affect the sensitivity of the ligand induced conformational changes that can be detected.

By modelling the spectra in the same way as described previously, we will show that the retardation phase shifts, $\Delta\Delta\theta$ and $\Delta\Delta\phi$, are not only sensitive to the orientations of the adsorbed protein molecule, demonstrated in the previous chapter, but are also sensitive to the ligand induced conformational changes. These phase shift parameters are in close agreement with the experimentally measured $\Delta\Delta S$ parameter for both protein orientations. Showing that both these phenomena are incisive probes into determining the ligand induced binding effects, especially when the protein is immobilised with an optimum orientation, and would be a powerful tool for high-throughput drug discovery.

6.2 Heat Shock Protein 90 (HSP90)

Heat shock protein 90 (HSP90) is one of the most abundant molecular chaperone proteins, which as a family, account for 1-2% of all cellular proteins in most cells [5]. The molecular chaperone HSP90, named as it protects cells from stress and is a 90 kDa sized protein, stabilises and activates more than 200 proteins which are often referred to as HSP90 'clients'. Many cancer cells can use the HSP90 protein to protect an array of mutated or overexpressed cancer associated proteins from misfolding or degradation [6]. Therefore, HSP90 has been recognised as a crucial facilitator of cancer cell survival, and as a result has become a significant therapeutic target for cancer drug treatment [7]. The structure of HSP90 is a homodimer, with each protomer containing three flexibly linked regions; an N-terminal domain, a middle domain, and a C-terminal domain [8]. The homodimer, in its apo (open) state, adopts a V shaped structure, as shown in Figure 6.01(a). HSP90 is a weak ATPase, leading to induced conformational changes upon ATP binding. When ATP binds to HSP90, a series of conformational changes occur. The first intermediate is reached after initial ATP binding, where the ATP lids in the N-domains close over, but the domains still remain open in the V shaped conformation. The second intermediate is then reached, where the N-terminal dimerise, with the middle domains repositioning, shown in Figure 6.01(b). The HSP90 then reaches its fully closed structure, shown in Figure 6.01(c), which is when the ATP is hydrolysed. After the hydrolysis of ATP, the N-domains dissociate and release the ADP, before returning back to the initial open conformation [9, 10].

Many therapeutic inhibitor molecules have been developed since HSP90 was identified as a target for cancer therapy, with one of the most prominent being the natural product, Geldanamycin. Part of the Ansamycin family, it binds to the ATP-binding site of the N-terminal domain in HSP90, and disrupts the ATPase activity [11]. However, Geldanamycin is too toxic in treating patients directly. Therefore, derivatives of Geldanamycin have gained interest as a therapeutic inhibitor, with the 17-allylamine derivative, 17-allylamino-17-demethoxygeldanamycin (17-AAG), being at the forefront of current research. Which has resulted in 17-AAG being the subject of multiple clinical trials [12]. 17-AAG is a small molecular inhibitor of HSP90 that inhibits the binding of HSP90 to client proteins by directly binding to the ATP/ADP binding pocket. When the inhibitors bind to the ATP/ADP binding pocket, the protein seems to mimic the ADP bound fully closed state, as shown in Figure 6.01(c). 17-AAG has been shown previously to bind to purified HSP90 with a micromolar affinity, causing the full closure of the HSP90 protein described [13-15].

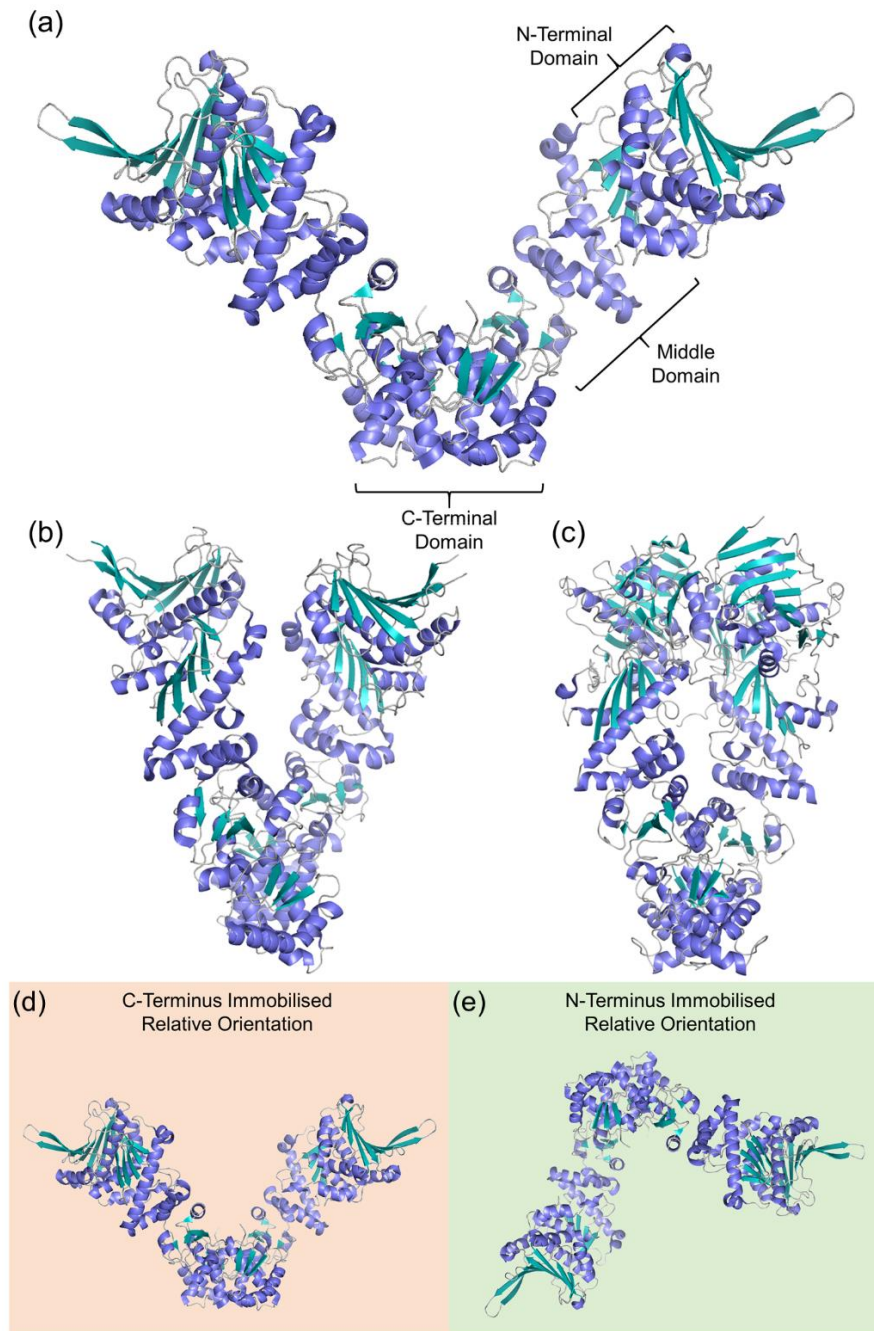


Figure 6.01 Heat shock protein 90 dimers in (a) the open form (PDB: 2IOQ), (b) partly closed ATP-bound form (Intermediate 2, PDB: 2O1V), and (c) closed ATP-bound form (PDB: 2CG9). (d) and (e) show the relative immobilised orientation of the HSP90 protein when His-tagged at the C-terminus and N-terminus domain respectively.

Figure 6.01 shows the three major conformations that occur upon HSP90 binding with ATP. First the open V shaped conformation, the intermediate partially closed ATP bound formation, and then finally the completely closed formation before releasing ADP and returning to the open conformation. The inhibitor, 17-AAG, binds to the

HSP90 protein inducing the full conformational closure, as shown in Figure 6.01(c). Two different variants of the HSP90 protein will be measured here, each with an identical structure but with the His-tag attached at a different position of the protein. The two variants have the His-tag attached at either the C-terminal domain, or on one of the N-terminal domains present within the protein. When the His-tag is attached to the C-terminal domain, the HSP90 is attached to the NTA monolayer with an orientation as shown in Figure 6.01(d). In this case, the C-terminal 'hinge' region is attached to the surface, through the His-tag, so that the N-terminal ATP binding domain is exposed to the solution, and the furthest part of the protein from the sample surface. The second variant, when the His-tag is attached to the N-terminal of the HSP90 protein, has the orientation of the protein reversed, shown in Figure 6.01(e). The N-terminal of one domain is attached to the nanostructure surface, through the His-tag, with the C-terminal now being furthest from the substrate surface. This means, that in the case of the N-terminal bound HSP90, the ATP binding site of one of the protomers is right next to the surface of the nanostructure.

6.3 Results and Discussion

6.3.1 Measurement of HSP90 and Ligand Addition

Having two versions of the HSP90 protein, with the His-tag at a different position for each, allows us to further test these phenomena for orientation effects of larger proteins, combined with the ligand induced conformational changes. The HSP90 protein was either His-tagged at the N-terminal or C-terminal domain, meaning that the protein would be attached to the nanostructure surface with two different orientations. The C-terminal domain attachment would be orientated with the 'hinge' domain attached to the surface, and the two ATP binding domains openly exposed away from the surface. Whereas, the N-terminal domain attachment is orientated with the 'hinge' domain furthest from the surface, and one of the ATP binding domains attached to the surface, with the other ATP binding domain in free space. For each of the HSP90 attachments, reflectance measurements were recorded after the immobilisation of the NTA/EG-thiol in the presence of buffer, as a reference. Then after the immobilisation of the HSP90 protein, and after the addition of each increasing concentration of the 17-AAG ligand.

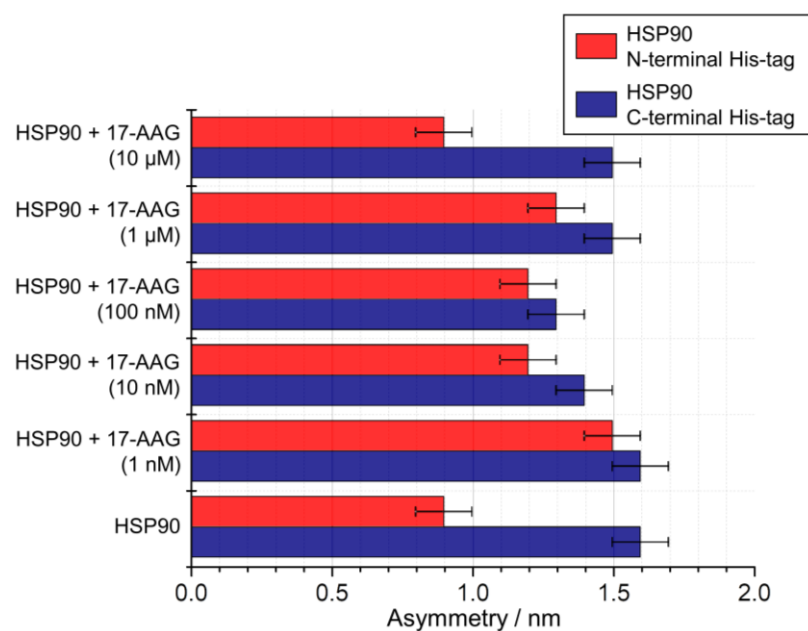


Figure 6.02 Bar chart showing the separation asymmetry parameter for HSP90 His-tagged at the C-terminal domain (blue) and at the N-terminal domain (red) for the initial immobilisation of the protein, and the addition of the 17-AAG ligand with increasing concentrations. The error bars represent the standard error calculated from 8 spectra measurements.

Figure 6.02 shows the separation asymmetry parameter, $\Delta\Delta S$, for the initial immobilisation of both variants of HSP90, C-terminus (blue) and N-terminus (red), and the asymmetry values measured when increasing concentrations of the 17-AAG ligand was added to each HSP90 orientation respectively. From these results, the two orientations of the immobilised HSP90 proteins can be easily separated by their $\Delta\Delta S$ value shown in Figure 6.02. For the HSP90 protein attached through a His-tag at the C-terminus domain, the $\Delta\Delta S$ value is almost twice as large as the value measured for the HSP90 protein attached by a His-tag on one of the N-terminal domains.

After the HSP90 proteins were immobilised onto the nanostructured surface, with the two different orientations, the 17-AAG ligand was introduced. Five different concentrations of 17-AAG solution were consecutively added to the immobilised HSP90. The smallest concentration introduced was 1 nM 17-AAG, increasing in one order of magnitude steps to a final concentration of 10 μM. The results in Figure 6.02 show that the two HSP90 orientations show different results for binding of the 17-AAG ligand at each respective concentration. For the lowest concentration, 1 nM solution of 17-AAG, there is no change produced in the asymmetry parameter for the C-terminus orientation of the protein. However, there is a larger increase in the asymmetry for the N-terminus immobilised protein upon addition of the low

concentration ligand solution. When the next three concentrations of 17-AAG were added (10 nM, 100 nM, and 1 μ M), both HSP90 orientations showed similar changes in the $\Delta\Delta S$ parameter response. With the 10 nM concentration producing a small decrease in asymmetry for both, albeit with the N-terminus variant showing a slightly larger decrease, and then the 100 nM and 1 μ M solutions having no effect on the asymmetry parameter within experimental error of the measurements. When the final 10 μ M ligand solution is added to the immobilised proteins, no change can be measured in the asymmetry parameter for the C-terminus HSP90. However, for the N-terminus variant of the protein, another relatively large decrease is the asymmetry parameter occurs relative to the previous solution.

6.3.2 Control Measurements

To confirm that the changes observed in the reflectance asymmetry parameter, $\Delta\Delta S$, are a result of the induced conformational changes upon HSP90 binding the 17-AAG ligand, DMSO solutions without the addition of the 17-AAG ligand were added to the immobilised protein layer. The solutions were made the same way as the inhibitor solution, by adding the respective volume of DMSO used to dissolve the 17-AAG ligand to buffer, to again create five solutions which were consecutively added to the immobilised protein. As the HSP90 attached to the surface through the N-terminal domain showed the largest changes, only this protein was measured with the DMSO test solutions. Hence, if no change was observed for this orientation it is highly likely that no change would also be detected for the C-terminal immobilised HSP90.

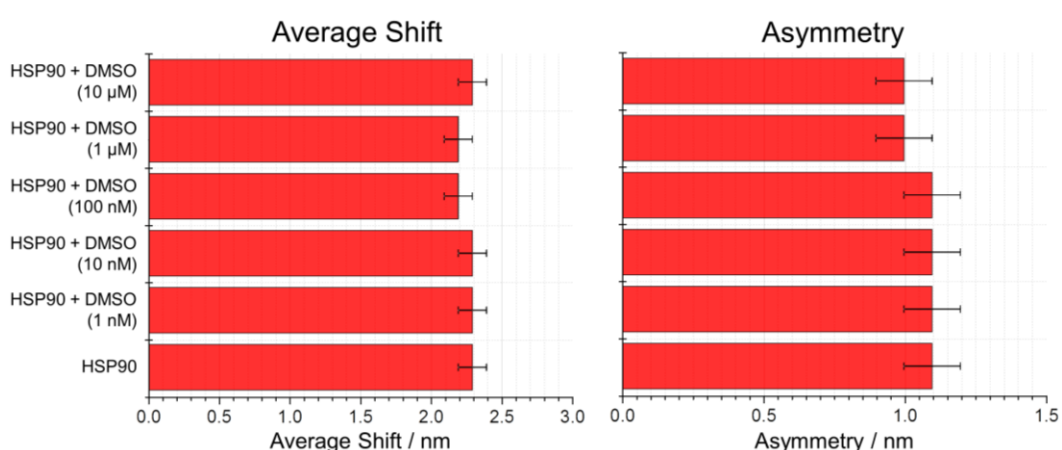


Figure 6.03 Average shift and separation asymmetry parameter ($\Delta\Delta S$) values for the N-terminal attached HSP90 protein with the addition of control DMSO solutions (no 17-AAG inhibitor). The error bars represent the standard error calculated from 8 spectra measurements.

Figure 6.03 shows the average shift values and asymmetry parameter values for the N-terminal immobilised HSP90 protein, and when increasing concentrations of DMSO solutions (with no 17-AAG inhibitor) were added to the protein. From this data, the DMSO solutions, containing no 17-AAG ligand, do not have any effect on the average shift or asymmetry parameter obtained from the HSP90 protein immobilised onto the gold nanostructure surface. Since there are no changes, outside of experimental error, when the DMSO solutions are added, we can conclude that all the changes observed for the measurements in Figure 6.02 are solely due to the conformational changes induced in the protein upon ligand binding.

6.3.3 HSP90 Modelling

As with the Affimer data, the HSP90 data shown here was also modelled using the coupled oscillator model in the same way as the previous chapter. With the retardation phase asymmetry, $\Delta\Delta\theta$ and $\Delta\Delta\phi$, values being plotted in Figure 6.04. These results are plotted for both the His-tagged versions of the HSP90 proteins, and the change observed for each ligand solution for both variants. The asymmetry values for the other three parameters, ω_r , ω_d and k , are also plotted in Figure 6.05.

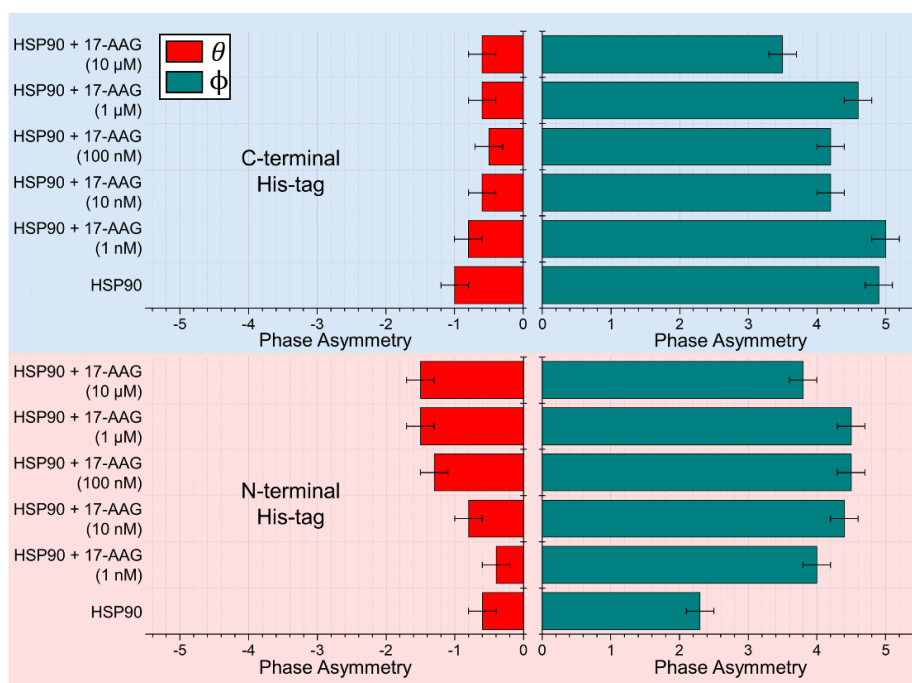


Figure 6.04 Bar graphs showing the asymmetry values of θ (red bars) and ϕ (green bars) for the C-terminal (blue background, top) and N-terminal (red background, bottom) attached HSP90 protein. The error bars represent the standard error calculated from 8 spectra measurements.

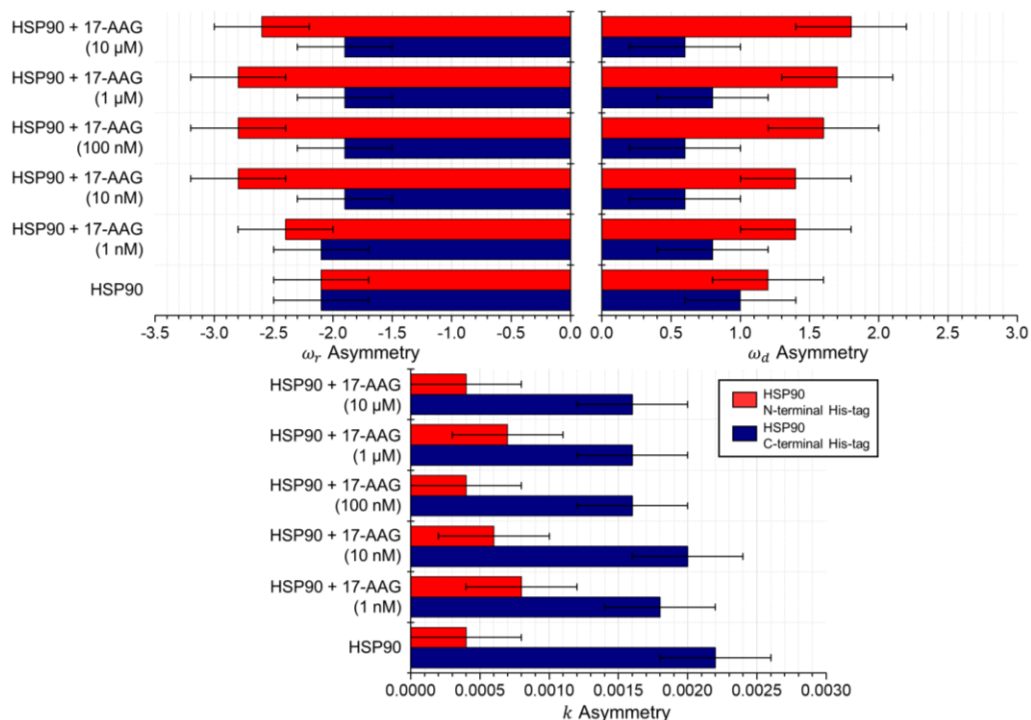


Figure 6.05 Bar graphs showing the asymmetries in the resonance frequencies (ω_r and ω_d), and coupling parameter (k) for the C-terminal (blue) and N-terminal (red) attached HSP90. The error bars represent the standard error calculated from 8 spectra measurements.

The results in Figure 6.04 show the asymmetry values obtained from the modelling for the two retardation phase values, θ and ϕ , for both the C- and N-terminal attached proteins. For the C-terminal attached HSP90, θ does not significantly change throughout the addition of the increasing concentrations of ligand solution. However, the ϕ parameter follows a very similar trend to the experimental data in Figure 6.02, with one major difference. Where the data suggests that, in correspondence with the experimental data, the protein goes through an intermediate structure when the 10 nM and 100 nM ligand solutions are added to the immobilised protein. Although, contrary to the experimental data for the C-terminal attached protein, a large change occurs when the 10 μ M 17-AAG ligand solution is added. Which shows that although the full closure of the immobilised protein cannot be detected in this orientation experimentally, by modelling the recorded data it can easily be distinguished from the intermediate structure. For the N-terminal attached HSP90, which is the version of the protein attached through one of the ATP binding domains, the modelled data again compliments the experimentally measured asymmetries. The θ parameter again shows insignificant changes, with only small changes upon binding of the 17-AAG. However, the ϕ changes show much larger differences for this orientation of

HSP90. Comparable to the experimental data, the initial ϕ value for immobilising the N-terminal attached HSP90 onto the nanostructure surface is much smaller than immobilising the C-terminal attached protein. When the smallest concentration ligand solution, 1 nM, is added to the N-terminal attached HSP90, a significantly large increase occurs when compared to the initial value of the immobilised protein. This agrees with the experimental data once again, and further suggests that at low concentrations, the ligand binds to the HPS90 causing a closure of the ATP lid without bringing together the arms of the protein. Then for the 10 nM, 100 nM, and 1 μ M solutions with the N-terminal attached protein, there are small changes in the ϕ asymmetry as it passes through the intermediate structure seen in Figure 6.01(b). Then finally, as seen in Figure 6.02 for the experimental data, there is a significant decrease in the ϕ asymmetry when the 10 μ M solution is added and the coming together of the two N-terminal domains leads to the full closure of the two arms.

For the three parameters in Figure 6.05, ω_r , ω_d and k , the values obtained upon modelling the addition of the ligand solutions to each HSP90 orientation are the same, within experimental error, of the initial protein value. This is the same for both the C-terminal, and N-terminal His-tagged proteins. Therefore, similar to the Affimer orientation detection, no ligand binding induced conformational changes could be determined from the modelling of the ω_r , ω_d , and k parameters. The numerical values used for each parameter in the model are shown in Appendix E.

6.3.4 Discussion

To characterise the conformational changes induced by ligand binding upon the HSP90 protein, immobilised with two different orientations, two interpretations of the reflectance data were again used here, in parallel with the previous chapter. The experimentally measured $\Delta\Delta S$ parameter, and the modelled retardation phase asymmetries, $\Delta\Delta\theta$ and $\Delta\Delta\phi$. The experimentally measured results for $\Delta\Delta S$, shown in Figure 6.02, show that there is a considerably larger asymmetry for the C-terminal immobilised protein than for the N-terminal immobilised HSP90. This is a result of the orientation with which the proteins are immobilised, shown in Figure 6.01(d) and (e). For the HSP90 with the C-terminus His-tag, the protein is bound through the C-terminus domain, which acts as a 'hinge' for bringing the two 'arms' of the protein together, with the two arms of the protein being orientated in similar directions, Figure 6.01(d). This orientates the two middle and N-terminal domains of the HSP90 structure in a similar fashion, and can be theorised to create a larger contribution to

the asymmetry, as the secondary structure of each 'arm' is orientated in a similar fashion. In contrast, the N-terminus attached HSP90, attached through a His-tag at the N-terminal domain on one of the HSP90 arms, has both arms of the protein orientated very differently relative to the surface. With one arm being directly attached to the surface, through the His-tag, and the other arm being in free space, Figure 6.01(e). This means that both arms of the protein, relative to the nanostructure surface, will not have similar orientations. Hence, the secondary structure in each arm will not be orientated in the same direction, and will not collectively contribute to the asymmetry, leading to the smaller asymmetry value seen in Figure 6.02.

As reported previously from the literature, full closure of the HSP90 protein occurs with micromolar affinity for the chosen ligand, 17-AAG [11, 15, 16]. However, from the results shown in Figure 6.02, it can be seen that there are small changes induced in the HSP90 structure, even at much lower ligand concentrations. This is particularly observed in the N-terminal variant of the HSP90 protein. This shows that smaller changes to the HSP90 protein, caused by the addition of low nanomolar concentrations of 17-AAG, can be detected when the protein is attached to the surface through the N-terminal domain, than through C-terminal domain attachment. This is due to the ATP binding site being within the N-terminal domain, so when the protein is immobilised on the surface through the N-terminal end, the ATP binding site is closer to the surface of the nanostructures. However, when the protein is attached through the C-terminal end, the ATP binding sites are the furthest part of the protein from the structured surface. Therefore, even by having only one of the N-terminal domains of the protein attached to the surface, the effect any change in this site has on the superchiral fields around the nanostructure is larger than when the binding sites are an extended distance from the surface, as in the C-terminal attachment of HSP90. This change caused, by the introduction of the 1 nM ligand solution, is most likely inducing the closure of the ATP binding lid in the N-terminal domain, with no large change in the quaternary structure of the protein [9, 10]. Hence, no detectable change for the HSP90 protein attached through the C-terminal domain. When the 10 nM and 100 nM solutions of 17-AAG are added to both the attached proteins, it can be theorised that some small changes are occurring with the protein possibly going through an intermediate conformation such as that shown in Figure 6.01(b). However, when the larger concentration solutions of the ligand are added, there is a small increase in the asymmetry for the C-terminal attached protein with 1 μ M 17-AAG, but the largest change is for the N-terminal attached protein after the addition of the 10 μ M ligand solution. The change caused for the C-terminal attached

protein with the 1 μM solution of 17-AAG, could be the change from the intermediate structure to the fully closed structure, but the changes measured in the asymmetry parameter are too small to say this with certainty. When the 10 μM ligand solution is added to the N-terminal attached HSP90 however, the asymmetry decrease is much larger due to the protein conformation becoming the fully closed structure shown in Figure 6.01(c). This larger change for the HSP90 attached to the surface through the N-terminal domain is theorised to be due to the two arms of the protein fully closing, bringing the two opposite N-terminal domains together and aligning the secondary structure of each arm relative to the surface. The changes caused for the protein attached through the C-terminal domain are consistently smaller due to the fact that the protein is attached through the hinge domain, resulting in the two arms of HSP90 behaving almost symmetrically upon ligand binding.

Consistent with the experimentally measured parameter, $\Delta\Delta S$, the two different immobilised variants of the HSP90 protein can be easily distinguished using the modelled phase parameters, $\Delta\Delta\theta$ and $\Delta\Delta\phi$. With again, the retardation phase parameter $\Delta\Delta\phi$ being twice as large for the HSP90 protein immobilised at the C-terminal end, than for the N-terminal immobilised version. When the addition of the 17-AAG ligand solutions were modelled using the same method, the $\Delta\Delta\phi$ parameter shows a similar trend to the experimentally measured $\Delta\Delta S$ parameters. With the N-terminal immobilised variant of the protein, two significant binding event can be seen. The initial binding of the 17-AAG with the 1 nM solution, attributed to the closure of the ATP-lid in the N-terminal domain, and the full conformational closure of the two protein arms with the 10 μM ligand solution. Small increases in the $\Delta\Delta\phi$ parameter can also be seen with the ligand solutions between these two concentrations, signifying the intermediate structure (Figure 6.01(b)) before the full closure of the protein. When the C-terminal immobilised variant of the HSP90 protein is modelled, the $\Delta\Delta\phi$ parameter once again follows the same trend as the experimental $\Delta\Delta S$ values. Where the initial binding of the 17-AAG ligand cannot be detected at the 1 nM concentration, but the intermediate structure can be observed for increasing ligand concentrations of 10 nM, 100 nM, and 1 μM . However, in contrast to the experimentally measured $\Delta\Delta S$ parameter, the final coming together of the two arms of the protein can be observed, with a significant decrease in the $\Delta\Delta\phi$ value.

In both the experimental and modelled results, the initial immobilised orientation of the HSP90 protein can be easily distinguished, with the C-terminal attached protein producing a response nearly twice the magnitude of the N-terminal, in both $\Delta\Delta S$ and $\Delta\Delta\phi$. The intermediate structure, can also be seen for both immobilised variants of

the protein, with the final conformational closure also being observed in the $\Delta\Delta\phi$ values for both attachments. However, in both the $\Delta\Delta S$ and $\Delta\Delta\phi$ interpretations of the data, only the initial binding of the 17-AAG from the 1 nM solution could be observed for the N-terminal attached protein. This is due to the binding site of the 17-AAG being located in the N-terminal domain of the HSP90 structure, which results in the closure of the ATP binding lid upon ligand addition. As the superchiral fields only extend a limited distance from the nanostructure surface, and are much more intense nearer the nanostructure, the closer to the surface the binding event or conformational change occurs then the more sensitive to this the structures will be. Hence, when the protein is immobilised through the N-terminal domain, the binding site of the 17-AAG is directly above the nanostructured surface, leading to the detection of the ATP-lid closure. However, in the C-terminal attached HSP90 protein, the N-terminal domain is located a significant distance away from the nanostructure surface (Figure 6.01(d)), resulting in the loss of sensitivity to the initial ligand binding event.

6.4 Conclusion

In this chapter, we have utilised the phenomena introduced in the previous chapter to discriminate between two surface bound orientations of the HSP90 protein, and detect the conformational changes induced upon ligand binding to the immobilised proteins. By initially immobilising the protein on the nanostructured surface with two opposite orientations, we can see how the orientation of the HSP90 can affect the sensitivity achieved for the protein-ligand interactions. With the protein initially binding the inhibitor, 17-AAG, before passing through an intermediate structure (Figure 6.01(b)), to reach the fully closed conformation shown in Figure 6.01(c) [17].

Both the experimentally measured $\Delta\Delta S$ parameter, and the modelled retardation phase parameters, introduced in the previous chapter, show the same trends for both immobilised HSP90 variants. With the two different immobilised orientations being easily distinguishable. However, for the C-terminal immobilised HSP90 the fully closed conformation of the protein was only detected through the modelled phase parameter and not the experimental $\Delta\Delta S$ parameter. Which again suggests the greater incisiveness of the phase retardation asymmetries to not only the orientations of surface immobilised protein molecules, but also to any conformational changes that occur within the immobilised structure. In contrast to the C-terminal domain attached HSP90, the results in both $\Delta\Delta S$ and the phase asymmetries for the protein immobilised through the N-terminal domain show an initial ligand binding event

occurring for the lowest concentration ligand solution of 1 nM. This can only be observed for the N-terminal variant of the HSP90 protein, as the ligand binding occurs at the nanostructure surface, where the superchiral field intensity is strongest. Resulting in a higher sensitivity to small changes, such as the ATP-lid closure in the N-domain of HSP90, than would be detected at a larger distance from the nanostructure surface.

In summary, we have shown here, that by using the same chiral nanostructures described throughout this thesis, that the orientation of an immobilised protein on the surface of the structures can increase the sensitivity of this phenomena to protein-ligand interactions. Although the experimental and modelled parameters do show an agreement throughout, the modelled parameter $\Delta\Delta\phi$ shows a greater incisiveness to the conformational changes produced upon ligand binding to the HSP90 protein. A greater sensitivity to the initial binding of the ligand, 17-AAG, was also achieved through controlling the immobilisation orientation of the protein. Hence, we have shown here that the sensitivity of this phenomenon to protein-ligand interactions, and conformational changes, can be increased through the immobilisation orientation of the protein. Enabling us to detect even very small changes within the protein structure, that would otherwise be a very difficult and arduous measurement.

6.5 References

1. Nienaber, V.L., et al., *Discovering novel ligands for macromolecules using X-ray crystallographic screening*. Nature Biotechnology, 2000. **18**(10): p. 1105-1108.
2. Pellecchia, M., et al., *Perspectives on NMR in drug discovery: a technique comes of age*. Nature Reviews Drug Discovery, 2008. **7**(9): p. 738-745.
3. Loving, G.S., M. Sainlos, and B. Imperiali, *Monitoring protein interactions and dynamics with solvatochromic fluorophores*. Trends in Biotechnology, 2010. **28**(2): p. 73-83.
4. Zhang, L., T. Hurek, and B. Reinhold-Hurek, *Position of the fluorescent label is a crucial factor determining signal intensity in microarray hybridizations*. Nucleic Acids Research, 2005. **33**(19): p. e166-e166.
5. Csermely, P., et al., *The 90-kDa Molecular Chaperone Family: Structure, Function, and Clinical Applications. A Comprehensive Review*. Pharmacology & Therapeutics, 1998. **79**(2): p. 129-168.
6. Trepel, J., et al., *Targeting the dynamic HSP90 complex in cancer*. Nature Reviews Cancer, 2010. **10**(8): p. 537-549.
7. Neckers, L. and P. Workman, *Hsp90 molecular chaperone inhibitors: are we there yet?* Clinical Cancer Research, 2012. **18**(1): p. 64-76.
8. Beebe, K., et al., *Post-translational modification and conformational state of Heat Shock Protein 90 differentially affect binding of chemically diverse small molecule inhibitors*. Oncotarget, 2013. **4**(7): p. 1065.
9. Hessling, M., K. Richter, and J. Buchner, *Dissection of the ATP-induced conformational cycle of the molecular chaperone Hsp90*. Nature Structural & Molecular Biology, 2009. **16**(3): p. 287.
10. Li, J. and J. Buchner, *Structure, Function and Regulation of the Hsp90 Machinery*. Biomedical Journal, 2013. **36**(3): p. 106-106.
11. Roe, S.M., et al., *Structural basis for inhibition of the Hsp90 molecular chaperone by the antitumor antibiotics radicicol and geldanamycin*. Journal of Medicinal Chemistry, 1999. **42**(2): p. 260-266.
12. Sausville, E.A., J.E. Tomaszewski, and P. Ivy, *Clinical development of 17-allylamino, 17-demethoxygeldanamycin*. Current Cancer Drug Targets, 2003. **3**(5): p. 377-383.
13. Chiosis, G., et al., *A small molecule designed to bind to the adenine nucleotide pocket of Hsp90 causes Her2 degradation and the growth arrest and differentiation of breast cancer cells*. Chemistry & Biology, 2001. **8**(3): p. 289-299.
14. Kamal, A., et al., *A high-affinity conformation of Hsp90 confers tumour selectivity on Hsp90 inhibitors*. Nature, 2003. **425**(6956): p. 407-410.
15. Zhang, J., et al., *The heat shock protein 90 inhibitor 17-AAG suppresses growth and induces apoptosis in human cholangiocarcinoma cells*. Clinical and Experimental Medicine, 2013. **13**(4): p. 323-328.
16. Chiosis, G., et al., *17AAG: low target binding affinity and potent cell activity—finding an explanation1*. Molecular Cancer Therapeutics, 2003. **2**(2): p. 123-129.
17. Krukenberg, K.A., et al., *Multiple conformations of E. coli Hsp90 in solution: insights into the conformational dynamics of Hsp90*. Structure, 2008. **16**(5): p. 755-765.

Chapter 7: Detection of Elevated Immunoglobulin G Levels in Human Serum

7.1 Introduction

Human blood serum contains more than 20,000 different proteins, varying in concentration from 50 g/l to less than 1 ng/l, with an overall protein concentration of ~1 mM [1]. Detecting any changes in the protein content of human blood serum efficiently is an important tool for disease and infection diagnostics, as the levels of certain proteins can be related to specific disease states [2, 3]. However, this can be very difficult due to the vast number, and concentrations, of different proteins present in the serum samples. Two common approaches that have been previously used for serum analysis are; specific recognition of biomarkers (using antibodies), and overall serum analysis using electrophoresis. The trouble with using these methods is that specific antibodies must be developed, electrophoresis is relatively insensitive, and they can be difficult in quantifying the level of protein present [4-6]. This leaves the necessity for a fast and efficient method to detect elevated levels of specific proteins within human serum samples.

In this chapter, we will show a simple and efficient method of detecting elevated levels of the antibody, immunoglobulin G (IgG) within human blood serum solutions. A self-assembled monolayer is added to the nanostructure surface to create an anionic interface for protein binding. The composition of the protein layer formed, called the protein corona, will primarily contain the IgG protein due to the isoelectric point associated with the IgG structure. Serum solutions spiked with different concentrations of IgG are investigated and characterised, using the experimentally measured $\Delta\Delta S$ parameter, relative to stock serum solution. It will be shown from these results that low concentrations of spiked IgG can be detected, however higher concentrations of spiked IgG produce the same response as previous solutions, resulting in multiple IgG concentrations becoming indistinguishable from each other. Due to the protein corona being attracted to the self-assembled monolayer through electrostatic interactions, the sensitivity of these measurements can be tailored to higher IgG concentrations through the addition of sodium chloride (NaCl) to the serum solutions. Finally, we will show that this addition of NaCl to the serum solutions increases the electrostatic shielding involved in the system, lowering the coverage of the protein corona on the nanostructure surface. Allowing much higher concentrations

of IgG to be detected, pushing the limit of detection into the physiologically relevant range necessary for clinical applications.

7.2 Human Blood Serum

Human blood serum can be obtained from whole blood by removing the red and white blood cells, as well as the clotting factors, from the solution. Although there are a vast number of proteins present in human serum, the major constituents present are; albumin, immunoglobulins, transferrin, and lipoproteins [7]. With only ~20 of these proteins making up 99% of the serum protein content by mass [8].

Human Serum Standard			
Proteins in Human Serum Standard	Certified Value (g/L)	Uncertainty (g/L)	Isoelectric Point
α_2 macroglobulin (A2M)	1.43	0.06	-
α_1 acid glycoprotein (AAG)	0.617	0.013	-
α_1 antitrypsin (AAT)	1.12	0.03	-
albumin (ALB)	37.2	1.2	5.4 - 5.8 ^[9]
β -2-microglobulin (B2M)	0.00217	0.00007	-
complement 3c (C3c)	1.00	0.04	-
complement 4 (C4)	0.162	0.007	-
haptoglobin (HPT)	0.889	0.021	-
immunoglobulin A (IgA)	1.80	0.05	4.5 - 6.8 ^[10]
immunoglobulin G (IgG)	9.17	0.18	6.6 - 10 (mean 8.3) ^[9]
immunoglobulin M (IgM)	0.723	0.027	-
transferrin (TRF)	2.36	0.08	5.8 - 6.2 ^[9]
transthyretin (TTR)	0.220	0.018	-

Table 7.01 Table showing the concentration and isoelectric points of constituents present in stock human serum solution [9, 10].

Table 7.01 shows the constituent proteins, as well as their concentrations and isoelectric points, in the stock serum solution used throughout this chapter. From the table, it can be seen that over 50% of the protein present in the stock solution is albumin, with the immunoglobulins the next most abundant, followed by transferrin. Many other proteins are also present in the solution, however at very small concentrations. This makes human serum one of the most difficult protein containing

samples to characterise due to the dominance of albumin present, and the wide range in the abundance of other proteins present in the solution [8].

Although human serum consists of such a large variety of proteins, immunoglobulin G (IgG) is the main target protein being measured in this study. This is due to the levels of IgG present in the solution fluctuating with specific diseases and infections, allowing the diagnosis of these to be confirmed by quantifying the elevated concentration of IgG present within the serum solution.

7.2.1 Immunoglobulin G (IgG)

Immunoglobulin G (IgG) is a large antibody with a molecular weight of ~150 kDa. The protein is made up of two different polypeptide chains, a heavy chain of 50 kDa, and a light chain of 25 kDa. With each IgG antibody consisting of two heavy chains, and two light chains.

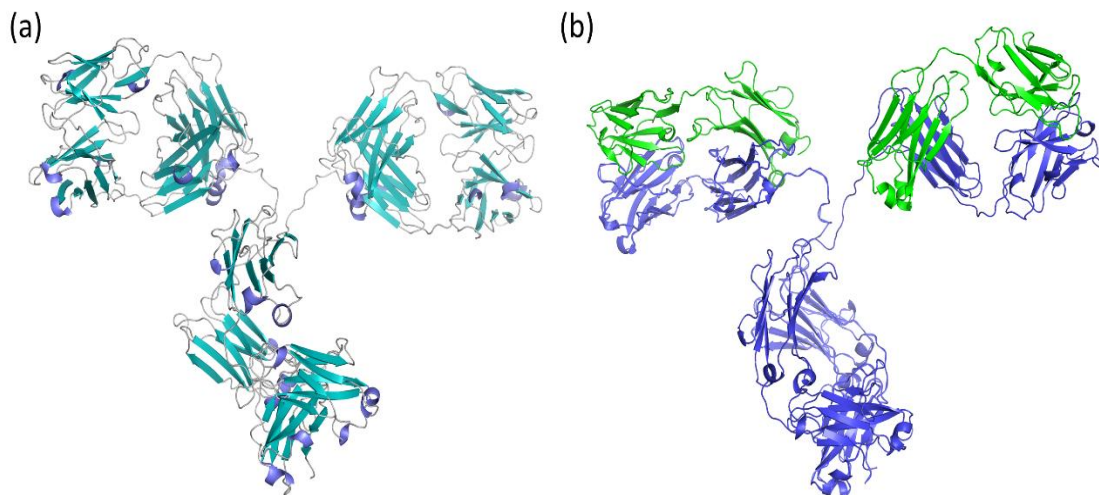


Figure 7.01 (a) Crystal structure of immunoglobulin G antibody (PDB: 1IGT), and (b) showing the heavy chains (blue) and the light chains (green).

Figure 7.01 shows the structure of immunoglobulin antibodies with the heavy and light chains identified in blue and green respectively. Where the two heavy chains are linked by disulphide bonds, with each heavy chain also being connected to a light chain by a disulphide bond [11]. There are five major immunoglobulin classes; IgM, IgD, IgG, IgA, and IgE, with IgG being by far the most abundant, making up nearly 75% of all serum antibodies [12]. Even though IgG is one of the most abundant proteins in human serum solution, it is still only about a quarter of the amount of

albumin present by mass. This makes it difficult to selectively detect from the bulk serum solution containing the vast number of other proteins. However, IgG has a high isoelectric point (pI), on average 8.3, which means that in a solution of pH lower than that, the protein would carry a net positive charge. IgG is the only abundant protein in human serum that has a pI value that high, with the other most abundant proteins, albumin, transferrin and IgA, all having pI values below 7, Table 7.01. This means that at the normal pH of blood serum, pH 7.4, IgG would be the only abundant protein to have a net positive charge, with the others all possessing a net negative charge. The differing isoelectric points of the abundant proteins within human serum is one of the properties exploited for separation by electrophoresis, and isoelectric focusing [13], and will be used here to selectively immobilise IgG on the nanostructured surface.

For various diseases and infections, certain protein levels within human blood serum can be altered. Previous studies have shown that elevated levels of IgG in serum can be a sign of fast progression cystic fibrosis in children [14], chronic liver disease [15], and autoimmune hepatitis [16]. With the amount that IgG is elevated by, being used to distinguish between chronic conditions, and autoimmune conditions [15, 17]. Hence, a simple and efficient method to quantify the level of IgG present in any serum sample would be of benefit for many medical diagnostic applications.

7.2.2 Protein Corona

When proteins from the serum samples adsorb to the nanostructure surface, the resulting protein layer is called the protein corona. The structure and composition of this protein corona can depend on many of the properties of the metamaterial, such as the size and shape of the nanostructures, as well as the functionalisation of the surface. The competitive adsorption of the proteins from the serum solutions on the nanostructure surface is based on the abundance and affinities of the proteins in the solutions, with this effect being known as the Vroman effect [18, 19]. In the Vroman effect, firstly the most abundant proteins are adsorbed to the nanostructure surface, and are replaced over time by the proteins with higher affinities. However, the results shown in Figure 7.02 and reported previously in other studies, show that when the surface is covered with negatively charged particles, proteins with isoelectric points above the pH of the solution (such as IgG) predominantly bind to the surface [20]. Hence by functionalising the nanostructures with NTA, the composition of the protein corona for serum solutions is altered to be predominantly made up of IgG.

7.3 Results and Discussion

A nitrilotriacetic acid (NTA) monolayer was added to the surface with no spacer molecule, to give complete NTA coverage, and without the addition of the Ni^{2+} solution described in chapter 3. By forming the monolayer in this way, a completely anionic surface is created on the nanostructure surface. This should allow us to enhance the adsorption of the IgG protein to the surface, compared with any of the other abundant proteins within the serum samples. To view the binding characteristics of the target protein (IgG), and the most abundant protein in human serum (Albumin), solutions of both proteins, of increasing concentrations, were made up in 10 mM Tris buffer and added to the surface. With the average shift and $\Delta\Delta S$ values plotted in Figure 7.02.

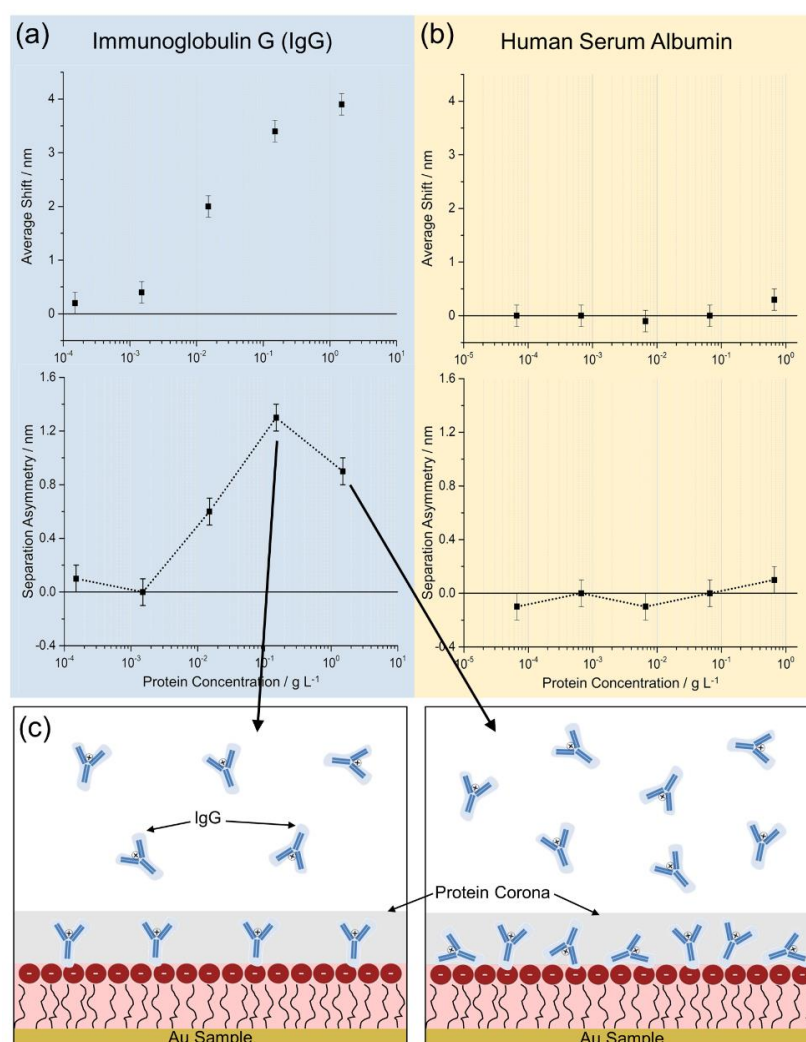


Figure 7.02 Average shift (top), and separation asymmetry (bottom) values for solutions of (a) immunoglobulin G (left, blue background), and (b) human serum albumin (right, orange background) in 10 mM Tris buffer. (c) Graphical description of protein corona composition for two IgG concentrations depicted by the arrows from part (a). The error bars represent the standard error calculated from 8 spectra measurements.

As described in chapter 3, the average shift parameter is an analogue of a surface plasmon resonance measurement, describing the coverage of the adsorbed layer on the metamaterial surface. The average shift results in Figure 7.02 show that, when a pure solution of IgG is added to the functionalised nanostructures, IgG is adsorbed on the anionic ligand with the coverage increasing as the protein concentration increases. However, both the average shift data, and the asymmetry values measured for the human serum albumin solutions, show that any albumin that is adsorbed is below the detection limit of the system. The asymmetry parameters for the IgG solution, which does adsorb to the surface, show an increasing asymmetry with increasing concentrations, but begins to decrease again as the solution reaches its highest concentration. We theorise that this decrease in the asymmetry value at higher concentrations of IgG, is a result of the increasing coverage of the protein on the nanostructure surface. It has been shown in the previous chapters, that the orientation of the proteins adsorbed on the chiral shuriken surface has a large effect on the magnitude of the asymmetry value produced, with the protein arrangement and orientation being a key factor in the composition of the protein corona [21-24]. At lower protein concentrations, when the coverage on the surface is smaller, the adsorbed proteins will be able to all align in a similar orientation leading to an increase in the asymmetry parameter value. However, at higher concentration solutions, where there is a greater coverage at the surface, it is theorised that the proteins will be more tightly packed leading to a more isotropic layer at the nanostructure surface (Figure 7.02(c)), and a decrease in the separation parameter observed, as seen for solutions of IgG in Figure 7.02(a).

7.3.1 IgG Spiked Serum Measurements

To test the capability of this approach for measuring elevated protein levels in human serum, five different concentrations of IgG spiked serum were made from a stock serum solution with a total protein concentration of 60 g/L. The normal level of IgG in blood serum, and the percentage in the stock serum solution purchased, is ~15.3% of the total protein content by mass. The stock solution was then spiked with IgG to give a total IgG concentration in the solutions of 16.1%, 17.0%, 18.6%, 21.1%, and 23.6% by mass. Each solution was diluted in 10 mM Tris buffer, pH 7.4, to give solution concentrations ranging from 3 g/L to 3×10^{-4} g/L. The separation asymmetry, $\Delta\Delta S$, for each measurement in the reflectance spectra was calculated as described in the previous chapters.

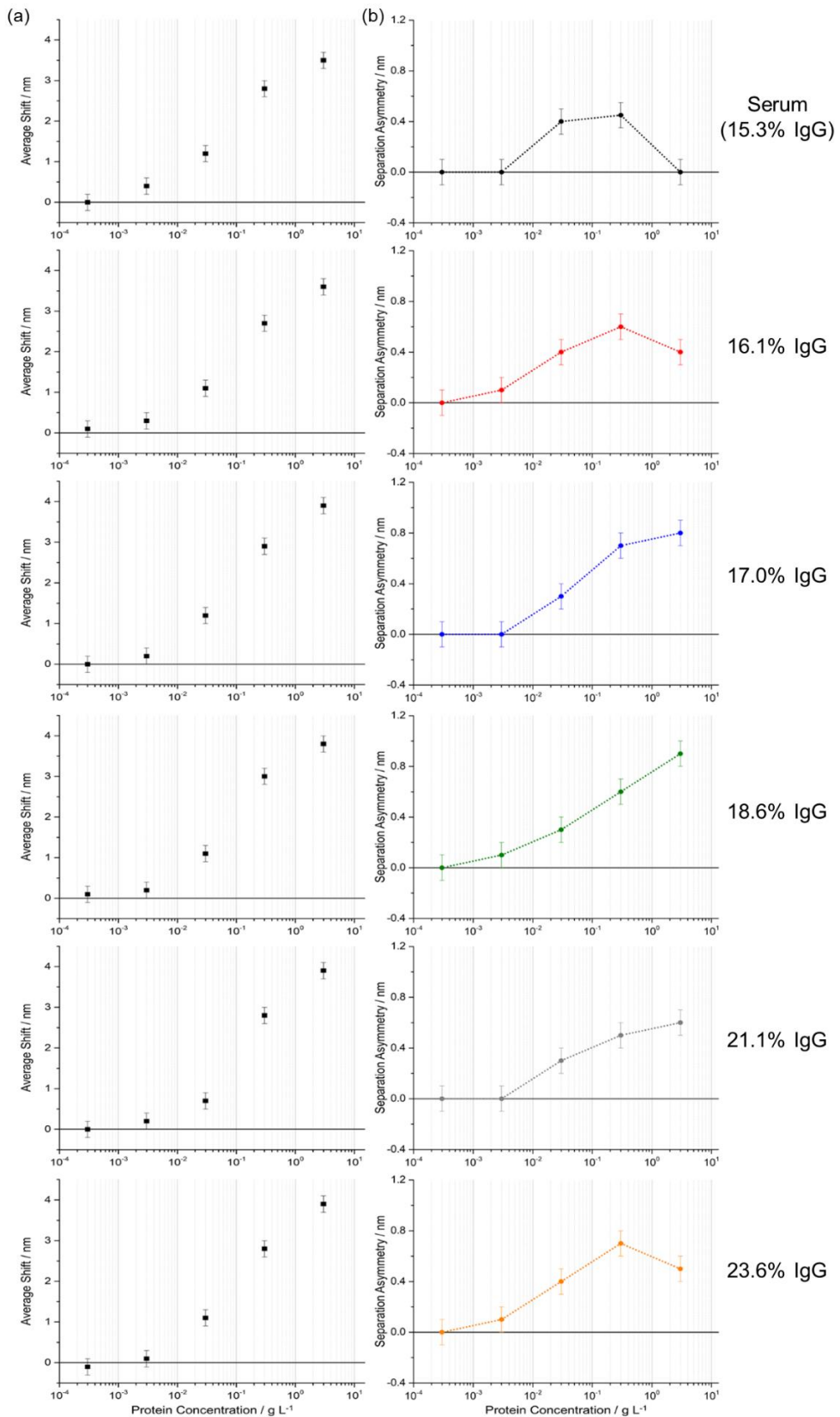


Figure 7.03 Graphs showing (a) average shifts, and (b) asymmetry values for increasing total protein concentration for stock serum solution, and all IgG spiked serum solutions diluted in Tris buffer. The error bars represent the standard error calculated from 8 spectra measurements.

Figure 7.03 shows the experimentally measured average shifts, and asymmetry values for the stock serum solution, and all the IgG spiked serum solutions with increasing concentrations. When looking at the average shift data for stock serum, and all IgG spiked concentrations, they all produce the same average shift profile, with the highest protein concentration solutions showing a coverage with an average shift of ~4 nm. This shows that the coverage of the protein corona at the nanostructure surface is the same for each of the solutions, and hence any changes that can be observed for each solution is due to the composition of the protein corona changing rather than the coverage.

The separation asymmetry results, $\Delta\Delta S$, show that at the two lowest protein concentrations for all solutions, no asymmetry change was detected within experimental error. However, for the stock serum solution, the asymmetry value begins to increase with the 0.03 g/L solution, and continues increasing with the 0.3 g/L solution. Once the highest protein concentration solution is added to the nanostructure surface, 3 g/L solution, the asymmetry value decreases again back to zero. This behaviour is similar to the IgG only solution shown in Figure 7.02, and again is a consequence of the increased IgG concentration at the surface, creating a more isotropic environment. All five of the spiked serum solutions (shown in red, blue, green, grey, and orange in Figure 7.03) follow the same trend originally. Hence, for all solutions there is a zero asymmetry value for the lowest concentration of solution, with the asymmetry parameter increasing up to the 0.03 g/L concentrated solution. However, the spiked solutions then begin to be separated at the 0.3 g/L concentration, with the largest differences being observable at the top concentration of 3 g/L. At this highest concentration, all five spiked serum solutions are easily separable from the stock serum solution, containing only 15.3% IgG. The lowest spiked concentration, with a total IgG content of 16.1%, still shows a decrease in the asymmetry parameter going from 0.3 g/L to 3 g/L. However, this decrease is much less, and still gives an asymmetry value of 0.4 nm above the stock solution at this concentration. When the next two spiked serum solutions are added, 17.0% and 18.6% total IgG content, the asymmetry separation continues to increase between the 0.3 g/L and 3 g/L concentrations. Both of these spiked serum solutions, at the highest concentration solution, increase to an asymmetry value of ~1.0 nm above the stock serum solution. However, with the two highest spiked serum solutions, containing 21.1% and 23.6% IgG, the asymmetry values begin to decline again from the peak value produced at the highest concentration. This results in the asymmetry values for the highest

concentration solution being 0.6 nm and 0.5 nm for the 21.1% and 23.6% spiked solutions respectively.

Since all the IgG spiked serums are inseparable at the lower concentrations of each solution, the higher concentration solutions are where the different IgG contents become distinguishable, and can be used for quantitative measurements. As the highest concentration solution of each spiked serum sample, 3 g/L, shows the greatest discrimination between samples and the stock serum solution, we can plot the asymmetry value produced at this concentration against the IgG content of each spiked serum. By taking the asymmetry parameter from each spiked solution at the highest total protein concentration, and plotting it against the IgG content of that solution, it is easy to see the quantitative sensitivity of these measurements. Figure 7.04 shows the asymmetry parameter from the 3 g/L solution of each serum sample, with the stock solution containing 15.3% IgG content by mass. With the five other spiked solutions containing 16.1%, 17.0%, 18.6%, 21.1%, and 23.6% IgG.

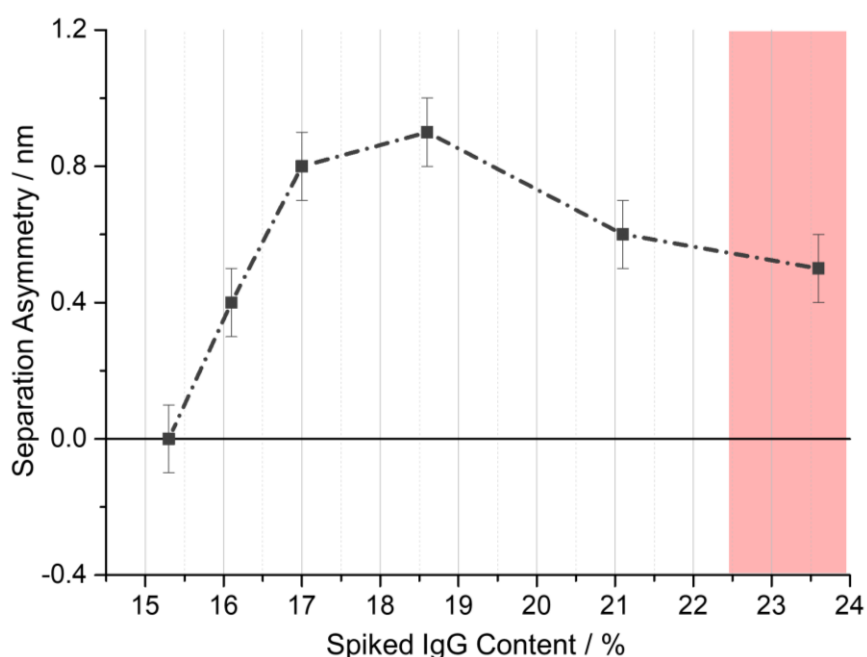


Figure 7.04 Graph showing the asymmetry value for the highest concentration solution of each spiked sample. Red background region shows the physiologically elevated levels of IgG in human serum. The error bars represent the standard error calculated from 8 spectra measurements.

The results in Figure 7.04 show that from stock serum solution (first point, 15.3% IgG), there is a steady increase in the asymmetry value produced by spiking human serum with IgG. However, once the concentration of IgG in the serum sample reaches ~19%,

the asymmetry parameter value begins to drop again. With the asymmetry value achieved for the highest IgG spiked solution being 0.5 nm, down from 0.9 nm for the 18.6% IgG serum solution. As the protein corona will also contain proteins other than IgG, the coverage remains the same with increasing IgG concentration, however the composition will differ. The area in Figure 7.04 with the red background is the region where the increase in IgG becomes physiologically relevant, with these levels being measurably higher than seen in the normal range [25]. In this case, the lower concentrations can easily be detected, with the asymmetry value gradually increasing as the IgG content increases, showing that the sensitivity of the method is suitable for these measurements. However, the current results show that detection of physiologically high levels of IgG are not possible, with the asymmetry parameter decreasing as the concentration of IgG reaches this range. Since the asymmetry value decreases again after a certain concentration of IgG, it becomes very difficult to separate samples, as two (or more) samples with different IgG concentrations would produce the same response. Hence, it would be difficult when measuring a sample of unknown concentration to tell if the IgG content was 16.5% or 23.5% for example, as these would produce the same ~0.5 nm response for both measurements.

7.3.2 Saline Buffered Spiked Serum Measurements

In the previous section, section 7.3.1, the serum solutions were all diluted using 10 mM Tris buffer. In the following results, both the stock serum and all IgG spiked serum solutions were diluted in 10 mM Tris-saline buffer, containing 150 mM sodium chloride (NaCl). The solutions were prepared in the same way as in section 7.3.1, but diluted with Tris-saline buffer, to give three IgG spiked concentrations of 18.6%, 21.1%, 23.6% by mass (the three highest concentrations used in the previous measurements). Sodium chloride was added to the dilution buffer used for each serum solution, to increase the ionic strength of the system. Hence, increasing the ionic strength of the solution, with 150 mM NaCl, resulted in lower protein adsorption to the functionalised surface, as a result of electrostatic screening lowering the electrostatic interactions between the functionalised surface and the proteins in solution.

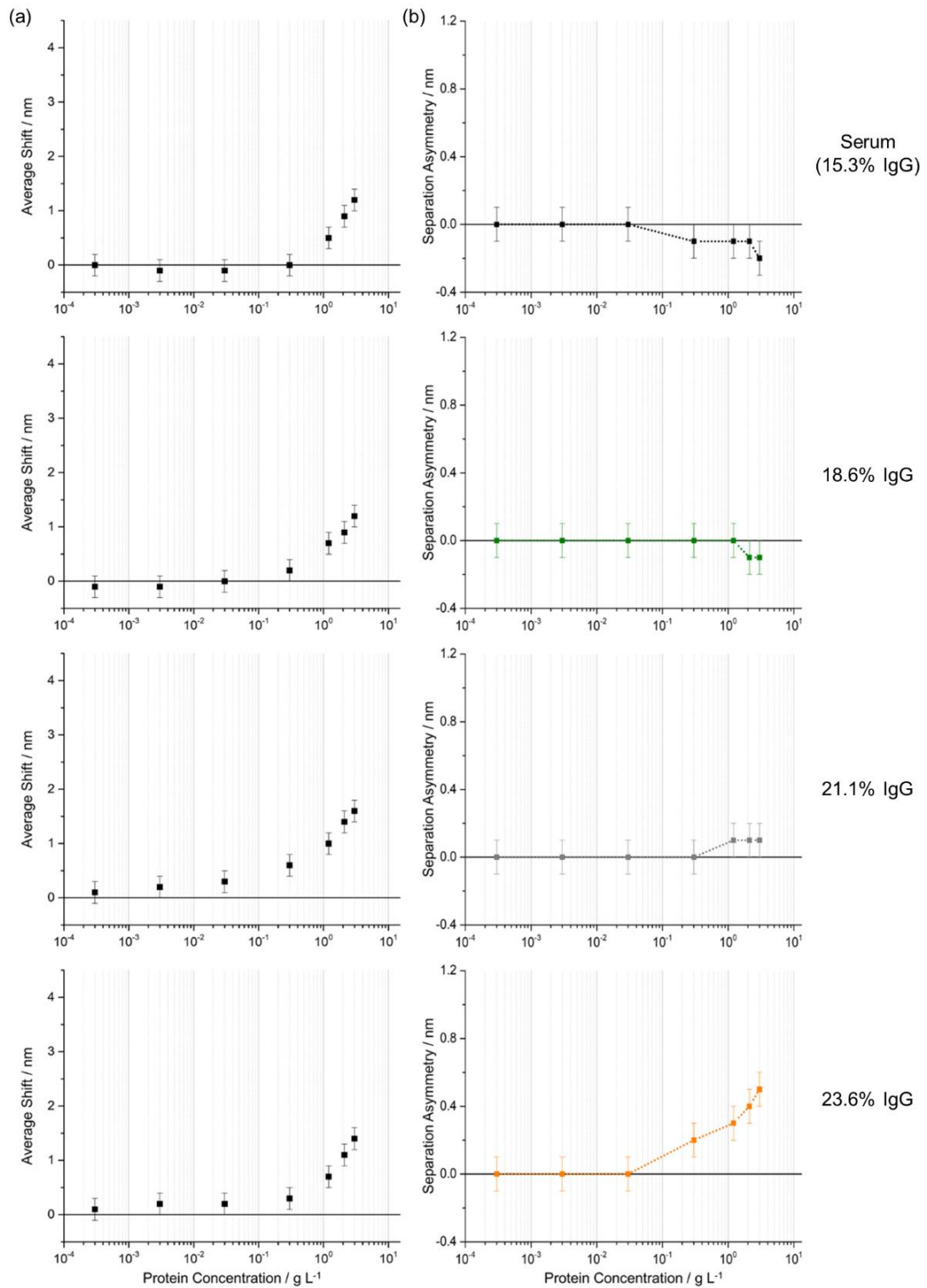


Figure 7.05 Graphs showing (a) average shifts, and (b) asymmetry values for increasing total protein concentration for stock serum solution, and all IgG spiked serum solutions diluted in Tris-saline buffer. The error bars represent the standard error calculated from 8 spectra measurements.

The results in Figure 7.05 show the experimentally measured average shifts and asymmetry values for the stock serum solution, and IgG spiked solutions of increasing concentrations, diluted in Tris-saline buffer. The average shift values when the solutions are diluted in a Tris-saline buffer still show a similar profile for every solution, however the coverage at the highest, 3 g/L, protein concentration solution only shows an average shift value of ~1.5 nm. This is considerably smaller than the ~4 nm average shift value produced for the Tris buffer diluted samples in Figure 7.03. The stock serum solutions, and IgG spiked solutions with IgG contents of 18.6% and 21.1% all show very similar asymmetry profiles to each other, suggesting that only minimal increased IgG binding is occurring on the nanostructure surface as the concentration of IgG in the solution increases. However, when the IgG concentration in the serum solution is raised to 23.6%, the asymmetry value begins to rise again until it reaches 0.5 nm at a total protein concentration of 3 g/L. This, suggests that when the IgG content in the serum solution reaches a suitably high level, the concentration of IgG present in the protein corona also increases. However, unlike the 23.6% IgG content solution diluted in Tris buffer in Figure 7.03, the concentration of IgG in the corona is still relatively low and therefore can still adsorb freely to the charged surface, leading to the increase in the $\Delta\Delta S$ asymmetry seen in Figure 7.05. As the average shift values do not change when solutions with an increased concentration of IgG are added to the system, we can again conclude that the differences being observed here are purely down to the composition of the protein corona changing (to include a higher concentration of IgG), rather than a higher protein coverage.

In the same way as was done for the Tris buffer diluted serum samples, the asymmetry value for the stock serum solution and IgG spiked serum solutions diluted in Tris-saline buffer were plotted against the IgG content of each solution. These results are plotted in Figure 7.06, along with the previous results from the Tris buffer only dilutions, shown in Figure 7.04. The solutions diluted in Tris buffer only (no addition of NaCl) are shown in grey, where the solutions diluted in Tris-saline buffer are shown in purple for the same IgG spiked concentrations between each buffer. The same red highlighted area signifying the concentration where the IgG increase becomes physiologically relevant is also included from Figure 7.04.

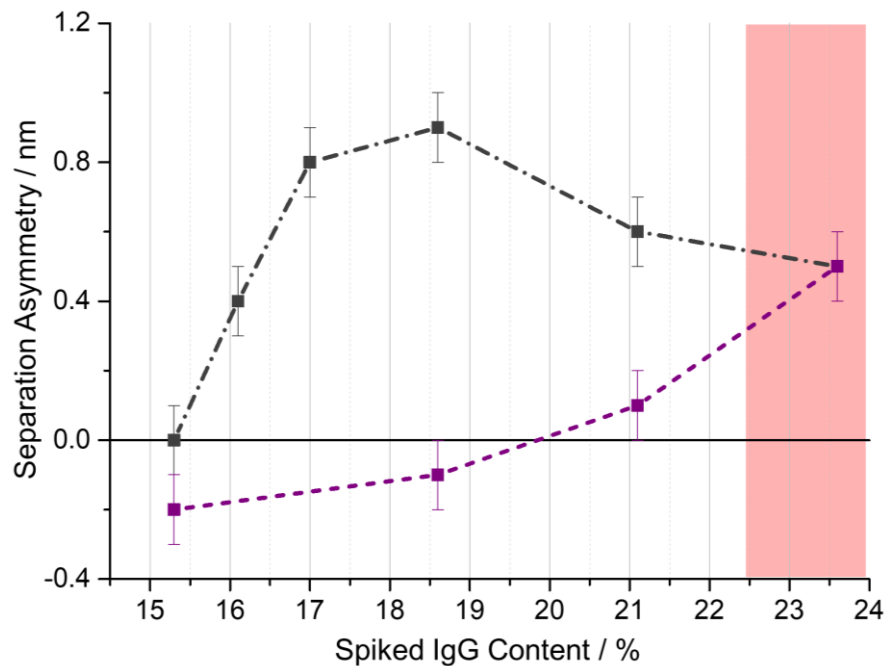


Figure 7.06 Graph showing the asymmetry value for the highest concentration solution of each spiked sample for Tris buffer only dilutions (grey), and Tris-saline buffer dilutions (purple). Red background region shows the physiologically elevated levels of IgG in human serum. The error bars represent the standard error calculated from 8 spectra measurements.

When the separation asymmetry results for the Tris-saline diluted solutions are plotted against the IgG content, as shown in Figure 7.06, the differences between diluting the samples in Tris buffer only, or Tris-saline buffer become much more distinguished. As discussed previously, when the samples are diluted in Tris-buffer only, the separation asymmetry increases as the IgG content initially increases from stock serum solution, but then begins to decrease again after an IgG content of 18.6%. Meaning that multiple solutions with different IgG contents become indistinguishable from each other. However, when the IgG spiked serum solutions are diluted in Tris-saline buffer, the behaviour of the separation asymmetry varies completely from the Tris buffer solutions. When the spiked solutions are diluted with the Tris-saline buffer solution, the separation asymmetry continues to increase with increasing IgG content all the way up to the highest concentration of 23.6% IgG. In contrast to the solutions diluted by the Tris buffer only, each different IgG concentrated solution produces a gradual increase in the asymmetry value, including for the high physiologically relevant concentrations (23.6% IgG), shown by the red bar in Figure 7.06. This addition of 150 mM NaCl to the dilution buffer, increases the concentrations of IgG that can be detected in the spiked serum samples, and pushes

the limits into the clinically relevant range that would be required for the quantitative analysis of elevated IgG samples in commercial and clinical applications.

7.3.3 Non-IgG Spiked Serum Solutions

As control measurements, to validate the enhanced adsorption of IgG over other serum proteins, the stock serum solutions were spiked with three other highly abundant serum proteins; Albumin, Transferrin, and Immunoglobulin A (IgA). However, in contrast to IgG, the isoelectric points of these three serum proteins are all lower than that of IgG, resulting in all three having a net negative charge in the dilution buffers of pH 7.4. The solutions were prepared identically to the IgG spiked serum samples, with the respective protein (either albumin, transferrin, or IgA) being added to the stock solution and the total protein concentration remaining at 3 g/L. These solutions were once again diluted using either Tris buffer or Tris-saline buffer in order of magnitude steps to 3×10^{-4} g/L concentration.

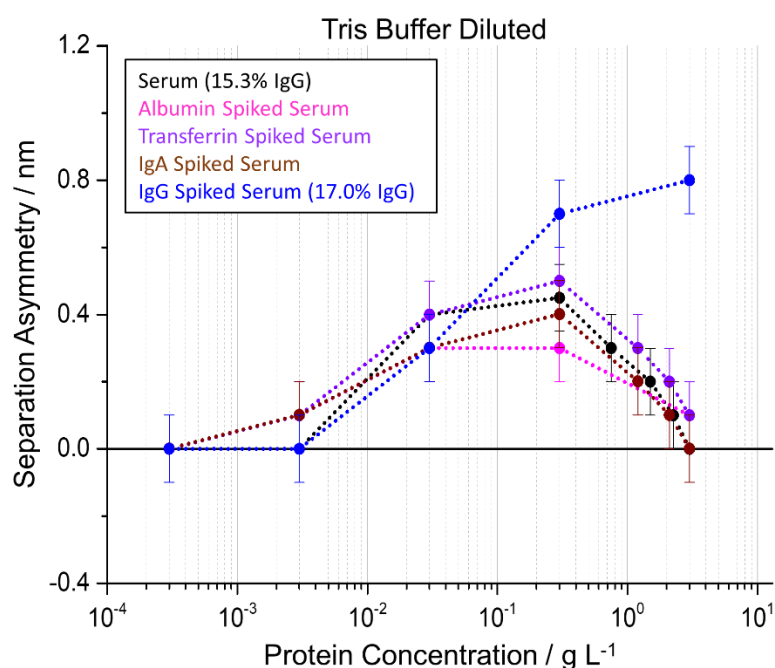


Figure 7.07 Graph showing the asymmetry parameters for increasing total protein concentration for stock serum (black), Albumin spiked serum (pink), Transferrin spiked serum (purple), and IgA spiked serum (maroon) diluted in Tris buffer. IgG spiked solution containing 17.0% IgG, and diluted in Tris buffer, shown for comparison purposes. The error bars represent the standard error calculated from 8 spectra measurements.

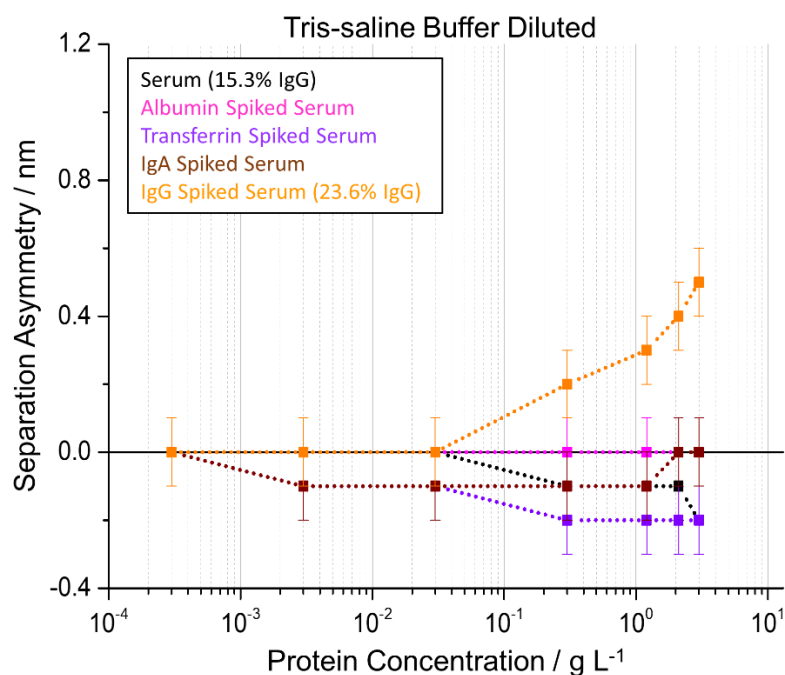


Figure 7.08 Graph showing asymmetry parameters for increasing total protein concentration for stock serum (black), Albumin spiked serum (pink), Transferrin spiked serum (purple), and IgA spiked serum (maroon) diluted in Tris-saline buffer. IgG spiked solution containing 23.6% IgG, and diluted in Tris-saline buffer, shown for comparison purposes. The error bars represent the standard error calculated from 8 spectra measurements.

Figures 7.07 and 7.08 show the separation asymmetry values obtained when the stock serum solutions were spiked with albumin, transferrin, and IgA, and diluted using Tris buffer or Tris-saline buffer respectively. In both figures, the IgG concentration that showed the largest asymmetry value at the highest protein concentration for each dilution buffer has been added for comparison. In the Tris buffer diluted serums, all three of the albumin, transferrin and IgA spiked solutions show no change (within experimental error) relative to the stock serum solution. In the case of the albumin, transferrin, and IgA spiked solutions diluted in Tris-saline buffer, there are also no changes within experimental error of the respective stock serum solution. For both cases, the IgG spiked serum shown produces much larger asymmetry values than any of the other spiked protein serum solutions. Even though Albumin is the most abundant protein, making up over 50% of the total protein content in serum, and IgA is the next most abundant immunoglobulin protein present after IgG. Showing that this method of binding to the nanostructure surface, and measuring the separation asymmetry, is solely sensitive to the IgG content of the human serum

solution, which is a result of the isoelectric points of each protein and the anionic ligand attached to the nanostructure surface.

7.3.4 Discussion

When the ideal protein solutions, both IgG and human serum albumin, were added to the functionalised nanostructure surface, only binding of IgG from the bulk solution was detected. With any albumin adsorption below the detection limit of the system. This is shown by the average shift data, which shows the increasing coverage of IgG on the nanostructure surface, with increasing protein concentration. However, the average shift with increasing albumin concentration, as well as the asymmetry value, does not increase out with experimental error. When the asymmetry parameter, $\Delta\Delta S$, for the pure IgG solution is measured, it shows an increase in separation with increasing protein concentration, until the final solution of highest concentration, where the asymmetry value decrease once again. This decrease in the separation asymmetry at higher IgG solution concentrations, is a consequence of the increased surface coverage of the protein. It has been shown in previous chapters of this thesis that the orientation of adsorbed proteins can have a large effect on the magnitude of the $\Delta\Delta S$ values observed. Hence, at the lower concentration solutions, the coverage of the protein at the nanostructure surface is small, which allows the IgG molecules to align in their preferred orientation, and leads to an increase in the asymmetry parameter measured. However, when the concentration of the IgG adsorbed on the nanostructure surface is sufficiently high, there is an increased coverage (shown in Figure 7.02(a)), resulting in the proteins being more tightly packed and randomly orientated, Figure 7.02(c). Which leads to the observed decrease in $\Delta\Delta S$ at high IgG concentration.

When the serum solutions were diluted with Tris buffer, shown in Figure 7.03, the shape of the asymmetry values, with increasing protein concentration, produce the same trend as the pure IgG solution. With the average coverage of the protein corona remaining the same, ~ 4 nm, upon spiking the solution with increasing concentrations of IgG. Showing that, since the protein corona will also consist of other proteins from the serum solution, the asymmetry parameter $\Delta\Delta S$, for each increasing IgG spiked solution, is sensitive to the composition of the protein corona, and not to the overall surface coverage. Hence, increased concentrations of IgG will be displacing other proteins from the corona layer, meaning the coverage remains the same but with an increased concentration of IgG present within the protein corona.

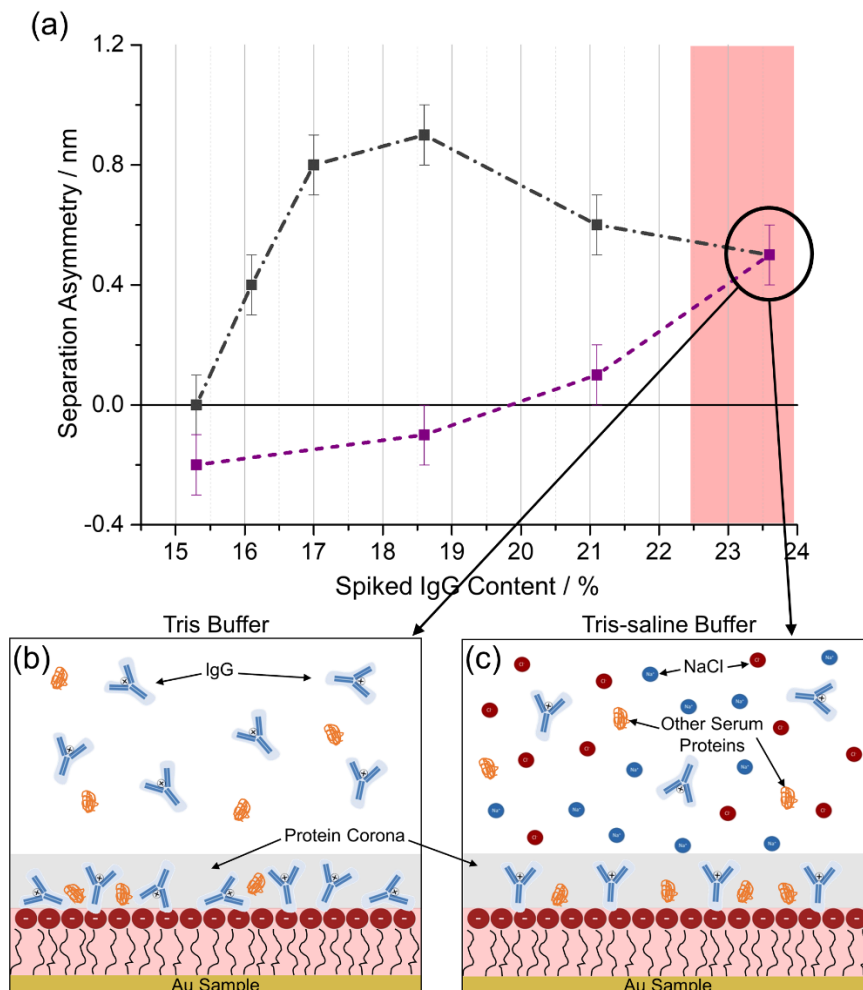


Figure 7.09 (a) Asymmetry values for the highest concentration solutions diluted in Tris buffer (grey), and Tris-saline buffer (purple) for increasing spiked IgG contents. Graphical depiction of the protein corona for the 23.6% elevated IgG serum solution diluted in (b) Tris buffer, and (c) Tris-saline buffer. The error bars represent the standard error calculated from 8 spectra measurements.

The shape of the graph shown in Figure 7.09(a), when diluted in Tris buffer (grey line) can be regarded as being due to the concentration of IgG present within the protein corona. When the IgG content in the solutions increases, the amount of IgG within the corona also increases, but is still sufficiently low to allow ordering of the adsorbed IgG below a concentration of 19.0% IgG. This allows the gradual increase in the asymmetry value when increasing the IgG content in the serum solution. However, when the IgG content in the solution increases above ~19.0%, the IgG content of the protein corona increases further, and results in a tightly packed isotropic layer, as shown in Figure 7.09(b). When the composition of the protein corona contains a high concentration of IgG, relative to other serum proteins, the corona continues to

become increasingly more disordered. Which results in the asymmetry value continuing to decrease, for the solutions from 19.0% to 23.6%, in a similar fashion as seen in Figure 7.02 for pure IgG solutions of increasing concentration. Hence, two serum solutions containing differing levels of IgG, such as 16.5% and 23.5% would produce the same asymmetry response, and would be indistinguishable from each other.

When the serum solutions are diluted with Tris-saline buffer, containing 150 mM NaCl, the coverage of the protein corona decreases to ~ 1.5 nm, as shown in Figure 7.05. This decrease in the coverage of the protein corona, to less than half the initial coverage, is a result of the increased ionic strength of the dilution buffer. Hence, the increased ionic strength of the solution increases the electrostatic shielding between the proteins in solution and the surface charge of the anionic ligand, and results in a decrease in the amount of adsorbed protein within the corona layer [26]. Since the amount of adsorbed protein within the corona layer is decreased, the effective concentration of IgG present within this layer is also lower than that of the Tris buffer diluted samples, shown in Figure 7.09(c). When the two 23.6% IgG solutions diluted in either Tris buffer or Tris-saline buffer are added to the nanostructure surface, the hypothesised corona model can be seen in Figure 7.09(b) and (c). Due to the high concentration of IgG present in the serum solution, when diluted with Tris buffer the IgG content of the protein corona is high, resulting in the IgG being tightly packed and disordered within the corona layer. However, when the same high IgG concentration solution was added, diluted in Tris-saline buffer, the effective concentration of IgG within the corona layer is decreased, resulting in a more ordered protein layer adsorbed on the surface for the same bulk solution concentration, Figure 7.09(c). Hence, since the chiral fields around the nanostructure are sensitive to the orientation and alignment of the proteins immobilised at the nanostructure surface, as shown throughout this thesis, lowering the effective concentration within the protein corona allows the proteins to adsorb to the surface in their preferred orientation. This allows the detection of sufficiently high concentrations of elevated IgG in human serum to be experimentally measured, and raises the level of detection possible into the physiologically relevant range required for many diagnostic applications.

7.4 Conclusion

In this chapter, we have further developed the use of the $\Delta\Delta S$ parameter introduced in the previous two chapters. However, in this chapter we have introduced the addition of a complex real life solution, human blood serum, which contains a multitude of different proteins at varying concentrations. Human blood serum was spiked with increasing concentrations of IgG, and two dilution buffers of differing ionic strengths were used to dilute the serum solutions.

When the serum solutions were diluted with Tris buffer (no NaCl added), an increase in the $\Delta\Delta S$ value was initially observed at lower spiked concentrations. However, when the elevated IgG levels increased into the physiologically relevant concentration range, a decrease in the $\Delta\Delta S$ value was observed, making these solutions indistinguishable from solutions of lower spiked levels. The coverage of the protein corona layer remained constant for each spiked solution, providing validation that only the composition of the corona was being altered upon increasing IgG in the bulk solution. Hence, at high IgG spiked concentrations, the protein layer would consist of a high proportion of IgG that would be tightly packed and randomly orientated within the corona, as depicted in Figure 7.09(b). Since the chiral fields of the nanostructures have been shown to be sensitive to the orientation and alignment of the adsorbed proteins, this would result in the decrease in the $\Delta\Delta S$ parameter value at the higher concentrations.

When the ionic strength of the buffer, used to dilute the serum solutions, is increased by adding 150 mM NaCl to the Tris buffer, low concentrations of spiked IgG become undetectable. However, the higher 23.6% IgG spiked solution can be detected due to a shift in the limit of detection to higher concentrations. This occurs due to the electrostatic shielding of the higher ionic strength buffer between the proteins in solution and the charged binding surface, resulting in a lower coverage on the surface by the protein corona. Hence, with the electrostatic shielding from the Tris-saline buffer, the effective concentration of IgG in the protein corona is lowered. Resulting in the 23.6% IgG spiked serum solution in Tris-saline buffer, eliciting the same response in the $\Delta\Delta S$ parameter as a 16.5% IgG spiked serum solution diluted in Tris buffer only.

In summary, we have demonstrated in this chapter, that a quantitative analysis of the IgG content in human serum solutions can be achieved experimentally using the $\Delta\Delta S$ parameter introduced in chapters 5 and 6. The levels of elevated IgG in the serum solutions can be detected for very low concentrations when diluted in Tris buffer, and

high concentrations well outside of the 'normal' patient range by increasing the ionic strength of the dilution buffer. This allows us to push the levels of detection possible into the appropriately high IgG range, and shows that elevated concentrations of IgG can be selectively detected in human serum solutions. This is the first demonstration of this phenomena being applied to a complex protein solution, such as human blood serum, and shows a new paradigm for detecting and quantifying elevated IgG levels at the physiologically high concentrations necessary in a clinical environment.

7.5 References

1. De, M., et al., *Sensing of proteins in human serum using conjugates of nanoparticles and green fluorescent protein*. Nature Chemistry, 2009. **1**(6): p. 461-465.
2. Bryan, T., et al., *An optimised electrochemical biosensor for the label-free detection of C-reactive protein in blood*. Biosensors and Bioelectronics, 2013. **39**(1): p. 94-98.
3. Kell, D.B. and E. Pretorius, *Serum ferritin is an important inflammatory disease marker, as it is mainly a leakage product from damaged cells*. Metallomics, 2014. **6**(4): p. 748-773.
4. Badgwell, D. and R.C. Bast Jr, *Early detection of ovarian cancer*. Disease Markers, 2007. **23**(5, 6): p. 397-410.
5. Murphy, G.P., et al., *Current evaluation of the tissue localization and diagnostic utility of prostate specific membrane antigen*. Cancer, 1998. **83**(11): p. 2259-2269.
6. McPherson, R.A. and M.R. Pincus, *Henry's clinical diagnosis and management by laboratory methods*. 2016: Elsevier Health Sciences.
7. Adkins, J.N., et al., *Toward a human blood serum proteome analysis by multidimensional separation coupled with mass spectrometry*. Molecular & Cellular Proteomics, 2002. **1**(12): p. 947-955.
8. Anderson, N.L. and N.G. Anderson, *The human plasma proteome history, character, and diagnostic prospects*. Molecular & cellular proteomics, 2002. **1**(11): p. 845-867.
9. Jin, Y., et al., *Estimation of isoelectric points of human plasma proteins employing capillary isoelectric focusing and peptide isoelectric point markers*. Electrophoresis, 2002. **23**(19): p. 3385-3391.
10. Prin, C., et al., *Isoelectric restriction of human immunoglobulin isotypes*. Biochimica et Biophysica Acta (BBA)-General Subjects, 1995. **1243**(2): p. 287-289.
11. Janeway, C.A., et al., *Immunobiology: the immune system in health and disease*. 5th ed. 2001: Garland Science.
12. Junqueira, L.C. and J. Carneiro, *Basic histology*. 11th ed. 2005: McGraw Hill.
13. Dale, G. and A. Latner, *Isoelectric focusing of serum proteins in acrylamide gels followed by electrophoresis*. Clinica Chimica Acta, 1969. **24**(1): p. 61-68.
14. Wheeler, W.B., et al., *Progression of cystic fibrosis lung disease as a function of serum immunoglobulin G levels: a 5-year longitudinal study*. The Journal of Pediatrics, 1984. **104**(5): p. 695-699.
15. Fallatah, H.I. and H.O. Akbar, *Elevated serum immunoglobulin G levels in patients with chronic liver disease in comparison to patients with autoimmune hepatitis*. Libyan Journal of Medicine, 2010. **5**(1).
16. Hennes, E.M., et al., *Simplified criteria for the diagnosis of autoimmune hepatitis*. Hepatology, 2008. **48**(1): p. 169-176.
17. Choi, E.K., et al., *The sensitivity and specificity of serum immunoglobulin G and immunoglobulin G4 levels in the diagnosis of autoimmune chronic pancreatitis: Korean experience*. Pancreas, 2007. **35**(2): p. 156-161.
18. Vroman, L., et al., *Interaction of high molecular weight kininogen, factor XII, and fibrinogen in plasma at interfaces*. Blood, 1980. **55**(1): p. 156-159.

19. Aggarwal, P., et al., *Nanoparticle interaction with plasma proteins as it relates to particle biodistribution, biocompatibility and therapeutic efficacy*. *Advanced Drug Delivery Reviews*, 2009. **61**(6): p. 428-437.
20. Gessner, A., et al., *Functional groups on polystyrene model nanoparticles: influence on protein adsorption*. *Journal of Biomedical Materials Research Part A*, 2003. **65**(3): p. 319-326.
21. Monopoli, M., et al., *Physical-chemical aspects of protein corona: relevance to in vitro and in vivo biological impacts of nanoparticles*. *Journal of the American Chemical Society*, 2011. **133**(8): p. 2525-2534.
22. Mahon, E., et al., *Designing the nanoparticle–biomolecule interface for “targeting and therapeutic delivery”*. *Journal of Controlled Release*, 2012. **161**(2): p. 164-174.
23. Walkey, C.D. and W.C. Chan, *Understanding and controlling the interaction of nanomaterials with proteins in a physiological environment*. *Chemical Society Reviews*, 2012. **41**(7): p. 2780-2799.
24. Gunawan, C., et al., *Nanoparticle–protein corona complexes govern the biological fates and functions of nanoparticles*. *Journal of Materials Chemistry B*, 2014. **2**(15): p. 2060-2083.
25. Agarwal, S. and C. Cunningham-Rundles, *Assessment and clinical interpretation of reduced IgG values*. *Annals of Allergy, Asthma & Immunology: Official Publication of the American College of Allergy, Asthma, & Immunology*, 2007. **99**(3): p. 281.
26. Pasche, S., et al., *Effects of ionic strength and surface charge on protein adsorption at PEGylated surfaces*. *Journal of Physical Chemistry B*, 2005. **109**(37): p. 17545-17552.

Summary and Future Outlook

This thesis has presented a series of experiments detailing the use of chiral metamaterials for ultrasensitive biosensing measurements. This builds upon the previous work produced, in developing a high throughput injection moulding method for creating nanopatterned plasmonic substrates, and utilises these substrates for biosensing applications with ideal and complex protein solutions. In this section, we will provide a brief summary of the results presented in chapters 4 to 7, and consider where this work may be expanded in future applications.

In the first results chapter, chapter 4, we build upon previous work where different structural motifs of proteins were discriminated using chiral structures that exhibit electromagnetic fields that possess a greater chiral asymmetry than circularly polarised light, termed 'superchiral'. We investigate the sensitivity of these superchiral field enhancements to ligand induced conformational changes of proteins adsorbed onto the nanostructure surface. Two proteins from the Shikimate pathway, a seven-step metabolic pathway found in plants and bacteria, were used due to each protein exhibiting a well characterised conformational change in their higher order structure upon specific ligand binding. To characterise these changes, optical rotatory dispersion spectra were measured, and the changes characterised using the asymmetry parameter $\Delta\Delta\lambda$. With this parameter essentially measuring the changes in the effective refractive index on the asymmetry of the generated chiral fields. Utilising this 'superchiral polarimetry', which effectively measures the spectral position dependence of the plasmonic resonance on the dielectric environment surrounding the nanostructure surface, we show that the sensitivity of this phenomenon is increased relative to conventional chiroptical techniques, such as circular dichroism (CD). Since conventional circular dichroism can routinely only detect changes in the secondary and, to a much lesser extent, tertiary structure of proteins, the conformational changes induced for these two sample proteins are undetectable with CD spectroscopy. Hence, due to the anisotropy change of the protein structure upon these conformational changes, this phenomenon produces a highly sensitive probe for observing higher order changes in surface immobilised protein molecules.

In chapter 5 of this thesis, we introduced two new parameters for characterising the changes observed upon the addition of biological samples to the nanostructure surface. The experimentally observed parameter, $\Delta\Delta S$, and the modelled parameters for retardation phase changes, $\Delta\Delta\theta$ and $\Delta\Delta\phi$. To extract these parameters, reflectance measurements were recorded for the chiral shuriken structures, which

exhibited electromagnetically induced transparency (EIT) like behaviour. This plasmonic analogue of EIT is a result of the interference between bright and dark hybrid plasmonic modes, with the strength of this coupling affecting the optical properties of the metamaterial. Small protein molecules consisting of the same scaffold, called Affimers, were immobilised onto the nanostructured surface with three different well-defined orientations. By utilising the experimental $\Delta\Delta S$ parameter, one orientation of the Affimer molecules could be distinguished, with the two others producing similar responses. However, when the reflectance spectra were modelled with a simple coupled oscillator model, the two retardation phase changes $\Delta\Delta\theta$ and $\Delta\Delta\phi$ could be extracted. With these two retardation phase parameters being shown to be a more incisive probe into the orientation of the Affimer molecules at the nanostructure surface.

In chapter 6, we continue using the $\Delta\Delta S$, and two retardation phase parameters introduced in chapter 5. However, here we utilised these phenomena to discriminate between two different immobilisation orientations of the cancer relevant protein, HSP90, as well as detecting any ligand induced conformational changes upon the addition of a well-known inhibitor molecule. By immobilising the same protein with two different orientations, we were able to show how the orientation of the immobilised molecule effects the sensitivity of the ligand induced changes detected. The experimental and modelled parameters used to characterise the differences, in the same way as chapter 5, showed very good agreement in the ligand induced changes detected. With one orientation of the immobilised protein exhibiting a higher sensitivity to the initial binding event of the inhibitor molecule. However, even though the experimental and modelled parameters were in agreement, the retardation phase phenomena was proved once again to be a more incisive probe into the ligand induced conformational changes of HSP90. With the modelled phase parameters detecting the final closure of the HSP90 molecule for one orientation, that was below the detection limit of the experimental $\Delta\Delta S$ parameter.

Finally, in chapter 7, we moved from detecting protein differences in ideal purified solutions, to the ultimate objective of using complex protein solutions, such as human blood serum. Human blood serum contains more than 20,000 different proteins, varying in concentrations from 50 g/L to less than 1 ng/L, with an overall concentration of ~ 1 mM, making it an extremely complex solution to characterise. The experimental $\Delta\Delta S$ parameter was used to quantify any changes in the protein corona when elevated levels of IgG were spiked into the serum solutions. By utilising an anionic ligand on the nanostructure surface, the amount of IgG adsorbed in the protein corona could

be enhanced relative to other proteins, due to IgG being the only abundant protein present in the serum solutions with an isoelectric point over 7. When the amount of IgG in the serum samples was increased, only the composition of the protein corona layer was altered, with the coverage on the nanostructure surface remaining the same between different concentrations of IgG spiked serum solutions. However, when the serum solutions were diluted in Tris buffer, at high IgG spiked concentrations, the concentration of IgG present in the protein corona also increased. With the IgG in the corona being tightly packed and randomly orientated relative to the nanostructure surface. Resulting in it becoming increasingly difficult to separate serum solutions consisting of different elevated IgG concentrations. To address this problem, the ionic strength of the solutions was increased by adding 150 mM NaCl to the dilution buffer. With the electrostatic shielding of the higher ionic strength buffer lowering the coverage of the protein corona on the nanostructure surface, due to the shielding of the electrostatic interactions between the anionic monolayer and the proteins in solution. The result of this lower coverage meant that lower effective concentrations of IgG were present in the corona relative to the bulk solution, allowing the IgG to orientate freely, and increasing the level of elevated IgG detected into the physiologically relevant levels necessary for clinical applications.

The preliminary results shown throughout this thesis demonstrate the sensitivity of these phenomena to the structure and orientation of protein molecules at the nanostructure surface. By using complex protein solutions, such as human serum solution, we have demonstrated, for the first time, the ability of using high-throughput injection moulded metamaterials for creating a commercially viable biosensing system. In progression from the initial observations detailed throughout this thesis, further investigation into the detection ability in complex protein systems, as well as characterising structural properties on the mesoscale (such as viruses), would be key objectives for any future work. With the ultimate goal of creating a high-throughput biosensing system, suitable for diagnostic characterisation in a clinical environment.

Appendix A – Plasmonic EIT Modelling

A.1 Modelling Function

The basis of the model used to fit the plasmonic induced transparency spectra within this thesis was first proposed by Zhang et al. [1] and subsequently used by Tassin et al. [2]. This coupled oscillator model describes the system by the equations:

$$\omega_r^{-2}\ddot{p}(t) + \gamma_r\omega_r^{-1}\dot{p}(t) + p(t) = gf(t) - \tilde{k}q(t) \quad (\text{A.1.1})$$

$$\omega_d^{-2}\ddot{q}(t) + \gamma_d\omega_d^{-1}\dot{q}(t) + q(t) = -\tilde{k}p(t) \quad (\text{A.1.2})$$

In these equations, the radiative (bright) resonator is described by the excitation $p(t)$, with a resonance frequency ω_r , and damping factor γ_r . Equally, the dark mode excitation is described by the excitation $q(t)$, with a resonance frequency ω_d , and a damping factor γ_d . The two resonators are coupled by a complex coupling constant \tilde{k} , with the bright mode being driven by an external force $f(t)$, and a constant, g , indicating the coupling strength between the oscillator and the external force. Equations A.1.1 and A.1.2 are solved by assuming the following solutions to these equations:

$$p(t) = e^{-i\theta}P(\omega)e^{-i(\omega t)} \quad (\text{A.1.3})$$

$$q(t) = e^{-i\phi}Q(\omega)e^{-i(\omega t)} \quad (\text{A.1.4})$$

As the coupling depends on the phase difference between the two oscillators, it can be considered that $\tilde{k} = ke^{-i(\theta-\phi)}$. Solving equations A.1.1 and A.1.2 for the solutions shown in A.1.3 and A.1.4 gives the following relations:

$$P(\omega)e^{-i\theta} = \frac{gF(\omega) - \tilde{k}Q(\omega)e^{-i\phi}}{D_r} \quad (\text{A.1.5})$$

$$Q(\omega)e^{-i\phi} = \frac{-\tilde{k}P(\omega)e^{-i\theta}}{D_d} \quad (\text{A.1.6})$$

Where $D_d = 1 - (\omega/\omega_d)^2 - i\gamma_d\omega/\omega_d$, and $D_r = 1 - (\omega/\omega_r)^2 - i\gamma_r\omega/\omega_r$.

By substituting equation A.1.6 into equation A.1.5, it becomes:

$$P(\omega) = \frac{gD_d(\omega)F(\omega)}{e^{-i\theta}(D_r(\omega)D_d(\omega) - k^2e^{-2i(\theta-\phi)})} \quad (\text{A.1.7})$$

The susceptibility is then calculated from equation A.1.7 using:

$$\chi(\omega) = \frac{P(\omega)}{E(\omega)} \quad (\text{A.1.8})$$

Where $E(\omega) = F(\omega)$, and hence susceptibility becomes:

$$\chi(\omega) = \frac{gD_d(\omega)}{e^{-i\theta}(D_r(\omega)D_d(\omega) - k^2e^{-2i(\theta-\phi)})} \quad (\text{A.1.9})$$

Since the plasmonic system being modelled here is based on a continuous metallic film, rather than individual nanostructures on a transparent substrate, this needs to be catered for through an effective medium approach. The average of the susceptibility from the plasmonic system and the gold film can then be calculated.

$$\chi_{Avg}(\omega) = \frac{\chi(\omega) + \chi_{Au}}{2} \quad (\text{A.1.10})$$

In equation A.1.10, χ_{Au} is the susceptibility of gold. As the refractive index can be calculated by taking the square root of the permittivity, and the susceptibility is directly related to the permittivity, the refractive index can be calculated as:

$$n_{EIT} = \sqrt{\chi_{Avg}(\omega) + 1} \quad (\text{A.1.11})$$

From this refractive index, and the refractive index of the solution (n_{Sol}), the reflectivity can be calculated by:

$$Reflectivity = \left| \frac{(n_{Sol} - n_{EIT})^2}{(n_{Sol} + n_{EIT})^2} \right| \quad (\text{A.1.12})$$

1. Zhang, S., et al., *Plasmon-Induced Transparency in Metamaterials*. Physical Review Letters, 2008. **101**(4): p. 047401.
2. Tassin, P., et al., *Electromagnetically Induced Transparency and Absorption in Metamaterials: The Radiating Two-Oscillator Model and Its Experimental Confirmation*. Physical Review Letters, 2012. **109**(18): p. 187401.

Appendix B – Experimental

B.1 Shuriken Symmetry and Hybridisation

Character table for structures consisting of C_6 symmetry is shown in Table B.01

C ₆ Character Table	E	C ₆	C ₃	C ₂	(C ₃) ²	(C ₆) ⁵	Linear functions, Rotations	Quadratic functions	Cubic Functions
A	+1	+1	+1	+1	+1	+1	z, R _z	x ² +y ² , z ²	z ³ , z(x ² +y ²)
B	+1	-1	+1	-1	+1	-1	-	-	y(3x ² -y ²), x(x ² -3y ²)
E₁	+1 +1	+ε +ε*	-ε* -ε	-1 -1	-ε -ε*	+ε* +ε	x+iy; R _x +iR _y x+iy; R _x -iR _y	(xz, yz)	(xz ² , yz ²) [x(x ² +y ²), y(x ² +y ²)]
E₂	+1 +1	-ε* -ε	-ε -ε*	+1 +1	-ε* -ε	-ε -ε*	-	(x ² -y ² , xy)	[xyz, z(x ² -y ²)]

Table B.01 C₆ symmetry character table.

B.2 Plasmonic EIT Modelling Method

To obtain the modelled spectra for each reflectance measurement, ten variables (described in chapter 3) were initially allowed to vary for the water/buffer spectra. These were varied by small amounts to achieve the best quality fit for the reference spectra, and stopped when changing the values were detrimental to the fit. These parameters were then carried forward in the model for the protein absorbed spectra, with only the five parameters, ω_r , ω_d , k , θ , and ϕ , being varied. These five parameters were again varied by small amounts to achieve the best fit, until no improvement could be made by altering the parameter values. This was repeated three separate times on the experimental data for each experiment, with the average values and standard errors being calculated for each of the five parameters in the modelled spectra.

Appendix C – Detection of Higher Order Structural Changes

C.1 Protein and Ligand Concentrations

Both EPSP synthase and shikimate kinase were purified as described in chapter 3. With the protein concentrations obtained being 20.0 mg/ml for EPSP synthase, and 7.7 mg/ml for shikimate kinase. HEPES buffered saline (10 mM 4-(2-hydroxyethyl)-1-piperazineethanesulfonic acid, and 150 mM NaCl) solution, pH 7.2, was used to make all ligand solutions. The EPSP synthase ligand solution was made up of 15 μ M shikimate-3-phosphate (S3P) and 5 μ M glyphosate. With the shikimate kinase ligand solutions consisting of 0.6 mM ADP, 2.0 mM shikimic acid, and 2.0 mM $MgCl_2$.

The ORD measurements were recorded in the presence of buffer after surface functionalisation, as a reference measurement, and then the protein solution was added to the surface and left to incubate at room temperature for 1 hour. Once the protein had adsorbed to the NTA/EG-thiol SAM, the protein solution was rinsed from the sample several times with buffer, and then further ORD measurements were recorded. Next, the appropriate ligand solution was added to the adsorbed proteins on the substrate surface, and left to incubate for 30 minutes before the final ORD measurements were recorded. All ORD measurements were recorded in the presence of 10 mM HEPES buffered saline (HBS) solution.

C.2 Ligand Only Solution ORD and Average Shifts

ORD spectra for respective ligand only solutions, in the absence of any adsorbed proteins, are shown in Figure C.01. The shifts shown for the ligand only solution, in the absence of protein, for the ORD spectra and in Figure C.01(b) are very small relative to the changes occurring for the proteins. The much larger shifts caused by the adsorption of the protein, and addition of the ligand solution to the adsorbed protein, compared with the ligand only solution is due to the protein being much larger than the ligands, and so will increase the refractive index of the region surrounding the nanostructures more than the ligand solution alone. When the respective ligand solutions are added to the immobilised proteins, in the case of EPSP Synthase, there is a decrease in the average shift as seen in Figure C.01(b). This is consistent with the conformational change expected, as the two domains close upon ligand binding, there is a reduction in the volume of the protein causing the decrease in average shift.

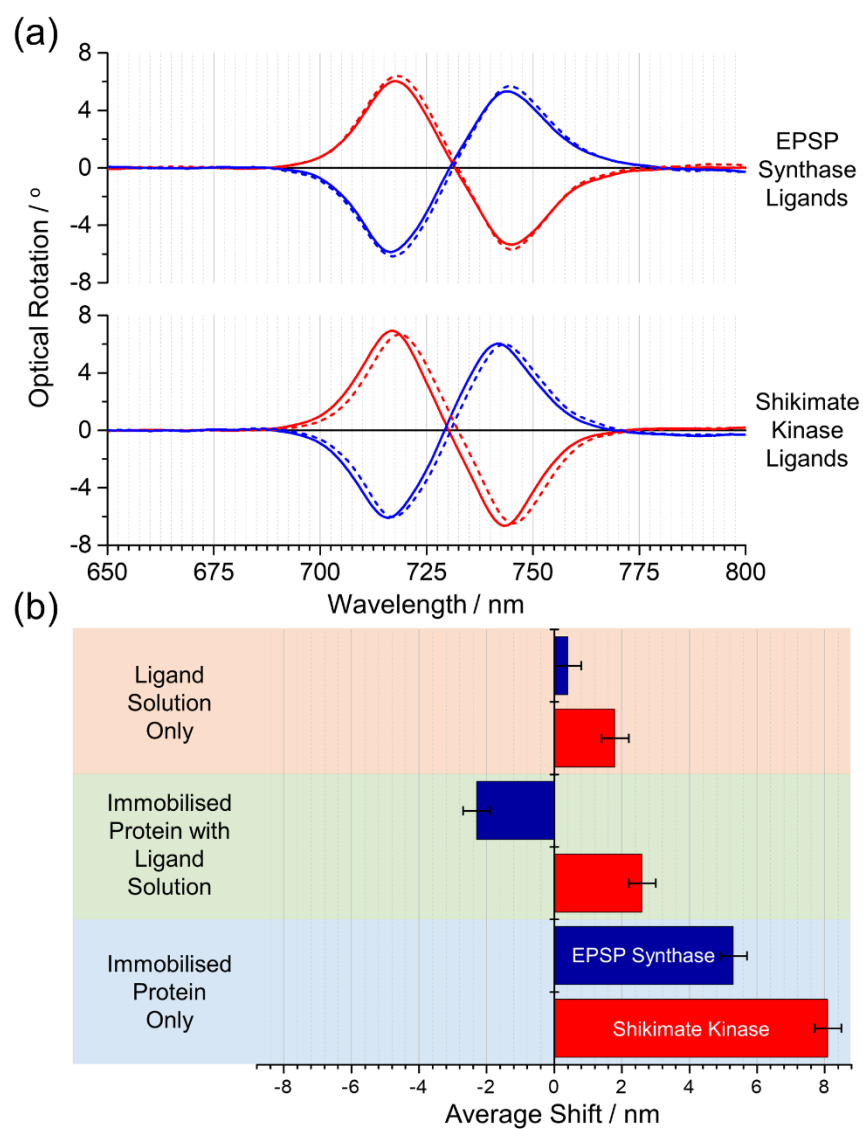


Figure C.01 (a) ORD spectra for EPSP Synthase (top), and shikimate kinase (bottom) ligand solutions relative to initial buffer measurements for left- (red) and right-handed (blue) shuriken structures. The solid and dashed lines represent the initial buffer measurement, and ligand solution measurements respectively. (b) The average shifts measured for EPSP Synthase and shikimate kinase when the protein was immobilised, when the ligand solutions were added to adsorbed proteins, and ligand solutions only in the absence of adsorbed protein. The error bars represent the standard error calculated from 8 spectra measurements.

Appendix D – Immobilisation and Results of Affimer Proteins

D.1 Immobilisation

All Affimer solutions were obtained from Avacta life sciences, and diluted to a concentration of 1 mg/ml in 10 mM HBS solution before being added to the substrate. The three Affimers received from Avacta, and their initial concentrations were: two glutathione S-transferase (GST) binding variants; G65C (1.5 mg/ml) and K67C (2.0 mg/ml), and one immunoglobulin G (IgG) binding variant; H6C (4.4 mg/ml). The concentrations of the target protein solutions, GST and IgG, added to the surface bound Affimers, were 0.8 mg/ml in each case.

To immobilise the Affimers onto the gold surface, the Affimer solution was added to the substrate and left to incubate at room temperature for 2 hours. This solution was then rinsed in 10 mM HBS. The surface was then 'back-filled' with a 10 μ M Triethylene glycol mono-11-mercaptopundecyl ether solution in 10 mM HBS, and left to incubate at room temperature for 1 hour. This was then again completely rinsed off with 10 mM HBS before the target protein was added. The respective protein solutions were then added to the immobilised Affimer surface, and left to incubate for 1 hour before being rinsed off with 10 mM HBS solution to remove any unbound protein. All experimental measurements were recorded after the substrate had been rinsed, and in the presence of 10 mM HBS.

D.2 ORD Results

ORD were recorded using the exact same methods as described in chapter 3, and used in chapter 4.

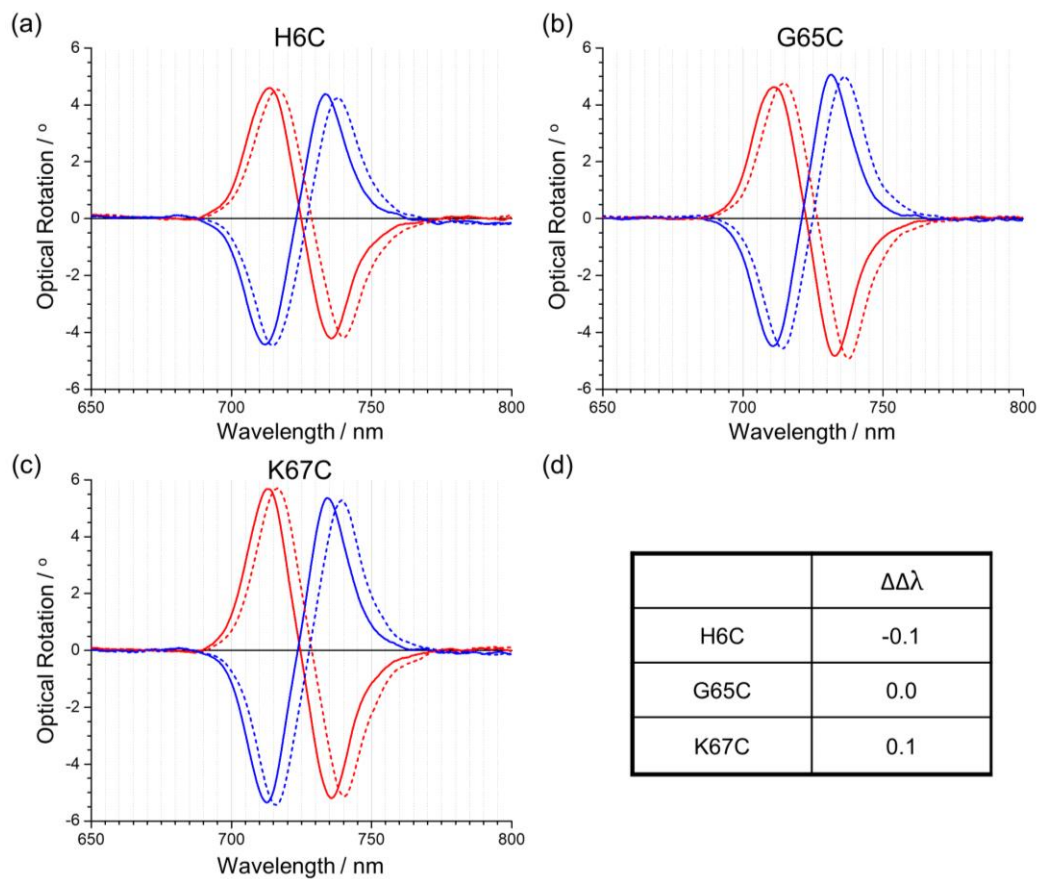


Figure D.01 ORD spectra for the three Affimer variants. (a) H6C, (b) G65C, and (c) K67C. Also (d) shows the $\Delta\Delta\lambda$ values for each Affimer for peak 1 of the ORD spectra.

D.3 Chiral Simulation Modelling Results

The chiral dielectric simulations were performed by Dr Affar Karimullah, using the Wave Optics module in COMSOL Multiphysics v4.4, a commercial finite element package.

The simulated data modelling parameters are shown in Table D.01. In the simulations, the left- and right-handed nanostructures have identical reflectivity spectra with water, and hence will have identical fitting parameters. The $\Delta\Delta\lambda$ values shown in Table D.01, show a significant asymmetry in θ and ϕ .

Parameter	Water	LH Chiral Dielectric	RH Chiral Dielectric	$\Delta\lambda$ LH	$\Delta\lambda$ RH	$\Delta\Delta\lambda$
ω_r	710.0	719.0	718.8	9.0	8.8	-0.2
ω_d	703.8	713.0	712.7	9.2	8.9	-0.3
k	0.02450	0.02400	0.02620	-0.00050	0.00170	0.00220
γ_r	0.0390	0.0390	0.0390	0	0	0
γ_d	0.01920	0.01930	0.01890	0.00010	-0.00030	-0.00040
θ	-13.7	-15.5	-12.7	-1.8	1.0	2.8
ϕ	-9.0	-10.0	-7.3	-1.0	1.7	2.7
g	0.02400	0.02400	0.02400	0	0	0
n_e	1.33	1.33	1.33	0	0	0
c_{Au}	0.1300	0.1300	0.1300	0	0	0

Table D.01 Fitting parameters for the reflectivity of the simulated spectra with water (identical for left- and right-handed nanostructures, and a chiral dielectric for both left- and right-handed structures).

Appendix E – Immobilisation HSP90 Protein

E.1 Protein and Ligand Concentrations

The HSP90 proteins were purchased from both Sigma Aldrich (C-terminus His-tag) and Enzo life sciences (N-terminus His-tag). Both variants of the protein were diluted to 0.1 mg/ml concentration, in 10 mM HEPES buffered saline (HBS), before being added to the nanostructured surface. To create the ligand solutions, 17-(Allylamino)-17-demethoxygeldanamycin (17-AAG) was dissolved in dimethyl sulfoxide (DMSO) to a total concentration of 20 μ M. This was then diluted in HBS buffer to give ligand solutions with total concentrations of 1 nM, 10 nM, 100 nM, 1 μ M, and 10 μ M. The control solutions of DMSO in buffer were prepared using the same volumes as above but without any 17-AAG inhibitor added.

The reflectance measurements were recorded in the presence of buffer after surface functionalisation, as a reference measurement. The protein solution was then added to the surface, and left to incubate at room temperature overnight (~17 hours). This was then rinsed with buffer several times, and further measurements recorded. After this, increasing concentrations of ligand solutions, from 1 nM to 10 μ M in 1 order of magnitude steps, were added consecutively to the immobilised protein and allowed to incubate for 30 minutes before reflectance measurements were recorded. All reflectance measurements were recorded in the presence of 10 mM HBS solution.

E.2 Modelling Values

Tables E.01 and E.02, show the numerical values for modelling of the HSP90 proteins with the ligand addition for the C-terminal His-tagged, and N-terminal His-tagged protein respectively.

C-Terminal His-tagged Protein					
	ω_r	ω_d	k	θ	ϕ
ΔLH HSP90	2.5	4.2	-0.0020	-1.0	1.1
ΔRH HSP90	0.4	5.2	0.0002	-2.0	6.0
$\Delta\Delta x$ HSP90	-2.1	1.0	0.0022	-1.0	4.9
ΔLH Ligand 1 nM	2.2	4.4	-0.0018	-1.2	1.7
ΔRH Ligand 1 nM	0.1	5.2	0.0000	-2.0	6.7
$\Delta\Delta x$ Ligand 1 nM	-2.1	0.8	0.0018	-0.8	5.0
ΔLH Ligand 10 nM	1.9	4.6	-0.0018	-1.4	2.5
ΔRH Ligand 10 nM	0.0	5.2	0.0002	-2.0	6.7
$\Delta\Delta x$ Ligand 10 nM	-1.9	0.6	0.0020	-0.6	4.2
ΔLH Ligand 100 nM	1.9	4.6	-0.0017	-1.4	2.5
ΔRH Ligand 100 nM	0.0	5.2	-0.0001	-1.9	6.7
$\Delta\Delta x$ Ligand 100 nM	-1.9	0.6	-0.0016	-0.5	4.2
ΔLH Ligand 1 μ M	1.9	4.6	-0.0016	-1.4	2.4
ΔRH Ligand 1 μ M	0.0	5.4	0.0000	-2.0	7.0
$\Delta\Delta x$ Ligand 1 μ M	-1.9	0.8	-0.0016	-0.6	4.6
ΔLH Ligand 10 μ M	1.5	4.6	-0.0016	-1.4	3.4
ΔRH Ligand 10 μ M	-0.4	5.2	0.0000	-2.0	6.9
$\Delta\Delta x$ Ligand 10 μ M	-1.9	0.6	0.0016	-0.6	3.5

Table E.01 Modelling values for the five variable parameters for the immobilisation of HSP90, and after the addition of each ligand solution for the C-terminal His-tagged protein.

N-Terminal His-tagged Protein					
	ω_r	ω_d	k	θ	ϕ
ΔLH HSP90	2.9	1.8	-0.0012	0.0	-0.1
ΔRH HSP90	0.8	3.0	-0.0008	-0.6	2.2
$\Delta\Delta x$ HSP90	-2.1	1.2	0.0004	-0.6	2.3
ΔLH Ligand 1 nM	3.1	1.8	-0.0018	-0.4	-1.4
ΔRH Ligand 1 nM	0.7	3.2	-0.0010	-0.8	2.6
$\Delta\Delta x$ Ligand 1 nM	-2.4	1.4	0.0008	-0.4	4.0
ΔLH Ligand 10 nM	3.3	1.8	-0.0018	-0.2	-1.3
ΔRH Ligand 10 nM	0.5	3.2	-0.0012	-1.0	3.1
$\Delta\Delta x$ Ligand 10 nM	-2.8	1.4	0.0006	-0.8	4.4
ΔLH Ligand 100 nM	3.3	1.8	-0.0016	0.1	-1.3
ΔRH Ligand 100 nM	0.5	3.4	-0.0012	-1.2	3.2
$\Delta\Delta x$ Ligand 100 nM	-2.8	1.6	0.0004	-1.3	4.5
ΔLH Ligand 1 μ M	3.2	1.8	-0.0018	-0.2	-1.1
ΔRH Ligand 1 μ M	0.4	3.5	-0.0011	-1.7	3.4
$\Delta\Delta x$ Ligand 1 μ M	-2.8	1.7	0.0007	-1.5	4.5
ΔLH Ligand 10 μ M	2.6	1.7	-0.0014	-0.2	0.2
ΔRH Ligand 10 μ M	0.0	3.5	-0.0010	-1.7	3.6
$\Delta\Delta x$ Ligand 10 μ M	-2.6	1.8	0.0004	-1.5	3.8

Table E.02 Modelling values for the five variable parameters for the immobilisation of HSP90, and after the addition of each ligand solution for the N-terminal His-tagged protein.

Appendix F – Human Serum Solutions

F.1 Serum solution preparation

Lyophilised human blood serum proteins (ERM[®] certified reference material) was purchased from Sigma Aldrich and diluted in distilled water to create a stock serum solution with a total protein concentration of 60 mg/ml. Serum solution, both spiked and unspiked, were produced with concentrations ranging from 3×10^{-4} to 3 mg/ml were produced by diluting the stock serum solutions with either 10 mM Tris buffer, or 10 mM Tris-saline buffer containing 150 mM sodium chloride (NaCl), both at pH 7.4. The spiked serum samples were produced by adding the relevant protein to the stock serum solution diluted to 3 mg/ml. The spiked IgG solutions were produced by adding 0.025, 0.050, 0.100, 0.175, and 0.250 mg of the protein per ml of serum solution diluted to 3 mg/ml. With lyophilised IgG from human serum being purchased from Sigma Aldrich. Subsequently, a further amount of relevant buffer was added to each spiked solution to give different spiked concentrations that each have a total protein concentration of 3 mg/ml. This provided solutions with 16.1%, 17.0%, 18.6%, 21.1%, and 23.6% IgG by mass. Transferrin, albumin, and IgG spiked serum solutions were produced by adding 0.050 mg, or 0.250 mg in the case of saline buffer diluted samples, of respective protein per ml of stock serum solution, once again diluted to give an overall concentration of 3 mg/ml for each spiked protein solution. All spiked solutions were then diluted with the relevant buffer to produce the required protein concentration solution between 3×10^{-4} and 3 mg/ml. It should be noted that, since serum solution contains saline at ~150 mM, the solutions diluted in Tris buffer containing no NaCl will still have a small saline concentration ranging from ~0.75 μ M to 7.5 mM. In contrast to the solutions diluted in Tris buffer containing 150 mM NaCl, which will have a saline concentration of ~150 mM to 157.5 mM. Therefore, the saline buffered solutions have a considerably higher ionic strength than the serum solutions alone.

The reflectance measurements were recorded in the presence of buffer after surface functionalisation, as a reference measurement. The serum solutions were then added to the surface, and left to incubate at room temperature for 20 minutes before the results were recorded. This was repeated for each consecutive measurement of increasing total protein concentration for each spiked solution. Therefore, the saline buffered solutions have a considerably higher ionic strength than the serum solutions alone.